Pulsed Laser Surface Treatment of Metals for Enhanced Field Emission Studies

By

ANIL KUMAR SINGH

(PHYS01201304014)

Bhabha Atomic Research Centre, Mumbai- 400085

A thesis submitted to the

Board of Studies in Physical Sciences

In partial fulfillment of requirements

for the degree of

DOCTOR OF PHILOSOPHY

of

HOMI BHABHA NATIONAL INSTITUTE

August, 2020

Homi Bhabha National Institute

Recommendations of the Viva Voce Committee

As members of the Viva Voce Committee, we certify that we have read the dissertation prepared by **Anil Kumar Singh** entitled **"Pulsed Laser Surface Treatment of Metals for Enhanced Field Emission Studies"** and recommend that it may be accepted as fulfilling the thesis requirement for the award of Degree of Doctor of Philosophy.

Chairman – Prof. Saibal Basu		Date: 24/08/2020
Guide / Convener – Prof. Sucharita Sinha		Date: 24/08/2020
Co-guide - ------		Date: - - -
Examiner - Prof. Jyotsna Dutta Majumdar		Date: 24/08/2020
Member 1- Prof. Madangopal Krishanan		Date: 24/08/2020
Member 2- Prof. A. K. Ray		Date: 24/8/2020
Member 3- Dr. C. P. Paul		Date: 24/08/2020.
Technical advisor: Dr. Amitava Roy		Date: 24/08/2020

Final approval and acceptance of this thesis is contingent upon the candidate's submission of the final copies of the thesis to HBNI.

I hereby certify that I have read this thesis prepared under my direction and recommend that it may be accepted as fulfilling the thesis requirement.

Date: 24/08/2020

Place: BARC, Mumbai

Sucharita Sinha

Signature:

Guide: Dr. (Smt.) Sucharita Sinha

STATEMENT BY AUTHOR

This dissertation has been submitted in partial fulfillment of requirements for an advanced degree at Homi Bhabha National Institute (HBNI) and is deposited in the Library to be made available to borrowers under rules of the HBNI.

Brief quotations from this dissertation are allowable without special permission, provided that accurate acknowledgement of source is made. Requests for permission for extended quotation from or reproduction of this manuscript in whole or in part may be granted by the Competent Authority of HBNI when in his or her judgment the proposed use of the material is in the interests of scholarship. In all other instances, however, permission must be obtained from the author.

Anil Kumar Singh

DECLARATION

I, hereby declare that the investigation presented in the thesis has been carried out by me. The work is original and has not been submitted earlier as a whole or in part for a degree/diploma at this or any other Institution/University.

Anil Kumar Singh

List of publications arising from the thesis

A. Journal Publications:

1. Self-assembled micro-cones generated on solid surface through pulsed laser irradiation, S. Sinha, **A. K. Singh**, Adv. Mat. Lett., (2013) 4, 6, 492-496.
2. Enhanced field emission from nanosecond laser based surface micro-structured stainless steel, **A. K. Singh**, D. Shinde, M.A. More, S. Sinha, Appl. Surf. Sci., (2015), 357, 1313-1318.
3. Field emission study from an array of hierarchical micro-protrusions on stainless steel surface generated by femtosecond pulsed laser irradiation, **A. K. Singh**, S. R. Suryawanshi, M. A. More, S. Basu, S. Sinha, Appl. Surf. Sci., (2017), 396, 1310-1316.
4. Field emission study from tantalum surfaces micro-structured with femtosecond pulsed laser irradiation, **A. K. Singh**, S. R. Suryawanshi, M. A. More, S. Sinha, Appl. Phys. A, (2018), 124:573, 1-9.
5. Nanosecond laser induced surface micro-structuring of Tantalum targets for improved field emission, **A. K. Singh,** S. R. Surayawanshi, M. A. More, K. Singh, S. Sinha, Mater. Res. Express, 6 (2019) 106418, 1-14.
6. Numerical simulation of the period of surface micro-protrusions generated on Titanium and Stainless Steel targets by femtosecond laser irradiation, **A. K. Singh**, S. Sinha, J. Appl. Phys., 128, 124903 (1-14), (2020).

B. Conference Publications:

1. Generation of micro-cones on stainless steel surface by femtosecond pulsed laser irradiation and its field emission study, **A. K. Singh**, S. R. Suryawanshi, M. A. More, S. Sinha, National Laser Symposium-23, CP-05-07, Dec. 3-6, (2014).

2. Surface micro-structuring of stainless steel 304 by femtosecond laser for novel applications, **A. K. Singh**, S. Suryawanshi, P. Jha, M.A. More and S. Sinha, Theme Meeting on Ultrafast Science (UFS-2016), P-42, Nov. 24-26, (2016).

C. Other Publications:

1. Nanosecond pulsed laser induced generation of open macro porosity on sintered ZnO pellet surface, **A. K. Singh**, S. Samanta, S. Sinha,Appl. Surf. Sci., (2015), 325, 139-144.
2. Surface micro-structuring of type 304 stainless steel by femtosecond pulsed laser: effect on surface wettability and corrosion resistance, **A. K. Singh**, B. S. Kumar, P. Jha, A. Mahanti, K. Singh, V. Kain, S. Sinha, Appl. Phys. A, (2018), 124:846, pp. 1-9.
3. 3D Hetro-architecture of GdB_6 nano particles on lessened Cu_2O nanowires: enhanced field emission behavior, S. R. Suryawanshi, **A. K. Singh**, M. Deo, D. J. Late, S. Sinha and M. A. More, Cryst. Eng. Comm., (2015), 17, 3936-3944.
4. A facile approach towards fabrication of GdB_6-ZnO heteroarchutecture as high current density cold cathode, S. R, Suryawanshi, C. D. Mistari, **A. K. Singh**, D. M. Phase, D. J. Late, S. Sinha, M. A. More, Chemistry Select, (2016), 1, 1-8.
5. Pulsed laser deposition of graphite in air and in vacuum for field emission studies, H. S. Jadhav, **A. K. Singh**, S. Sinha, Materials Chemistry & Physics, (2015), 162, 279-285.
6. Pulsed laser deposition of nanostructured Co-B-O thin films as efficient catalyst for hydrogen production, H. Jadhav, **A. K. Singh**, N. Patel, R.

Fernandes, S. Gupta, D. C. Kothari, A. Miotello, S. Sinha, Appl. Surf. Sci., (2016), 387, 358-365.

7. Surface treatment of 45S5 bio-glass using femtosecond laser to achieve superior growth of hydroxyapatite, S. Shaikh, S. Kedia, **A. K. Singh**, K. Sharma, S. Sinha, J. Laser Applications, (2017), 29 (2), 022004 (1-8).

8. Morphology and structural studies of laser treated 45S5 bioactive glass, K. Sharma, S. Kedia, **A. K. Singh**, C. B. Basak, A. K. Chauhan, S. Basu, S. Sinha, Journal of Non-Crystalline Solids, (2016), 440, 43-48.

DEDICATIONS

"Dedicated to my family"

ACKNOWLEDGEMENT

Completion of this doctoral thesis was possible with the help of several people. I would like to express my sincerely gratitude to all of them**.** There are chances that I may fail to mention name of some of the individuals who have supported me. I sincerely apologize for such mistakes while writing this acknowledgement.

Firstly, I would like to express my sincere gratitude to my research guide Dr. Sucharita Sinha, (Outstanding Scientist, LPSPS, BARC and Prof. of Physics in HBNI) for the invaluable guidance and consistent encouragement throughout the research work. I consider it a great opportunity to do research under her supervision. She always made herself available to clarify my doubts despite her busy schedule.

I am thankful to my co-guide during the initial phase of my Ph.D. programme Dr. K. Dasgupta, former Associate Director, Beam Technology Development Group, BARC and Dr. A. K. Das, former Head, Laser and Plasma Technology Division, for their support and giving me opportunity to register for Ph.D. programme.

I would also like to express my sincere gratitude towards my doctoral committee members, Dr. Saibal Basu (former Head, Solid State Physics Division, BARC & Prof. in HBNI), Dr. A. K. Ray (former Project Leader, RISP, BARC and Prof. in HBNI), Dr. Madangopal Krishanan (Associate Director, Materials Group, BARC and Prof. in HBNI), Dr. C. P. Paul, (Scientific Officer G, RRCAT, Indore), Dr. Amitava Roy (Scientific Officer G, APPD, BARC) for their insightful comments, encouragement, making them available for regular progress review of the research work. Their questions during the progress review incented me to widen my research from various perspectives.

I am grateful to Shri. S. Kundu, Tunable Laser Section, Laser & Plasma Technology Division, BARC, for his support and encouragement during the research work.

I am thankful to my fellow labmates, Dr. S. Kedia, Harshada Jadhav, Shazia Shaikh, for their support and valuable discussions during the entire research work. I am also thankful to my colleagues Mr. Amit Khattar, Mr. Abdul Wahid, Mr. Ajit. Singh, Mr. Jitendra S. B. Singh, Mr. S. K. Maurya, Mrs. P. S. Mohite, Mr. J. S. Dhumal, Mr. Tarang Garg, Mr. Biswajit Jana, Mr. R. Satpute for their generous supports during this research activity.

I would also like to express my sincere thanks to Prof. M. A. More, Department of Physics, Savitribai Phule Pune University, Pune for allowing me to carry out field emission characterization in his lab. I am also thankful to his students Dr. Ranjit V. Kashid, Dr. Deodatta Shinde, Dr. S. R. Suryawanshi and Mr. Somnath who worked with me during nights and holidays too for field emission characterization of the laser treated samples.

During this work I received generous helps from many of the researchers in BARC whose support culminated into this thesis. I would like to thank all of them. Among these names I remember: Mr. Lalchand of PED, Mrs. Sabana Khan of MMD, Mr. Arvind Bind of MMD, Dr. Soumen Samanta of TPPED, Dr. Jagnnath of TPPED, Dr. A. K. Debnath of TPPED and Dr. P. U. Sastry of SSPD.

Last but not the least, I would like to thank my family: my parents, wife, brother, sisters daughter and son for supporting me spiritually throughout writing this thesis and my life in general. I am extremely grateful to my wife who went through a lot of challenges during the period of this research activity but allowed me to work from early in the morning till late in the night and also during holidays. I could have not imagined completing this thesis without her sacrifices.

CONTENTS

LIST OF FIGURES

LIST OF TABLES

Chapter 6

Conclusion & Future perspective

6.1 Conclusion

In the present study, we carried out surface micro-structuring of stainless steel 304 (SS 304) and tantalum (Ta) samples via irradiation with a focused beam of nanosecond (ns) or femtosecond (fs) lasers. Surface micro-structuring of sample surfaces was carried out by varying laser fluence and number of laser pulses irradiating the target at a specific location. Surface micro-structured samples were characterized in terms of surface morphology, roughness, chemical phase, crystallographic phase and field emission behavior. Irradiation of targets with optimized laser fluence and number of laser pulses resulted in generation of self-assembled micro-protrusions on the surfaces. These micro-structured surfaces have shown improved field emission behavior in comparison to the pristine samples. In addition to the experimental work theoretical simulation was carried out to predict period of the generated micro-protrusions on SS 304 surface corresponding to irradiation with fs laser pulse.

Surface micro-structuring experiments on SS 304 targets using nanosecond laser revealed that targets irradiated with laser fluence $\geq$ 4 J/cm^2 and 3000 pulses resulted in deep crater formation in the target. Self-assembled micro-protrusions were formed in the laser irradiated surface when incident laser fluence was $\leq$ 2 J/cm^2. Average height of the generated micro-protrusions on SS surface corresponding to 2 J/cm^2 increased from 17 μm to 30 μm when number of incident laser pulses increased from 3000 to 9000. While initial growth of height of surface protrusions with incident number of pulses was rapid it slowed after certain number of laser pulses. When SS sample was irradiated with 0.7 J/cm^2 and 6000 laser pulses surface micro-

protrusions were formed over the entire laser irradiated spot. SS 304 sample treated with laser fluence of 0.7 J/cm^2 was characterized for chemical phase. This sample showed that laser treated surface consists of iron oxides and iron nitrides. SS 304 sample surface micro-structured with laser fluence of 0.7 J/cm^2 demonstrated low turn on field (~7.5 V/μm), high macroscopic field enhancement factor (~585) and delivered emission current density up to 340 μA/cm^2. Formal area efficiency of emission for this specimen was estimated to be ~2.7×10^{-10} which implies that a very small fraction of the actual specimen was actually contributing towards emission of electrons. Field emission current from the laser micro-structured specimen was fairly stable over the test period.

Similarly, surface micro-protrusions were generated on Ta targets via nanosecond laser irradiation with laser fluence of 0.9 J/cm^2 and varying number of laser pulses in the range 3000 to 9000. In the case of Ta too, height of the generated surface micro-protrusions and mean roughness of the laser treated surface increased with increasing number of irradiating pulses. Raman spectroscopy results revealed that chemical phase of the laser treated region varied with position within the laser irradiated region. Central region of the laser irradiated spots where incident local laser fuence was higher remained in metallic phase while periphery of the irradiated spot consists of Ta_2O_5. Laser treated Ta samples showed enhanced field emission. Ta sample treated with 9000 laser pulses demonstrated lowest E_{on} (~3.7 V/μm) and delivered maximum emission current density (~386 μA/cm^2) among all the laser treated Ta samples. However, field emission current stability of this sample was poor in comparison to the other laser treated Ta samples.

Dense array of self-assembled micro-protrusions were generated on SS sample surfaces using optimized fs laser fluence and number of incident pulses per location. SS sample showed

generation of surface micro-protrusions with number density ~5.6 x 10^5 micro-protrusions/cm^2corresponding to irradiation with laser fluence of 0.5 J/cm^2 and number of laser pulses per location equal to ~3.1 x 10^4. When SS sample was irradiated with laser fluence of 0.9 J/cm^2 and number of laser pulses equal to ~2250 (corresponding to target scan speed of 400 μm/s) surface micro-protrusions were generated with number density ~1.5 x 10^6 micro-protrusions/cm^2. SS sample micro-structured with ~3.1 x 10^4 laser pulses per location at laser fluence of 0.5 J/cm^2 showed superior field emission behavior in comparison to SS sample surface modified with 2250 laser pulses per location at laser fluence of 0.9 J/cm^2. Measured turn on field and estimated macroscopic field enhancement factor corresponding to SS specimen treated with laser fluence of 0.5 J/cm^2 were ~4.1 V/μm and ~1830, respectively. The observed poor field emission behavior of the SS sample treated with 0.9 J/cm^2 was explained on the basis of field screening effect.

Similarly, dense array of self-assembled micro-protrusions were generated on Ta surfaces via irradiation with fs laser pulses with optimized laser fluence levels for achieving enhanced field emission. Number densities of the generated surface micro-protrusions on Ta samples treated with laser fluence levels of 0.35 J/cm^2, 0.45 J/cm^2 and 0.55 J/cm^2 were ~8.8 x 10^5, ~7.5 x 10^5 and ~3.5 x 10^5 μ-protrusions/cm^2, respectively. Fs laser modified Ta surfaces were found to predominantly consist of Ta_2O_5. The fs laser modified Ta samples demonstrated improvement in field emission behavior. Ta sample treated with laser fluence of 0.55 J/cm^2 has shown lowest turn on field (4.0 ± 0.6 V/μm) and highest macroscopic field enhancement factor (4400 ± 500) among all the fs laser treated Ta samples. However, its field emission current stability was poorer than other laser modified samples.

In addition to experimental investigations on ns and fs laser induced surface modification and their characterization we carried out a theoretical simulation study to predict period of the generated surface micro-protrusions on SS 304 and titanium surfaces by fs laser. Simulated period of the generated surface micro-protrusions on Ti surface as a function of laser fluence was compared with reported experimental data on Ti to validate our theoretical model. Simulated trend of the variation of micro-protrusions period with laser fluence broadly matched with the reported data confirming validity of the model. Thereafter, this model was used to simulate period of the generated micro-protrusions on SS 304 sample corresponding to fs laser irradiation.

6.2 Future perspective of the work

Future scope of the work described in this thesis includes both experimental and theoretical investigations. In future, other materials such as Tungsten (W), Molybdenum (Mo) and Niobium (Nb) could be surface micro-structured using both fs, as well as, ns lasers. In order to achieve high field emission current density at low applied field along with stable emission current, laser parameters would have to be optimized. Also materials having low work function, high thermal and electrical conductivity, low vapor pressure, high melting point and high hardness could be deposited on surface micro-structured surfaces to achieve enhanced field emission current density, stable emission current and long cathode life time. In future, simulation would be further improved by incorporating change in material properties as a function of temperature to predict number density and height of the cones and range of fluence over which cones are formed. Simulation would also be extended to account for multiple laser pulses instead of single pulse condition.

Summary

In the present thesis, surface micro-structuring of metallic targets such as Stainless Steel 304 (SS 304) and Tantalum (Ta) have been carried out via direct irradiation with nanosecond (ns) and femtosecond (fs) laser pulses with the aim to generate high density micro (μ)-protrusions for achieving field emission enhancement. Surface micro-structuring of sample surfaces was carried out by varying laser fluence and number of laser pulses irradiating the target at a specific location. The surface μ-structured specimens have been investigated in terms of surface morphology, chemical phase, crystallinity and their field emission behavior.

Target surfaces irradiated with optimum laser fluence and number of laser pulses has shown generation of dense μ-protrusions on their surfaces. Typical areal number density of the generated surface μ-protrusions on SS 304 and Ta targets were of the order of ~10^5 to 10^6 μ-protrusions/cm^2 corresponding to fs laser based treatment. These μ-protrusions causes enhancement of local field on their tips resulting in enhanced field emission compared to the pristine surfaces. Laser modified SS 304 and Ta targets have shown high macroscopic field enhancement factor in the range of 585−1830 and 270−4500, respectively.

Theoretical simulation to predict spatial period of the generated surface μ-protrusions/areal number density for SS 304 and Ti targets as a function of laser fluence has been carried out. Our numerical model has been validated by comparing simulation results with the reported experimental results for Ti. Simulated variation of the period of the generated surfaces micro-protrusions with incident laser fluence was found to be in good agreement with the reported experimental data.

Chapter 1

Introduction and Objectives of the Study

1.1 Introduction

Surface modification involves tailoring specific surface properties of materials without altering their bulk properties. Surface modifications have resulted in significant improvement in performance of these materials in a variety of applications. For example, surface micro-structuring of solar cells has shown enhanced conversion efficiency due to increase in absorptivity of the surface [1], generation of surface micro/nano structures on sensing materials resulted in increase in surface area and hence improved sensitivity [2-3], surface textured implants have demonstrated faster growth of body tissues and improved osseointegration [4, 5], surface modification has enhanced resistance of samples against corrosion and wear [6, 7], surface micro-structured catalysts have shown superior catalytic activity [8, 9] and surface micro/nano structured field emission cathodes have shown high emission current densities at low applied voltages [10-13].

Field emitting cathode (FEC) is a device which ejects electrons from its surface on account of applied high electric fields. FECs are widely used in vacuum micro/nano electronic devices and related technologies due to its offered advantages over thermionic emission cathodes. These include− low power consumption (no energy is wasted in form of heat as in the case of thermionic cathodes), high brightness (~100 to 1000 times higher brightness than thermionic cathodes), low energy spread, high speed switching capability (switching demonstrated up to few GHz), compactness and longer cathode life [14-16]. FECs can be either in the form of single tip field emitter or large area field emitter (LAFE) consisting of an

ensemble of several emitters on a surface. Single tip field emitters offer advantage of high brightness in comparison to LAFEs but limitation comes from current handling capabilities. On the other hand LAFEs can withstand higher emission current in comparison to single tip field emitters without damage. There are many applications such as electron beam accelerators, free electron lasers, flat panel displays, generation and amplification of microwaves etc., where use of LAFEs improves performance of the devices. Therefore, development of FECs delivering high emission current density with good stability at low operating electric fields has attracted considerable interest of researchers. Performance of a LAFE is governed by properties of the cathode material, surface morphology and ambient environment of operation. Hence, performance of a LAFE can be improved via either tailoring material properties or surface morphology. Field emission cathodes with micro/nano surface features have been reported to show improved field emission behavior.

Numerous techniques have been employed to generate micro/nano protrusions on cathode surfaces such as Spindt technique [17], ion beam etching [18], electrochemical etching [19], thermal oxidation [20], hydrothermal method [21] and pulsed laser irradiation [12]. Each of these techniques has its own advantages and limitations. Pulsed laser irradiation based surface micro-structuring technique offers numerous advantages such as simplicity, single step and non-contact processing, clean processing as no use of chemicals is involved, high processing speed, high degree of reproducibility, good spatial resolution, easy automation, flexibility in terms of control over laser parameters and choice of processing environment [12].

1.2 Objectives of the study

The main objective of this thesis was to generate dense micro-protrusions on metallic target surfaces (Stainless steel 304 and Tantalum) using nanosecond (ns) and femtosecond (fs) pulsed

laser irradiation in order to achieve enhanced field emission. Other associated objectives of this study were –

i. Investigation on the effects of laser fluence, number of incident pulses and pulse duration on surface morphology, chemical phase, and field emission behavior of laser micro-structured specimens.
ii. Theoretical simulation to predict areal number density/period of the generated surface micro-protrusions on laser treated surfaces.

1.3 Fundamentals of pulsed laser based surface micro/nano-structuring

Lasers have ability to deposit energy in the target at precise location within a localized volume. The energy transferred from laser to the target leads to heating of the target and change in surface properties depending upon the amount of energy deposited and the volume over which energy has been deposited. Laser based surface modification of materials occurs mainly in four steps namely– (i) Absorption of laser beam in target (ii) Generation of heat, heating of the target and phase change (iii) Flow of melt pool (iii) Energy dissipation and re-solidification. To understand different processes/mechanisms in laser surface modification understanding of laser–matter interaction is important. Since in the present study we have carried out surface micro-structuring of metals hence mechanism for interaction of laser beam with metals has be explained below.

The first and the most important step in laser based surface processing of materials is absorption of incident laser beam by the target. It is this absorbed energy in the target which leads to modifications in the material. When a laser beam is incident on metal surface a fraction of the total incident laser power is coupled to the target depending upon reflectivity of the target (R). Reflectivity of the target depends on target material properties, angle of incidence,

polarization, and the wavelength of the laser beam [22]. The fraction of laser energy (1-R) which enters the target surface first gets absorbed by free electrons by inverse bremsstrahlung process causing these electrons to reach their excited state. These heated electrons collide with other electrons present in the target and transfer their energy coming into thermal equilibrium among themselves. Excited electrons then transfer energy to lattice via electron phonon scattering process. The exchange of energy between electrons and phonons leads to thermalization of electronic and lattice subsystems over a time scale of few picoseconds. After occurrence of thermalization a single temperature of the target is defined and all the processes occurring thenafter are thermal in nature process.

The energy absorbed from the laser beam thus leads to increase in target temperature. If the absorbed energy is sufficiently high it causes melting of the target up to certain depth or even vaporization. The target also dissipates energy contained in the absorption volume to the bulk of the target through thermal diffusion and to the ambience via radiation loss mechanism. While in molten phase, liquid in the melt pool may move and get be transported from one place to another place. Based on heat dissipation mechanisms temperature of the target material starts reducing and re-solidification of the target takes place at the end of the incident optical pulse resulting in formation of new material surface properties. Schematic diagram depicting time scales of different processes occurring in laser-matter interaction is shown in Fig. 1.1.

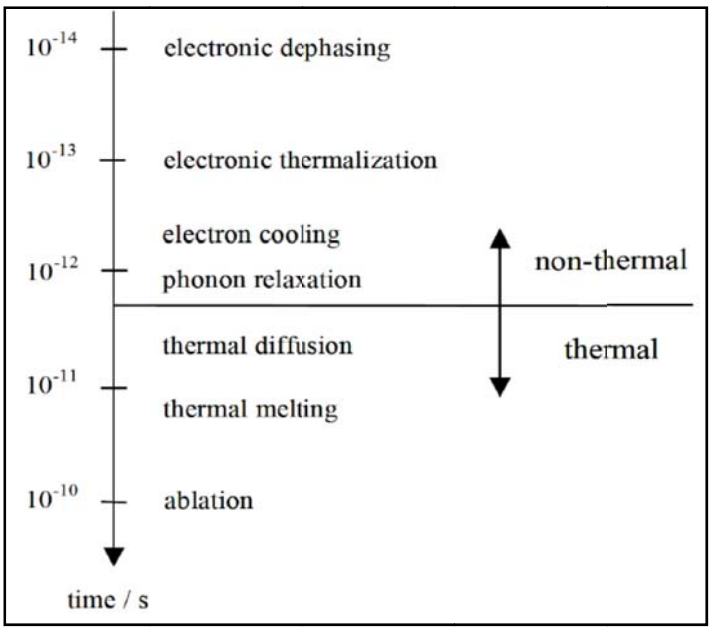

Figure 1.1 Schematic diagram depicting time scales of different processes in laser matter interaction [23].

1.4 Work reported on pulsed laser surface micro/nano structuring – A review

Surface micro/nano-structuring of materials is widely used in variety of applications owing to its offered advantages. Some of the reported works on surface micro-structuring using nanosecond and femtosecond lasers have been listed below.

Generation of super-hydrophobic surfaces by ns and fs laser induced surface texturing has been reported in [24-29]. Refs. [24-26] and [27-29] have reported nanosecond and femtosecond laser induce surface modifications, respectively. In ref. [24], D. V. Ta et al., have reported that texturing of Cu & brass using ns pulsed laser with wavelength of 1064 nm resulted in formation of superhydrophobic surfaces. In [25], authors have generated superhydrophobic surface of 316L steel via generating an array of micro-holes using ns pulsed laser irradiation and optimizing their pitch and depth. Ref [26] has reported surface texturing of Ti-6Al-4V alloy using nanosecond pulsed laser irradiation and heat treatment leading to generation of super

hydrophobic surface. This surface has shown significant reduction in bacterial growth on the surface. Ref. [27] has reported wettability control of SS 316L by fs laser induced surface modification. In ref. [28], authors have micro-structured copper surface using fs laser irradiation with continuously scanning the target. Here, authors have reported that by optimizing processing parameters and modifying surface chemistry super hydrophobic surface (contact angle up to 165^{o}) can be generated. In ref. [29], authors have reported generation of superhydrophobic silicon surface by femtosecond laser irradiation.

Nanosecond and femtosecond laser induced surface modification technique is also employed for modifying surface morphology of the bio-implants. Surface textured implants have been reported to demonstrate improvement in their performances [4, 5, 30]. In ref. [4], authors have carried surface micro-structuring of Ti implants via Nd:YAG laser irradiation and compared bonding strength of these implants with mechanically machined Ti implants in rats. Here, authors observed that bonding of laser micro-structured Ti implant was superior to machined Ti implant. Ref. [5] has reported that laser (355 nm wavelength) based surface micro-structuring of Ti dental implants showed reduced bio-film formation in comparison to Ti surfaces prepared via grit ballast, enamel and machined techniques. In ref. [30], S. Mukherji et al. have reported that micro-texturing of Ti6Al4V bio-implant with fiber laser has resulted in enhanced biocompatibility.

Another application in which laser based surface micro-texturing has shown great potential is tribology. There are many reports available in literature demonstrating that laser micro-structuring of materials results in reduced friction induced wear [31-35].

Nanosecond and femtosecond laser induced surface micro/nanostructuring of the solar cells has been reported to show enhanced efficiency [1, 36, 37]. Ref. [1] has reported that

irradiation of solar cell surface by ArF excimer laser leads to formation of array of micro-protrusions resulting enhancement of absorptivity and hence efficiency of solar cell. In Ref. [36], authors have generated nanostructures on Si surface which resulted in increase in responsivity and conversion efficiency of the photovoltaic cell. In Ref. [37], B. K. Nayak et al., have reported that fs laser induced micro-structuring of thin a-Si:H films results in significant enhancement in efficiency of solar cell.

Apart from the aforementioned applications of the laser surface modification technique field emission from large area cathodes have been reported to improve via generation of self-assembled mciro/nano protrusions on emitter surface [10-13].

1.5 Basics of field electron emission

Liberation of electrons from solid surface to vacuum is called electron emission. Electron emission from a surface can occur via any of the four basic mechanisms, namely (i) thermionic emission (ii) photo-electric emission (iii) secondary emission and (iv) field emission. Thermionic emission is the process of electron emission from the cathode surface due to heating which provides sufficient thermal energy to electrons to overcome the potential barrier at the surface. In photo-electric emission electrons are ejected from the cathode surface via irradiation with photons of sufficient energy. Secondary electrons are emitted from the surface by via bombardment of the surface with energetic particles. In field electron emission process emission of electrons takes places due to application of intense electric field. Since in field emission process cathode surface remains at close to room temperature field electron emission is also known as cold field emission or in short field emission.

Field emission from cold metal surfaces was first observed by R. W. Wood in 1897 [38]. W. Schottky made first attempt to explain this phenomenon based on classical theory in 1923

[39]. However, experimentally observed value of turn on field was 10 to 50 times lower than the values predicted by W. Schottky model. In year 1928, R. H. Fowler and L.W. Nordheim gave a theory of field emission based on quantum mechanical tunneling of electrons through surface potential barrier [40]. This theory is commonly known as F-N theory. F-N theory describes relation between field emission current from bulk metal surface and applied electric field. F-N theory was experimentally validated by E. Muller by measuring emission current from clean tungsten (W) tips [41].

1.6 Fowler-Nordheim (FN) theory for field emission

F-N theory explains field emission from a bulk metal surface on the basis of quantum mechanical tunneling of electrons. Tunneling probability of electrons through a potential barrier depends on potential barrier height and thickness. Field emission of electrons takes place at high electric fields on the surface (in the range 10^7–10^8 V/cm). Applied electric field leads to potential barrier narrowing and height reduction both resulting in increasing transmission probability of electrons [42]. Field emission from metals can be understood as following-

In metals free electrons are present in high number density which can move freely within the metal. Therefore, these free electrons are considered as free electron gas. However, in absence of external source these free electrons in metal cannot escape from the metal surface because there exists a potential barrier of infinite width and height equal to work function at metal to vacuum interface. When external electric field is applied on the surface, shape of the potential barrier is deformed into a triangular shape of finite thickness. Thickness of the potential barrier depends on magnitude of the field on the surface (local field). The triangular shape of barrier is further modified to rounded shape near to surface due to image force. Image force is generated due to interaction between emitted electrons and conducting surface. Therefore, shape

of the potential barrier is determined by work function of the emitting surface, electric field on the surface and image charge potential. Potential barrier on the cathode material surface is given by following expression [42] –

$$V(x) = \varphi - eEx - \frac{e^2}{16\pi\varepsilon_0 x} \qquad \text{..... (1.1)}$$

Here, φ, E, ε_0 and x are work function of the material, external electric field on the surface, electric permittivity of vacuum and distance from the surface, respectively. Potential barrier of the form written in equation 1.1 is known as Schottky-Nordheim (SN) barrier [43]. The resulted lowering of the potential barrier height (Δφ) due to image force is given by–

$$\Delta\varphi = \sqrt{\frac{e^3 E}{4\pi\varepsilon_0}} \text{ ..... (1.2)}$$

Deformation of the potential barrier shape and reduction in height due to applied electric field has been schematically shown in Fig. 1.2.

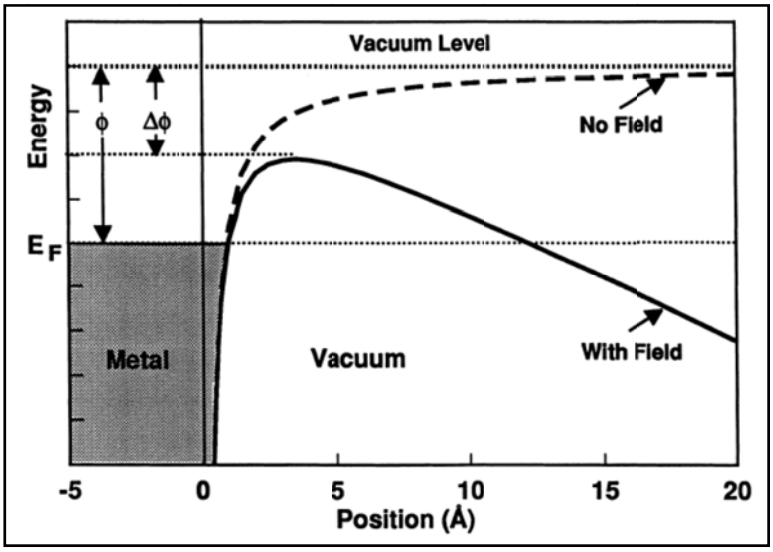

Figure 1.2 Potential energy diagrams for electron near metal surface [44].

The aforementioned reduction in height and width of the potential barrier leads to significant increase in transmission probability of electrons through tunneling process provided electric field on the surface is high. F-N considered some assumptions and solved Schrodinger equation to find a relationship between the emission current density and the applied electric field as–

$$J_L = a\varphi^{-1}E_L^2 \exp\left(-\frac{b\varphi^{\frac{3}{2}}}{E_L}\right) \quad \ldots\ldots\ldots\ldots (1.3)$$

Here, J_L is local emission current density, E_L is local electric field on the surface and φ is work function of the material. a (=1.5414 34 μA eV V^{-2}) and b (= 6.830890 eV^{-2} V nm^{-1}) are universal constants called first and second FN constants. Assumptions considered by F-N were [45] –

i. Emitter is a metal with smooth and flat surface and there is a constant field outside.
ii. Ignored atomic structure of emitter.
iii. Potential barrier is exact triangular i.e. ignored exchange and correlation effect.
iv. Assumed Sommerfeld type free electron model.
v. Emitter temperature is 0 K.
vi. Several mathematical approximations.

However, exact triangular potential barrier is physically unrealistic. Later on Nordheim tried to calculate transmission probability of electrons for Schottky–Nordheim (SN) type barrier. Unfortunately, his calculations significantly under predicted the transmission probability [45].

In year 1950, Murphy and Good (MG) made corrections to the existing field emission theory, resulting in following revised FN type equations –

$$J_L = t_F^{-2} a\varphi^{-1} E_L^2 \exp\left(-\nu_F \frac{b\varphi^{\frac{3}{2}}}{E_L}\right) \quad \ldots\ldots\ldots\ldots (1.4)$$

Where, t_F and ν_F are mathematical functions sometimes called as field emission elliptic functions [31]. In FN type equation proposed by MG all other assumptions were same as FN assumptions except the barrier form. Further, MG used JWKB (Jeffreys Wentzel Kramers Brillouin) approximation that does not generate tunneling pre-factor which should be present. Technically complete equation for relating field emission current from large area field emitter with the applied macroscopic electric field is given by [45] –

$$J_m = \lambda_m a \varphi^{-1} \beta_m^2 E_m^2 \exp\left(-\frac{\nu_F b \varphi^{\frac{3}{2}}}{\beta_m E_m}\right) \ldots\ldots\ldots\ldots\ldots (1.5)$$

Here, J_m and E_m are macroscopic field emission current density and macroscopic applied electric field, respectively. λ_m is macroscopic pre exponential factor, β_m is macroscopic field enhancement factor and ν_F is barrier form correction factor.

1.7 Parameters affecting field emission from an emitter

Field emission from an emitter depends upon its properties such as morphology, work function, electrical and thermal conductivity, hardness, vapor pressure, adsorption on the surface, residual gas pressure. Influences of some of these parameters have been summarized below.

1.7.1 Effect of emitter surface morphology

Surface morphology of a field emitter plays a vital role on its field emission behavior. If there are surface micro/nano features on the cathode surface they lead to increase in local (microscopic) electric field on the surface by concentrating electric field lines on their tips. This phenomenon is called local field enhancement. Local field enhancement leads to significantly high electric field on the cathode surface even at low applied field resulting in enhanced field emission. Schematic diagram depicting equipotential lines between tip emitter array and plate anode is shown in Fig.

1.3 [46]. This figure indicates that electric field (defined as gradient of potential) maximizes near the emitter tip. This figure is just for illustration purpose. However, in the present study separation between cathode and anode is much larger than the value shown in Fig. 1.3. Enhancement factor of the local electric field on the tip depends upon aspect ratio, radius of curvature and number density of the micro/nano protrusions. Higher aspect ratio and smaller radius of curvature of micro/nano protrusions results in higher field enhancement factor. When separation between surface micro/nano features is reduced below certain value electric field on one micro tip starts perturbing the equipotential line on the other protrusions resulting in reduced field enhancement factor (Screening effect) [47].

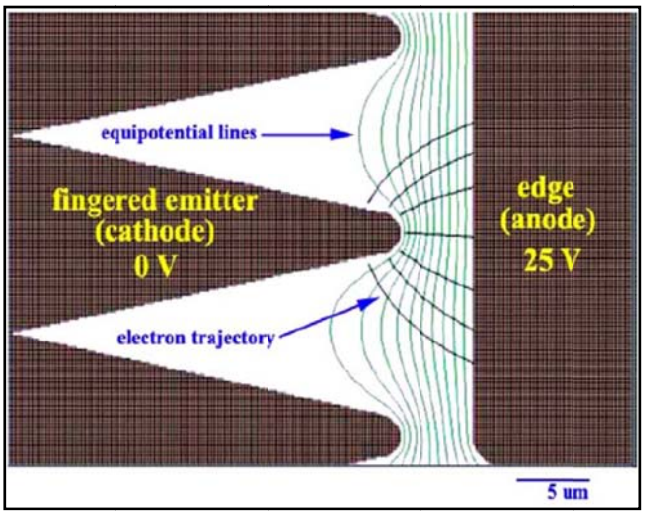

Figure 1.3 Typical image showing equipotential plot around the tip emitter array and electron trajectory [46].

1.7.2 Effect of work function of emitter

Work function of the field emitting surface determines strength of the potential barrier at emitter surface to vacuum. Hence, work function of the material surface determines emission current

from a cathode surface. Cathode having lower work function delivers higher emission current at a given external electric field (Equation 1.5).

1.7.3 Electrical and thermal conductivity of emitter

Electrical and thermal conductivities of the emitter surface plays important role in determining current handling capacity of the emitter. High electric conductivity ensures supply of electrons at surface for emission and low energy dissipation due to Joule heating. At large emission current level Joule heating of the emitter surface can lead to damage of surface micro-protrusions which are taking part in emission. Similarly, high thermal conductivity of the surface helps in removal of generated heat via Joule heating effect and minimizes chances of damage of emitting tips due to joule heating effect. Hence, high electrical conductivity and thermal conductivity is desired for large emission current handling. However, apart from joule heating Nottingham effect can also plays role in heating/cooling of the micro-protrusions during field emission [48].

1.7.4 Hardness of emitter surface

During the process of field emission residual gas atoms in the vacuum chamber get ionized and are accelerated by electric field and collide with emitter surface. This collision of ions with emitter surface causes physical sputtering of the surface resulting in reduced service life of the emitter. High hardness of the emitter material reduces sputtering yield and increases life time of the emitter.

1.7.5 Emitter material vapor pressure

Low vapor pressure of the emitter can generate sufficient number of atoms near tip surface causing breakdown and arcing effect at the surface. This phenomenon limits the applied electric field up to which such an emitter can be used.

1.7.6 Residual gas pressure

Emission current from a field emitter strongly depends on the ambient pressure. Electric field required for discharge to occur in a gas medium depends upon pressure and nature of the gas. Since the electric field required for field emission of electrons is ~10^8 V/m whereas breakdown of the gas occurs at electric field ~10^7 V/m [49]. Hence, vacuum is required for field emission.

Another important pressure dependent effect is ionization of residual gas atoms between anode and cathode. These generated ions get accelerated due to applied electric field and collide with the surface of the cathode resulting in damage of the surface protrusions. Degradation of surface protrusions results in deterioration of the field emission.

Additionally, high ambient pressure leads to adsorption and desorption of the gas molecules on the emitter surface resulting in fluctuation in field emission current. Effect of residual gas can be reduced by working in ultra high vacuum.

1.8 Desired material properties of a good field emitter

Performance of a field emitter cathode strongly depends on properties of the emitter material. Desired material properties of a good field emitter are –

i. Low work function.
ii. High electrical conductivity.
iii. High thermal conductivity.
iv. High hardness.
v. Very good chemical inertness.
vi. Low vapor pressure.
vii. High melting point.

1.9 Reported work on field emission enhancement via surface modification– Review

There exist several reports on generation of variety of surface morphologies on the cathode surface using different methods and their field emission characterization. These include nano-rods, urchin nanostructures, nano-fibers, nanobelts, nanoflakes, micro/nano-spikes array, nano-pyramids on different materials. Field emission cathodes with aforementioned surface morphologies have demonstrated improved field emission behavior. Results of some of these investigations have been summarized below.

1.9.1 Field emission from urchin like nanostructures

There are several reports presenting generation of urchin like nanostructures on different material surfaces and their field emission characterization. Cathode surfaces with urchin type nanostructures have resulted in improved field emission behavior [50-52]. Ref. [50] has reported generation of urchin type nanostructure of Co_3O_4 by depositing Co_3O_4 films by pulsed laser deposition (PLD) technique and subsequently annealing these films at 600^oC for 8hrs in air. Co_3O_4 films with urchin type nanostructures have shown superior field emission in comparison to Co_3O_4 films without urchin structures. Measured turn on electric fields (defined for emission current density of 10 $\mu A/cm^2$) for films with and without urchin nanostructures were ~3 V/μm and 5 V/μm, respectively. The term "turn on field" used in this thesis is basically a macroscopic electric field unless otherwise clearly stated. Also, maximum delivered emission current density for film with surface urchins was 480 $\mu A/cm^2$ at 6 V/μm while emission current density for Co_3O_4 film without urchin was < 100 $\mu A/cm^2$ at 6 V/μm.

In ref. [51], Li-Chieh Hsu et al.have generated 3-dimensional urchin like Fe_2O_3 structures on Fe spheres via thermal oxidation process. Here substrate with Fe spheres was heated for 10 hrs at 300^oC temperature resulted in formation of urchin like structure with tip diameter of the

spine in the range 10-20 nm. This surface has demonstrated good field emission with turn on field ~ 2.8 V/μm and maximum delivered current density upto ~ 50 μA/cm^2 at ~3.5 V/μm.

In another report [52], authors have generated of ZnO urchin nanostructures using hydrothermal route which have demonstrated good field emission performance with turn on field (defined for 10μA/cm^2) equal to ~3.7 V/μm and delivered emission current density up to ~4 mA/cm^2.

1.9.2 Field emission from nanowires/nano rods

Researchers have also grown high density nanowires on various cathode surfaces showing improved field emission behavior [53-59]. In ref. [53], authors have reported synthesis of α-Fe_2O_3 nanowires via thermal oxidation of iron films and investigation on their field emission behavior. In this work, authors have observed that for a given heating temperature (350^{o}C) and time (10 h) number density of the grown nanowires increased with increasing thickness of the iron films used for thermal oxidation. Also, there is an optimum number density of the nanowires for maximum field emission. Specimen with medium number density of nanowires on the surface (~7.8 x 10^8 nanowire/cm^2)has shown lowest turn on field (~3.3 V/μm).

X. Sun et. al. [54] have reported that high density iron nanoneedles are formed on iron plate via thermal oxidation process. Surfaces with grown surface nanoneedles have demonstrated improved field emission behavior with turn on field of ~ 4.8 V/μm due to local enhancement of electric field on surface.

In other report, fabrication of LaB6 nanowires via catalyst free chemical vapor deposition technique and their field emission behavior investigation has been reported [55]. In best case LaB_6 nanowires array have shown turn on field as low as 1.8 V/μm and delivered emission current density upto ~5.6 mA/cm^2 at applied electric field of ~2.9 Vμm^{-1} at room temperature.

Field emission behavior from CuO nanowires grown on Cu via thermal oxidation process has been reported in ref. [56]. Here, surfaces with CuO nanowires have demonstrated turn on fields in the range 3.5 - 4.5 $V\mu m^{-1}$ and delivered maximum current of ~ 0.45 mA at applied field of ~7 V/μm. In another work CuO nanowires generated via thermal oxidation has shown turn on field equal to ~ 0.7 $V\mu m^{-1}$ and maximum delivered current density ~ 5-6 mA [57].

Growth of vertically aligned Co nanowires grown via electro-deposition technique and their field emission behavior is reported in ref. [58].

In a work reported in [59], authors have synthesis of ZnO nanowire array on silicon substrate via chemical vapor deposition which has shown good field emission behavior. In this work authors have also observed that morphology and field emission behavior both can be tailored by varying growth time.

1.9.3 Field emission from nanofibers

Many researchers have demonstrated that one dimensional nanofibers and nanobelts and two dimensional sheet like structures show promising field emission behavior [60-61]. For example, Ref. [60] reports generation of α-MoO_3 nanofibers on Mo via hydrothermal process and its field emission characteristics. The surface with grown MoO_3 nanofibers has shown low turn on field (~2.5 V/μm) and high field enhancement factor (~ 4347).

Field emission behavior of dense, sparse and patterned carbon nanofibers have been reported in [61]. In this work, carbon nanofibers have been produced via plasma enhanced chemical vapor deposition technique. Density of the nanofibers in dense, sparse and array forms were 10^9 nanofibers/cm^2, 10^7 nanofibers/cm^2 and 10^6 nanofibers/cm^2, respectively. All these specimens showed enhanced field emission. However, performance of array of nano fibers was superior among all the samples. The observed higher enhancement in array of nanofibers has

been explained on the basis of absence of field screening effect due to lower number density of emitters.

1.9.4 Field emission from nanobelts

Cathodes having nanobelts on their surfaces have demonstrated significant enhancement in field emission. Ref [62] reports formation of GaN nanobelts on Si surface and its field emission behavior. Generated GaN nanobelts on Si surface have delivered emission current density upto ~350μA/cm^2 at applied electric field of ~13.5 V/μm. Also, emission current from this specimen was found to be fairly stable over the test period of ~6 hrs.

Field emission investigation of the TiS_3 nanobelt films generated via surface assisted chemical vapor transport is reported in [63]. TiS_3 nanobelt films produced in this study have shown excellent field emission with turn on field of ~ 1 V/μm and delivered current density up to 4 mA/cm^2.

1.9.5 Field emission from hybrid nanostructures

Apart from generation of nanostructures of metal oxides and metal sulfides for field enhancement applications field emission from hybrid nanostructures have also been reported [64 -67]. For example Ref. [64] has reported that Si tip array coated with monolayer of graphene shows better field emission behavior. Similarly, references [65] & [66] have reported that ZnO and Cu_2O coated with GdB_6 films demonstrated improved field emission behavior. Ref. [67] has reported that coating of Si tips array with LaB_6 results in significant improvement in field emission behavior.

1.9.6 Field emission from laser micro-structured surfaces

There are many reports on field emission investigation from self-assembled micro-protrusions/spikes on cathode surfaces which have been generated by irradiation with nanosecond and femtosecond pulsed lasers. These laser micro-structured surfaces have shown promising field emission behavior. Some of the investigations on field emission behavior of laser modified emitters are summarized below.

Y. Liu et al. [68] have reported fabrication of self-organized conical microstructures of cyanoacrylate-carbon nanotube composites by irradiation with excimer laser and their field emission behavior characterization. Their investigation has shown that sharp conical features are formed corresponding to for laser fluence in the range 1.5 – 2.0 J/cm^2 and number of laser pulses in the range of several thousands. In this work target surface micro-structured with 8000 laser pulses at laser fluence of 1.5 J/cm^2 has shown low turn on field (2.0 V/μm) and high emission current density (300 μA/cm^2) in comparison to untreated sample which showed turn on field equal to ~3.5 V/μm and delivered emission current density only up to 5 μA/cm^2.

In another investigation [69], authors have reported generation of dense array of micro-conical features on Si surface via irradiation with nanosecond (ns) and femtosecond (fs) lasers under SF_6 environment. In this investigation surface micro-spike are generated on the surface by varying incident laser fluence in the range 1 J/cm^{2}to 3.5 J/cm^2. Observed separation between the grown spikes were in the range ~2.5 μm to 5μm and 20 μm to 25μm corresponding to Si surfaces treated with fs and ns lasers. These surface micro-structured specimens have shown low turn on field (~2 V/μm) and high emission current density up to 1 mA/cm^2 @ 4 V/μm.

Similarly, ref. [70] has reported micro-structuring of copper surfaces using nanosecond pulsed Nd:YAG lasers irradiation and their field emission characterization. Laser micro-

structured specimens have shown turn on field as low as ~5.5 V/μm and field enhancement factor up to ~2730.

Picosecond laser based generation of micro/nano structures on LaB_6 surfaces have been reported in ref. [71]. In this work, laser surface modified LaB_6 surfaces have demonstrated low turn on field (~2.3 V/μm [defined for current density ~10μA/cm^2) and delivered emission current density up to 530 μA/cm^2]).

In Ref. [72], authors have grown laser induced self-assembled micro-cones on Si and Ni surfaces and incorporated carbon nano-tubes (CNTs) in these protrusions for enhanced field emission. These micro-structured specimens have shown very good field emission with turn on field (defined for ~10 μA/cm^2 current density) in the range 1.0 to 3 V/μm and emission current density upto ~100 μA/cm^2.

Q. Z. Zhao [73] et al., have reported generation of carbon micro-cones on graphite surface by femtosecond laser irradiation and their field emission characteristics. Graphite surface with generated micro-cones has shown low turn on field (~2.5 V/μm). However, its maximum delivered current was only ~ 1μA/cm^2 for applied electric field of 5.5 V/μm.

E. Spanakis et al. have reported field emission performance of metal coated Si emitter surface [74]. In this study surface micro-cones have been generated via femtoscond laser irradiation and coated with Au and Cr metals.

In ref. [75], authors have generated surface micro-protrusions on silicon surface using nanosecond, picosecond and femtosecond laser irradiation. In this study it has been reported that that Si surface irradiated with nanosecond laser have resulted in cone formation with tallest height and lowest number density among all the samples. Nanosecond laser based micro-structured samples have shown best field emission characteristics.

Field emissions from laser micro-structured Tungsten (W) surfaces have been reported in ref. [76]. In the work reported in [76], W surfaces have been micro-structured by irradiating with ns pulsed Nd:YAG laser with varying laser fluence. These surface micro-structured surfaces have been reported to show significant local field enhancement (up to ~3490).

1.10 Motivation of the work

Metals possess high electrical and thermal conductivity along with work function in intermediate range (~4−5 eV). However, metallic surfaces suffer from limitations of high sputtering yield and high sensitivity for oxidation. Therefore, they can serve as a good field emitting cathodes under ultrahigh vacuum. It has been reported that dense micro/nano protrusions are generated on metal surfaces by direct irradiation with nanosecond and femtosecond laser irradiation leading to local field enhancement resulting in enhanced field emission at low applied electric fields. There are many reports on nanosecond and femtosecond pulsed laser induced generation of self-assembled micro-protrusions/spikes on the metal surfaces. However, only few of them have carried out field emission characterization of the laser micro-structured metal specimens.

For example, Yuji Kawakami et al. [77] generated microcones on Tungsten (W) surface using irradiation with nanosecond pulsed Nd:YAG laser in air, SF_6 and helium ambiences. In this authors have reported formation of dense surface micro-cones in air, He and SF_6 gas environments for laser fluence in the range 5.0 – 10 J/cm^2, 3.0 – 10.0 J/cm^2 and 3.0 – 12 J/cm^2, respectively. However, authors have not investigated field emission behavior of the laser modified W samples.

In another work generation of micro-cones array on Tantalum (Ta) and stainless steel (SS) surfaces using copper vapor laser irradiation in vacuum and air has been reported [78]. In

this work authors have investigated effect of surface micro-cones array on reflectivity of the surface.

Robert Lloyd et al. [79] have reported generation of self-assembled micro-structures on stainless steel surface using direct irradiation with Nd:YVO_4 and Nd:YAG lasers. Nd:YVO_4 and Nd: YAG lasers were delivering lasers at wavelength of 532 nm and 1064 nm, respectively. In this study also field emission behavior of the micro-structured specimens has not been investigated but effect of laser wavelength and number of laser pulses on period and height of generated surface micro-structures is presented.

Generation of self-assembled micro/nano structures on metal surfaces (Titanium, Aluminium and Copper) by femtosecond pulsed laser irradiation has been very systematically investigated by B. K. Nayak et al. [80]. Authors have reported generation of high density, nearly uniform surface micro-cones on metal surfaces. However, in this work field emission from the micro-structured surfaces has not been investigated.

Although, there are numerous reports on nanosecond and femtosecond based surface micro-structuring and their field emission behavior only few have reported field emission behavior of laser based micro-structured metals surfaces. Hence, in the present study surface micro-structuring of metallic surfaces (Ta, and Stainless steel 304) has been carried out using nanosecond and femtosecond laser irradiation to investigate effect of processing parameters such as pulse duration, laser fluence, number of laser pulses on surface morphology and optimize laser parameters to achieved enhanced field emission from laser modified surfaces.

Chapter 2

Description of Experimental Setup & Characterization Techniques

2.1 Introduction

This chapter deals with experimental part of the study. Here, experimental procedures employed for surface micro-structuring and characterization of micro-structured surfaces have been explained along with description of various hardware/components. This includes description of method of preparation of targets used for surface modification, different components & hardware of experimental setup used for surface micro-structuring, techniques used for characterization of surface micro-structured specimens such as Scanning Electron Microscopy (SEM), Energy Dispersive X-ray Spectroscopy (EDS), Surface Profilometer, Grazing Incidence X-Ray Diffraction (GI-XRD), X-ray Photoelectron Spectroscopy (XPS), Kelvin Probe Microscopy and Field Emission characterization setup. This chapter is divided in two parts – (i) Description of surface micro-structuring procedure (ii) Description of characterization techniques.

2.2. Description of surface micro-structuring procedure

In the present study, surface micro-structuring of commercially available type 304 stainless steel (SS 304) and high purity (99.9% pure) tantalum (Ta) targets has been carried out using a focused beam of nanosecond and femtosecond pulsed lasers. Targets chosen for surface micro-structuring were samples having typical surface dimensions ~ 1 cm x 1 cm. These targets were polished with emery papers of different grit sizes (grit size 180 and grit size 1/0) and cleaned with ethanol/acetone before using as targets. Cleaned sample was mounted on computer controlled XY translational stage and irradiated with a focused laser beam in air. Schematic diagram of the

experimental setup used for surface micro-structuring process is shown in Fig. 2.1. The main components of this setup are nanosecond (ns)/femtosecond (fs) laser system, plane mirror, focusing lens and a computer controlled XY translational stage. Description of each of the components is provided below.

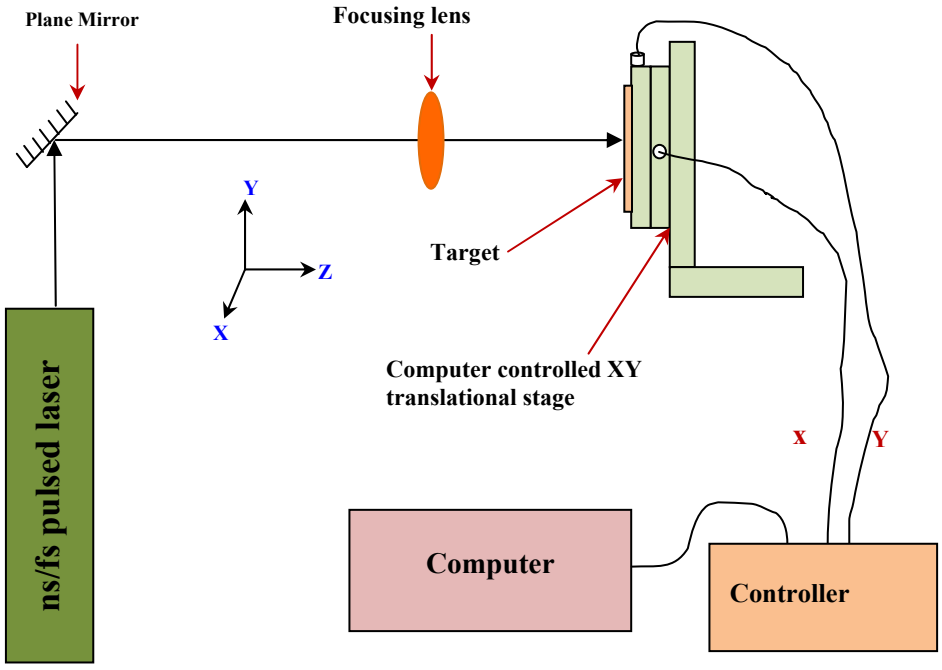

Figure 2.1 Schematic diagram of experimental setup used for surface micro-structuring.

2.2.1 Nanosecond laser system

This is a commercially available Q-switched nanosecond pulsed Nd:YAG laser system (Make: EKSPLA, Lithuania, Model number: NL311) which delivers laser pulses of duration 6 ns (FWHM). It is a flash lamp pumped laser system consisting of two stages - one oscillator and one amplifier stage. Q-switching in this laser system is done via electro-optic technique. This laser is basically a high pulse energy and low pulse repetition frequency system which delivers pulse energy up to ~1300 mJ at fundamental frequency (λ = 1064 nm) at 10 Hz pulse repetition frequency (prf.). This laser generates green beam at λ = 532 nm via second harmonic generation

technique using a KDP crystal. Maximum delivered output pulse energy at 532 nm wavelength is up to 600 mJ. Diameter of the delivered beam is ~10 mm with divergence < 0.5 mrad. Spatial profile of the output beam is nearly top-hat in near field and nearly Gaussian in far field. Pulse energy stability of the laser at 1064 nm and 532 nm wavelengths are ~0.5 % and 1.5%, respectively. Power drift in 8 hrs of continuous operation is ±2 %. Laser beam has very good pointing stability (±50 μrad). In the present surface micro-structuring experiments laser beam at 532 nm wavelength having vertical polarization has been used. Output power of the laser is controlled via a combination of a half waveplate and a polarizer. By rotating angle of the optic axis of the half waveplate output power of the laser can be controlled.

2.2.2 Femtosecond laser system

Femtosecond laser system employed in the present study is a commercially available laser system (Make: Thales, France; Model: Femtocube). This system delivers laser beam at a wavelength (λ) of 800 nm with 50 fs (FWHM) pulse duration and 3 kHz prf. Active medium in this laser is a Titanium Sapphire (Ti:Sa) crystal. This laser system works on the principle of chirped pulsed amplification (CPA) and consists of four main parts which are shown in schematic diagram (Fig. 2.2).

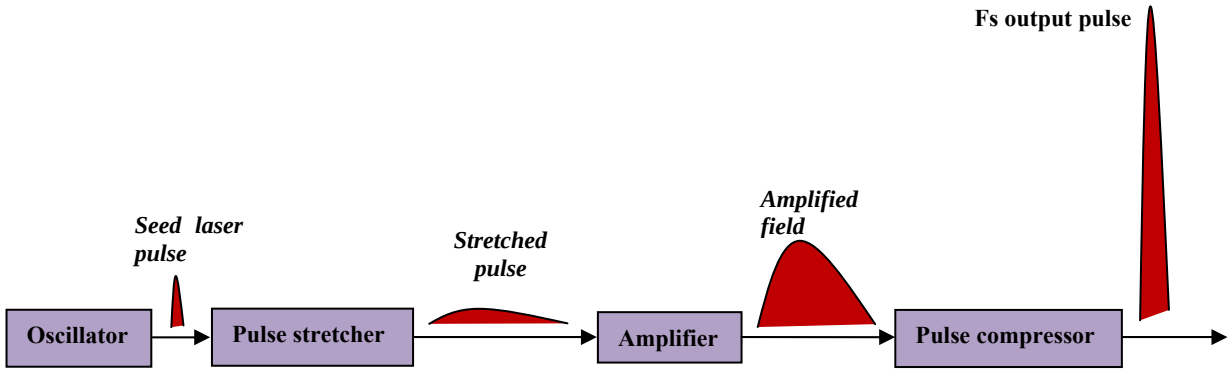

Figure 2.2 Schematic diagram of fs laser based upon chirped pulse amplification (CPA) technique.

This laser delivers maximum average power of 2.5 W which corresponds to pulse energy of 833 μJ. Size of the output fs laser beam is 12 mm in diameter and it has a divergence of ~0.5 mrad. Output beam of this laser is a vertically polarized beam.

2.2.3 Plane mirror

Plane mirror has been used to direct the beam on target surface. Mirror used in the present study is a hard dielectric coated high reflectivity mirror with reflectivity ~99 %.

2.2.4 Focusing lens

To focus the incident laser beam on the target surface a biconvex lens made of fused silica has been used. Based on laser fluence requirements in some of the experiments 20 cm focal length lens has been used while, in some cases 50 cm focal length lens has been used, to carry out surface micro-structuring.

2.2.5 Computer controlled XY translational stage

To carry out surface modification over large area samples targets have been mounted on a translational stage which can be moved in X and Y directions in a controlled manner.For movement of the stage along X and Y directions one stepper motor is connected for movement along each axis. Speed and range of the movement in both the directions can be controlled via software installed in computer. Each axis can be programmed independently. Step size of the movement is 0.125μm and speed of the stepper motor can be changed from 1 step/s to 10000 steps/s. Maximum range of movement along each axis is 25 mm. Also, provision exists such that stage can be held static at a particular location for user defined time and then shifted at user defined speed by a preselected distance.

2.3 Description of characterization techniques

Surface micro-structured specimens have been characterized in terms of surface morphology, roughness, elemental composition, chemical phase, crystal structure and work function using Scanning Electron Microscopy (SEM), Surface Profilometer, Energy Dispersive X-ray Spectroscopy (EDS), Raman Spectroscopy and X-ray Photoelectron Spectroscopy (XPS), Grazing Incidence X-ray Diffraction(GI-XRD), Kelvin Probe Microscopy techniques, respectively. The surface micro-structured specimens have also been characterized for their field emission behavior. Brief description of these characterization techniques have been provided below.

2.3.1 Scanning electron microscope (SEM)

A scanning electron microscope (SEM) is a specialized version of the electron microscope. It uses a focused beam of energetic electrons to interact with surface of solid specimens producing a variety of signals at the surface [81]. Interaction of high energy (accelerated) electrons with sample may produce– (a) secondary electrons (SEs) (b) back scattered electrons (BSE) (c) characteristic X-rays and light (d) continuous X-ray (e) transmitted electrons. SEs are emitted from very close to the sample surface and its intensity strongly depends upon surface morphology. SEM based upon detection of SE provides information about surface texture with spatial resolution of the order of ~1 nm. Back scattered electrons emerge from deeper location of the sample. Hence spatial resolution for backscattered electron detection is poor in comparison to SE detection. However, intensity of backscattered electrons depends upon Z number of the target. Hence, SEM based on detection of backscattered electrons can proved information about elemental distribution inside the target. Image of the sample surface is produced by scanning the

focused electron beam in a raster scan manner and correlating beam position with detected signal [82].

In a conventional SEM samples are observed under high vacuum while in case of environmental SEM low vacuum is used. Due to narrow width of the electron beam SEM micrographs have a large depth of field which results in characteristic 3-dimensional appearance of the sample under investigation which helps in understanding surface morphology. In SEM wide range of magnification is possible (from ~10X up to 500kX) [82]. Working principle of a SEM can be understood from the schematic diagram shown in Figure 2.3.

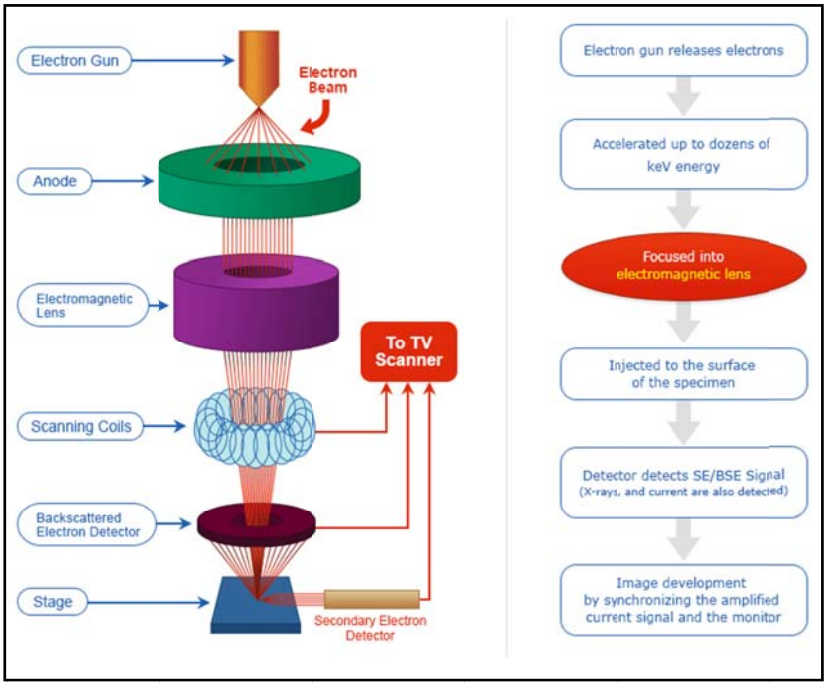

Figure 2.3 Schematic diagram of a SEM with flow chart of different processes [83].

Every SEM has an electron gun which is the source of electrons. These electrons are generated either via thermionic emission or field emission principle. These ejected electrons are accelerated to high kinetic energy (typical energy in the range 20 to 25 keV) by applying positive voltage on an anode. Accelerated beam of electron then passes through electromagnetic lens (condenser)

stage which focuses the beam to a small size on the target. The electrons illuminating the target surface ejects secondary electrons. These electrons are counted using an electron detector. To generate surface image electron beam is scanned in a raster manner and SE signal intensity is recorded. Scanning of the electron beam is achieved with the help of a pair of scanning coil which scans electron beam in x and y direction. Scanning is controlled via scan control circuit. Information about the position of electron beam is extracted from the scan control circuit and SE signal intensity as a function of position is plotted which generates surface texture of the specimen. Specimen to be characterized in SEM has to be conducting in order to provide path for incident electrons. If they are not conducting a thin coating of conducting material is done before characterizing with SEM.

2.3.2 Energy dispersive X-ray spectroscopy (EDS)

EDS technique makes use of the characteristic X-rays which are generated due to interaction between energetic electrons and sample atoms to analyze elemental composition of the specimen. EDS is normally used as an add-on associated either with SEM or TEM. In this technique energy dispersive spectrum of the characteristic X-rays are recorded. This technique provides both qualitative and quantitative information about elemental composition of the specimen. In principle all the elements from Be ($Z = 4$) upto U ($Z = 92$) can be detected with this technique tough all the instruments are not equipped with detection of light elements ($Z < 10$) [84]. Qualitative analysis involves identification of elements from photon energy of the characteristic X-rays. Quantitative analysis (determination of the concentration of elements present in the sample) involves measuring line intensities for each element in the sample and for the same elements in the calibration standards of known composition. Element distribution map is obtained by scanning the electron beam in raster manner and recording signal (characteristic

X-rays) as a function of position. In EDS X-ray intensities are measured by counting photons hence obtainable precision is limited by statistical error. Overall accuracy of EDS analysis is typically nearer to ± 2%. Using common procedures detection limit of element is ~1000 ppm by weight but it can be reduced by using long counting times. Spatial resolution is governed by interaction volume of electrons in specimen hence it is a function of density of the specimen. Since the electron probe analyses only to a shallow depth, specimen should be polished to remove surface roughness. Specimen to be analyzed in EDS should be conducting. If specimen is non-conducting a conducting surface coat must be applied to provide a conducting path for incident electrons. The usual coating material is carbon (~10 nm thick), which has a minimal influence on X-rays intensities on account of its low atomic number [84].

2.3.3 Surface profilometer

Surface profilometer is a device which provides information about surface topography (surface features, roughness, curvature etc.) of the specimen [85]. Topographical information can be taken from a single point, line scan or even area scan. Surface profilometers are of two types – (i) contact- stylus based profilometer (ii) non-contact (optical profilometer). Stylus based surface profilometer uses a physical probe to measure surface profile. This probe touches the sample surface and moves to acquire surface profile. This is done mechanically with feedback loop that monitors the force from the sample pushing up against the probe as it scans along the surface. A feedback system is used to keep the arm with specific amount of torque on it known as set point. The changes in the Z position of the arm holder are used to reconstruct surface. On the other hand optical profilometery is a non-contact technique to extract much of same information about surface topography as obtained via stylus based profilometer. It uses light instead of a physical probe to get surface profile. Various techniques are being currently employed in optical surface

profilometers such as laser triangulation, low coherence interference, confocal microscopy and digital holography. Advantages of surface profilometers are high speed, reliability, and better lateral resolution, with limited chance of damaging specimen surface. Typical lateral resolution in optical profilometers ranges from few microns down to submicron [86].

2.3.4 Raman Spectroscopy

Raman spectroscopy is a spectroscopic technique which works on the principle of Raman scattering and provides information about the molecules present in specimen. Raman scattering is the process of inelastic scattering of monochromatic light due to interaction with vibrating/rotating molecules. Inelastically scattered photons will be either of reduced frequency (Stoke shift) or increased frequency (anti-Stoke shift). Change in frequency of scattered photons with respect to frequency of incident photons (Raman shift) depends upon mode of rotation/vibration of the molecules. Therefore measurement of Raman shift provides fingerprint about the molecules present in the sample. A Raman spectrum which records intensity of Raman signal as function of shift in wavenumber provides insight about chemical composition of the sample [87, 88]. Schematic diagram of a typical Raman spectrometer is shown in Fig. 2.4.

In the present study an unpolarized micro-Raman spectrometer has been employed for characterization of laser modified specimens. In this spectrometer frequency doubled diode pumped Nd:YAG laser is used as excitation source. This laser delivers laser beam at 532 nm wavelength in continuous wave (CW) mode. Average output power of the excitation laser in 100 mW. Excitation laser beam power level to be sent on sample surface is controlled via neutral density (ND) filter. Raman signal is also collected and send to spectrometer using optical fiber.

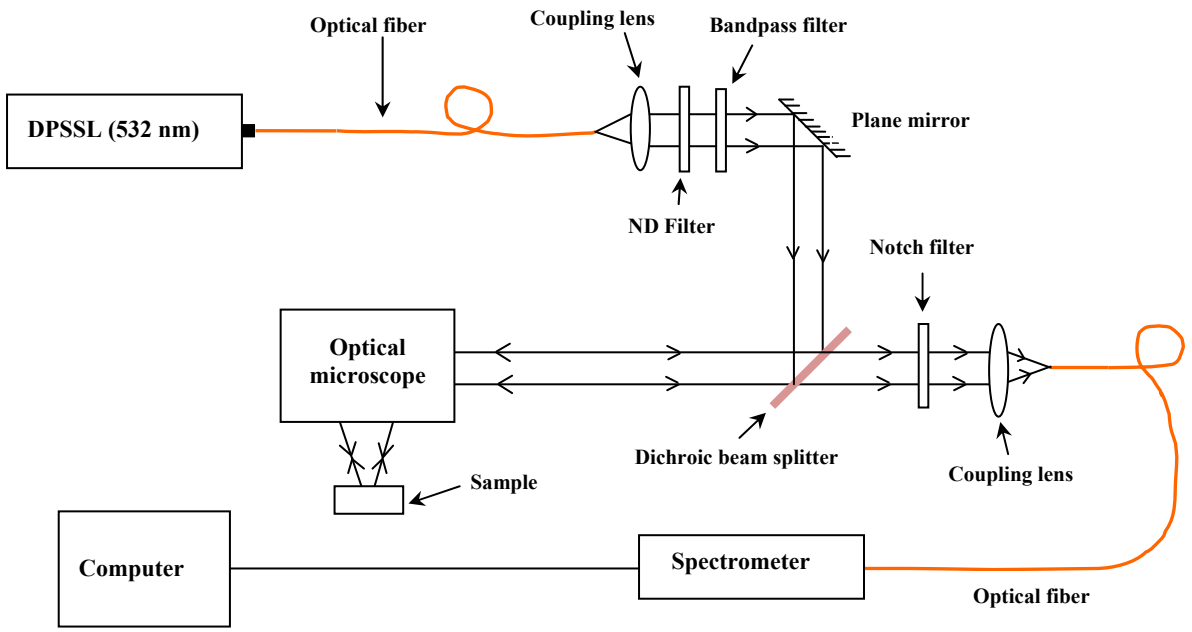

Figure2.4 Schematic diagram of a fiber coupled micro-Raman spectrometer.

2.3.5 Grazing incidence X-Ray diffraction (GI-XRD)

X-ray diffractrometry is a technique based on principle of diffraction of monochromatic X-ray radiation. Diffraction of the X-ray radiation from crystalline sample is governed by Bragg's law. According to Bragg's law when X-ray of wavelength (λ) is incident on surface of the sample with inter planar spacing d, maxima of the diffracted X-ray beam occurs at certain angles (θ) with respect to normal of the plane. Governing equation for diffraction is as following [89]–

$$2dsin(\theta) = n\lambda \text{ ---------- (2.1)}$$

Here, n is an integer called order of diffraction. Intensity of the X-ray beam vs diffraction angle is called diffraction pattern which provides information about crystal structure, residual stress, defects in specimen. Generally to study crystal structure of bulk materials θ-2θ (Bragg-Brentano) type diffractometer is used. In normal XRD, where typically larger angle of incidence of X-ray beam (>20^o) is used, X-ray beam penetrates deep inside the specimen and X-ray diffraction

signal comes from depth of the surface. Therefore, to analyze crystal structure of thin films or thin surfaces GI-XRD technique is employed [89]. In GI-XRD, a parallel monochromatic X-ray beam is incident at very small incident angle in the range 2^o to 5^o with respect to sample surface and diffraction pattern is recorded. An advantage of GIXRD is that in this case penetration depth of the X-rays is limited hence diffraction pattern mainly contains information on thin surface layer. However, a disadvantage in this case is the limited in-plane spatial resolution (due to large beam footprint [89]

2.3.6 X-Ray photoelectron spectroscopy (XPS)

XPS or electron spectroscopy for chemical analysis (ESCA) is a surface analysis technique which provides information about elemental composition and chemical state from outer 5 to 10 nm of the solid surface. It can detect all elements from lithium (Li) to uranium with an accuracy of 0.1 to 0.5 atomic percentages [90].

In this technique sample is irradiated with an X-ray beam of known photon energy (hν) under ultra-high vacuum. These X-ray photons interact with atoms and eject electrons from core shell of the atoms via photoelectric effect. Intensity and kinetic energy (K.E.) of the emitted electrons are measured to identify element and its concentration. Binding energy of the atom with respect to Fermi level is inferred from the measured K.E. of the emitted electrons by following equation-

$$E_b = h\nu - E_k - \varphi_{sp} \quad \text{……..(2.2)}$$

Where E_b, E_k and $\varphi_{sp}$are binding energy of electron in atom, kinetic energy of the ejected electron and work function of the target, respectively. Binding energy of the atom renders information about the atomic number of the atom and its chemical environment because binding

energy of atom depends upon chemical environment. An XPS spectrum shows ejected electrons count vs binding energy which provides information about the concentration of different elements and their ionization state.

2.3.7 Kelvin Probe Microscopy

Kelvin probe microscopy is a non-contact technique to measure work function of a specimen. This technique works on the principle of contact potential difference (CPD) measurement between a specimen and a standard probe (normally gold). When two materials with different work functions come closer to form a capacitor equal and opposite charges are generated on the two surfaces due to work function difference a potential is developed between the two surfaces. This potential is known as CPD. If the specimen and the standard probe have work functions has φ_1 and φ_2, respectively then CPD between sample and standard probe will be the two materials is given by [91] –

$$CPD = (\varphi_1 - \varphi_2) / e \qquad \ldots\ldots\ldots\ldots (2.3)$$

Here, e is electronic charge. Since work function of the standard probe is known, work function of the specimen can be estimated by measuring CPD between sample and the standard probe. Basic principle of the CPD measurement in Kelvin probe is to apply external potential between to two surfaces until potential between then disappears completely.

2.3.8 Field emission characterization setup

In field emission characterization total emission current as a function of applied electric field between electrodes was measured. Field emission characterization of the specimens has been carried out under ultra-high vacuum. In the present study typical vacuum during FE characterization were in the range $1x10^{-7}$ to $1x10^{-8}$ mbar. Electrodes were used in plane-plane

geometry for field emission characterization. Schematic diagram of the field emission characterization setup is shown in Fig. 2.5.

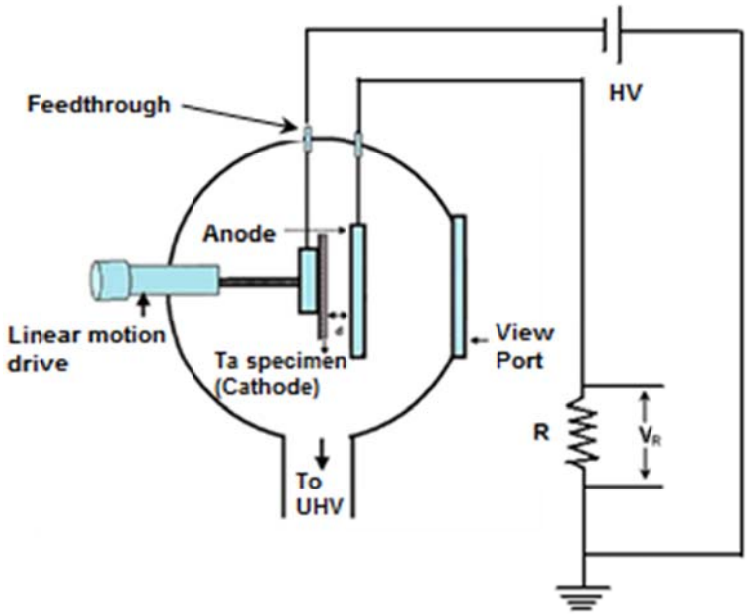

Fig. 2.5 Schematic diagram of the field emission characterization setup [92].

Vacuum chamber was mainly divided into two compartments (primary compartment and secondary compartment) separated by a gate valve. In the main compartment of the vacuum chamber where cathode (laser micro-structured specimen) and anode were kept during FE characterization ultra-high vacuum was maintained. On the other hand, pressure of the secondary chamber was kept in the range $1x10^{-5}$ mbar to $1x10^{-6}$ mbar and it was connected to main chamber only at the time of loading or removing samples. To load the sample for field emission characterization secondary chamber is kept isolated from main chamber with the help of a gate valve and it is vented to atmosphere. Sample is mounted on a sample holder in the secondary chamber and then chamber is evacuated using a combination of a rotary pump and a turbomolecular pump. Once vacuum in secondary chamber is reached ~10^{-6} mbar this chamber is connected to main chamber which is already under ultra-high vacuum and sample is transferred

to main chamber. After transferring sample to main chamber secondary chamber is again isolated from the main chamber. Ultra high vacuum in the chamber is achieved using a combination of rotary pump, turbomolecular pump, sputter-ion pump and pouring liquid nitrogen. A negative DC high voltage on the cathode surface is applied using Spellman high voltage power supply with the help of feed-through. Anode in this experimental facility was made of a transparent conducting material of diameter (40 mm). Separation between anode and cathode is varied by moving cathode surface with the help of micrometer based linear drive arrangement. Applied voltage on cathode surface was varied by varying output voltage of the power supply and corresponding field emission current was extracted from the measured voltage drop (V_R) across a 100 kΩ resistance (R) connected in series between anode and ground. To check stability of field emission current voltage drop across the 100 kΩ resistance was measured as a function of time and recorded at every 10 s interval with the help of a data logger. The recorded voltages were converted in to current.

Chapter 3

Nanosecond Laser Based Micro-structuring of Stainless Steel 304 and Tantalum Surfaces for Enhanced Field Emission

3.1 Introduction

Surface morphology plays a vital role in field emission performance of a field emitting cathode (FEC). Therefore, extensive research has been carried out in recent past for generation of different surface morphologies on FECs and characterization of their field emission properties (as listed in Section 1.8). Key objectives of these studies are to achieve− high field emission current along with high current density at low operating electric field, stable field emission current under relatively poor vacuum conditions, long lifetime, low emittance of the emitted electron beam etc. Reported works listed in section 1.8 have shown that cathodes with surface micro/nano structures demonstrate improved field emission behavior. The observed enhancement of field emission current from FECs occurs on account of local electric field enhancement on cathode surface. Enhancement of the applied electric field on cathode surface depends on shape, size and number density of the surface micro-structures.

Nanosecond and femtosecond laser based surface micro-structuring of materials has demonstrated improved performance of materials in variety of applications (as listed in Section 1.3). Nanosecond laser systems are low cost and robust system in comparison to the femtosecond lasers.

Stainless steel 304 (SS 304) and tantalum (Ta) targets have been surface micro-structured using nanosecond (ns) laser owing to its offered advantages. Objective of these surface micro-

structuring experiments were to investigate effect of processing parameters on surface morphology and enhanced field emission behavior.

This chapter presents our results on ns laser based surface micro-structuring of SS 304 and Ta surfaces and their characterization. Surface micro-structuring of targets has been carried out by irradiating them in air using a focused beam of a ns pulsed Nd:YAG laser. Laser micro-structured specimens have been characterized in terms of surface micro-morphology, roughness, changes in chemical phase on laser treatment and field emission characteristics. Parameters characterizing surface micro-structured specimens as field emitter have been derived from the experimental data.

3.2 Surface micro-structuring of stainless steel 304 targets

3.2.1 Experimental details

Surface micro-structuring of SS 304 targets have been carried out by direct irradiation in atmospheric air. Experimental setup employed for surface modification is described in Section 2.1 of Chapter 2. SS 304 targets used for these experiments were small samples of commercially available SS 304 sheet of typical dimensions− Length: ~1 cm, Width: ~1 cm, Thickness: ~0.05 cm. To investigate effect of laser fluence and cumulative number of irradiating laser pulses on the formed surface microstructure, laser fluence and number of pulses were varied in the range 0.7 J/cm^2 to 10 J/cm^2 and 3000 to 9000, respectively. Laser fluence levels mentioned in our experiments are space averaged values which are defined as the ratio of incident pulse energy to laser spot area. In the first set of experiments laser fluence was varied in the range 2 J/cm^2 to 10 J/cm^2 and samples were irradiated at different spots with varying number of pulses in the range 3000 to 9000. These specimens were characterized in terms of surface micro-structure using scanning electron microscopy (SEM) technique. SEM images were taken by mounting surface

modified specimens at inclination of ~30°−40°. SEM images of the regions where micro-protrusions are formed were further analyzed using Leica Qwin3 software attached with an optical microscope (Make: Leica, Model: DM ILM inverted optical microscope) to estimate average height of the generated protrusions. Based upon observations from the first set of experiments on surface micro-structuring of SS 304 subsequent experiment was planned to carry out SS 304 surface modification at lower laser fluence. Based on these runs optimized laser parameters were selected.

SS 304 specimen was finally micro-structured with 6000 laser pulses at laser fluence of 0.7 J/cm^2 and characterized in terms of surface micro-structure, elemental composition, roughness and field emission behavior. During the field emission characterization vacuum in the chamber was maintained at ~1 x 10^{-8} mbar and separation between anode and cathode (SS 304 specimen) was kept at 0.5 mm. Some of the important parameters characterizing a large area field emitter have been extracted using the experiment data on variation of macroscopic emission current density versus applied macroscopic electric field.

3.2.2 Characterization results on SS 304 samples

3.2.2.1 Surface morphology characterization

SEM images showing surface morphology of the spots irradiated with 3000 laser pulses and varying laser fluence in the range 2 J/cm^2 to 10 J/cm^2 are shown in Figs. 3.1 (a−d). These SEM images show that surface micro-protrusions are formed in laser irradiated region preferably near periphery of the spot. In the case of target irradiation with 2 J/cm^2 micro protrusions are also formed towards central part of the region where local laser fluence is low. SEM images also show that prominent crater is formed within the spots treated at laser fluence levels ≥ 4 J/cm^2. Hence, to avoid deep crater formation within laser irradiated spots laser fluence used for surface

micro-structuring was limited to 2 J/cm^2. SS targets were again irradiated with 6000 and 9000 laser pulses while keeping incident laser fluence fixed at 2 J/cm^2 to investigate effect of number of laser pulses on surface micro-structure. Surface micro-structure of the spots treated with 6000 and 9000 pulses at 2 J/cm^2 laser fluence are shown in Figs. 3.2 (a–b). Figs. 3.3 (a–b) show magnified SEM image of spots irradiated with 6000 and 9000 laser pulses. The images in Figs. 3.2 & 3.3 clearly show the formation of surface micro-protrusions of increased height in comparison to generated micro-protrusions in the spot treated with 3000 laser pulses at same laser fluence [Fig. 3.1 (a)].

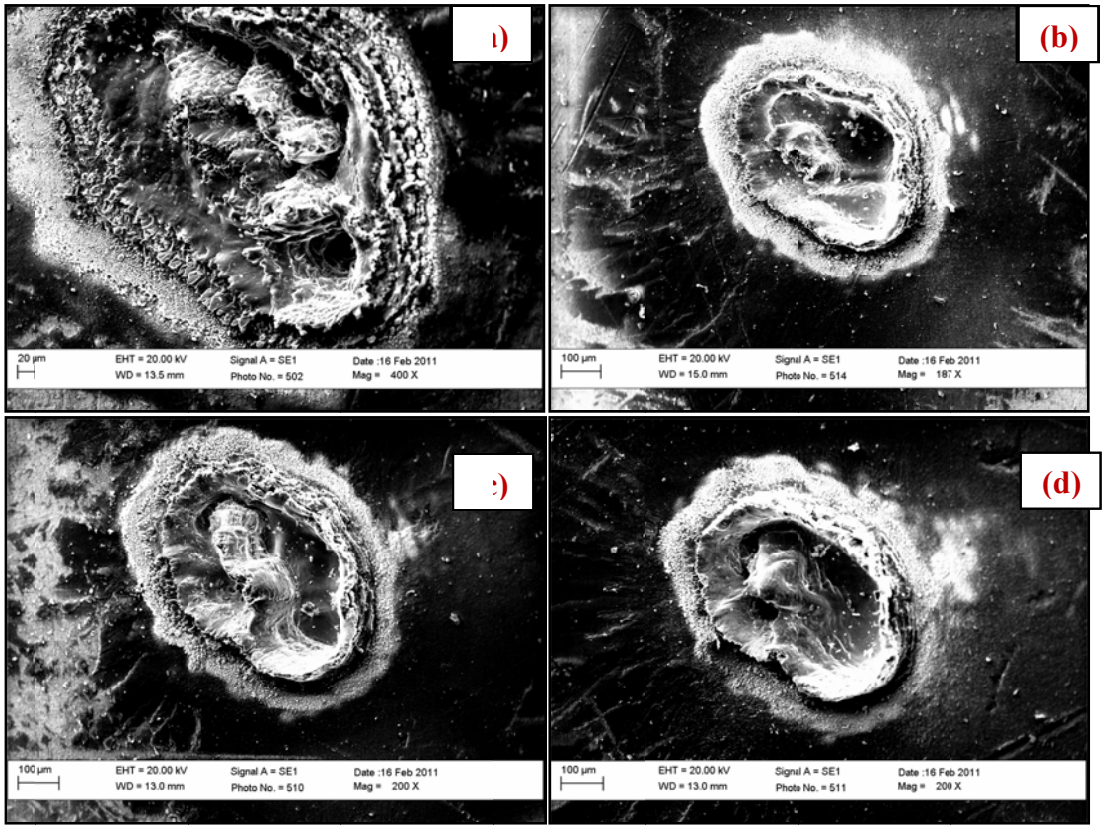

Figure 3.1 SEM images of the spots on SS 304 target irradiated with 3000 laser pulses at laser fluence of (a) 2 J/cm^2 (b) 4 J/cm^2 (c) 6 J/cm^2 (d) 10 J/cm^2 [93].

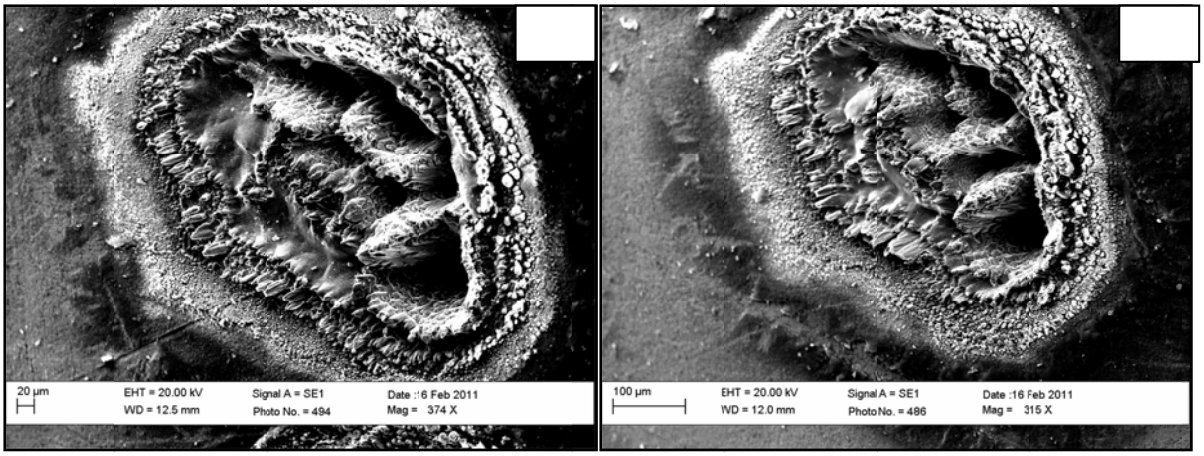

Figure 3.2 SEM images of the spots irradiated at laser fluence of 2 J/cm^2 with (a) 6000 laser pulses (b) 9000 laser pulses [93].

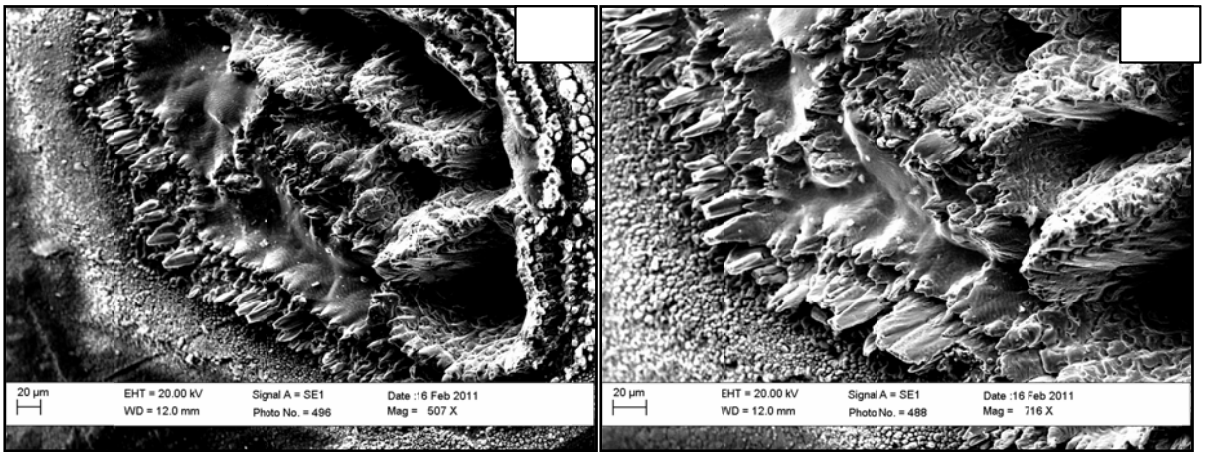

Figure 3.3 Magnified SEM images of spots irradiated at fluence level of 2 J/cm^2 and number of laser pulses equal to (a) 6000 (b) 9000 [93].

Analysis of the SEM images of the regions treated with 3000, 6000 and 9000 laser pulses at laser fluence level of 2 J/cm^2 using Leica Qwin3 software revealed that mean height of the surface micro-protrusions grown in periphery of the laser treated spot increased with increasing number of incident laser pulses. Observed variation in the mean height of surface micro-structures with number of incident laser pulses is shown in Fig. 3.4.

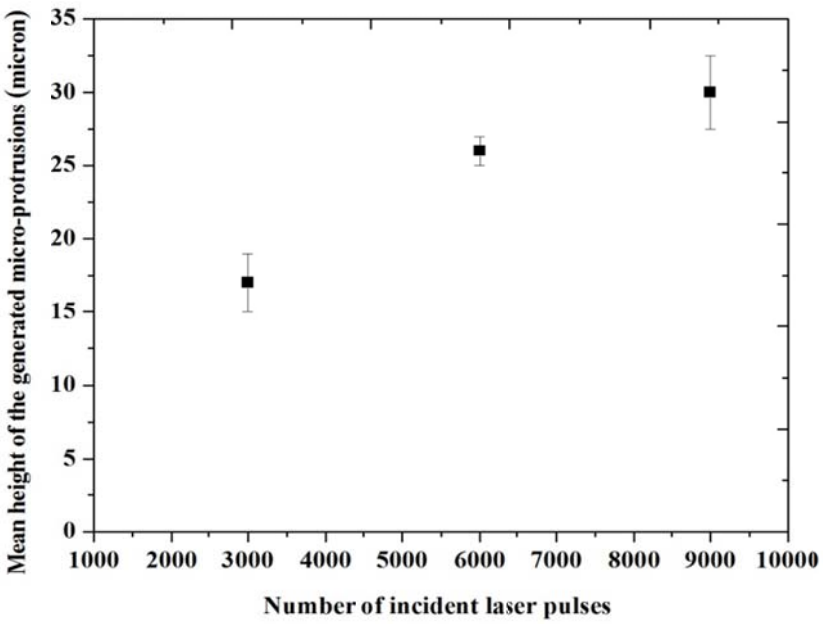

Figure 3.4 Variation of mean height of surface micro-protrusions with number of laser pulses [93].

Plotted error bar on each data point shows range of estimated mean value in three different attempts of analysis. It is clear from Fig. 3.4 that increasing number of laser pulses from 3000 to 6000 resulted in increase in mean height (h_{av}) of the micro-protrusions from 17 μm to 26 μm i.e. h_{av} increased by 9 μm when number of laser pulses increased by 3000. Further, when the SS target was irradiated with 9000 laser pulses h_{av} of generated the micro-protrusions increased to 30 μm i.e. increase in h_{av} of micro-protrusions in comparison to specimen treated with 6000 laser pulses was only by 4 μm. This indicated that initial growth rate of surface micro-protrusions (change in height per incident laser pulse) was high, subsequently it slow down after certain number of incident laser pulses. These observations are in agreement with the observations reported in literature for micro-structure evolution of laser irradiated silicon targets both with nanosecond and femtosecond laser pulses [94, 95].

It was observed from Fig. 3.1(a) that even in the spot irradiated at 2 J/cm^2 some amount of crater was formed in the spot owing to hot spot present in the laser beam. Therefore, to avoid

formation of crater within the laser irradiated spot laser fluence was further reduced and surface modification was carried out using laser fluence of 0.7 J/cm^2 and irradiating with 6000 laser pulses. SEM images showing surface micro-structures of the laser modified regions corresponding to 0.7 J/cm^2 at different magnification levels are shown in Fig. 3.5 (a-d).

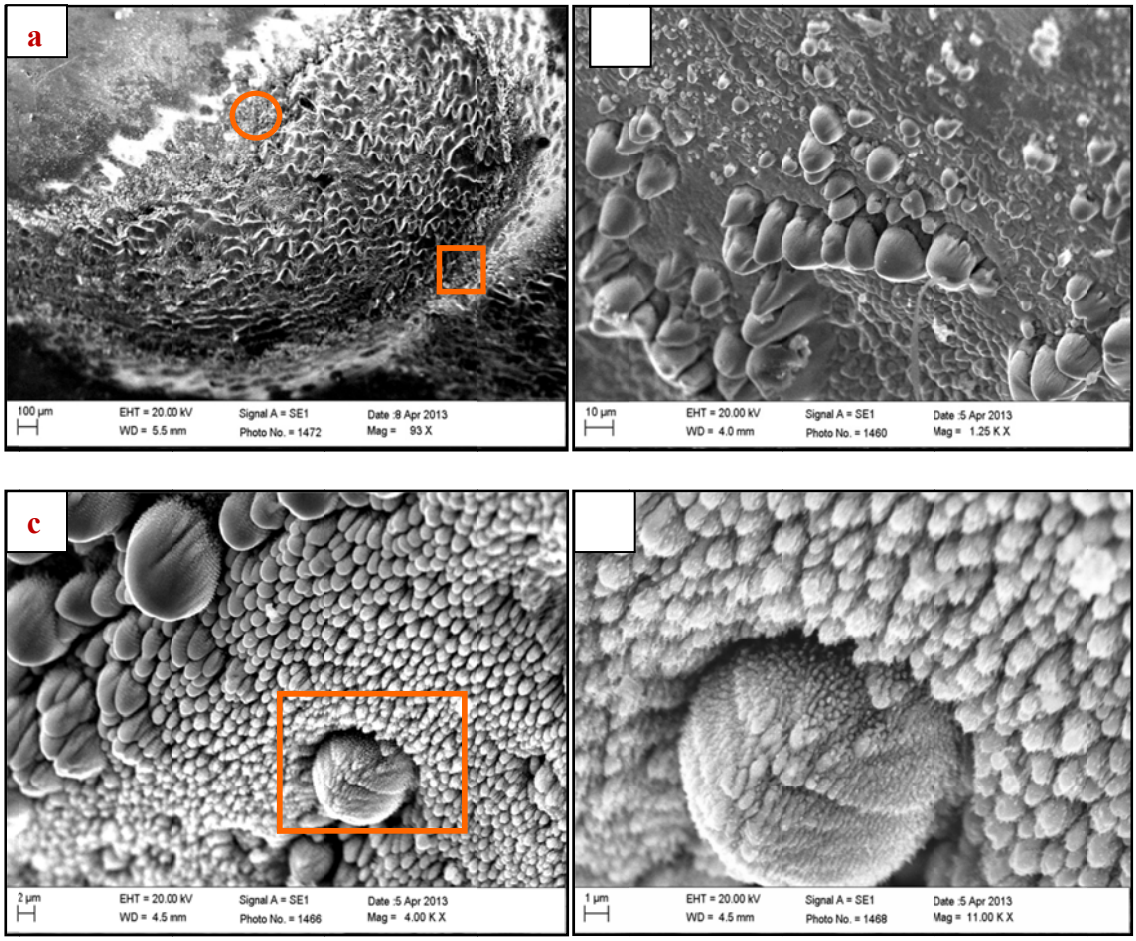

Figure 3.5 (a—d) SEM images of different regions of the spot irradiated with 6000 laser pulses at laser fluence of 0.7 J/cm^2. Fig. 3.5 (a) shows surface morphology of the laser treated spot at low magnification. Fig. 3.5 (b) shows magnified image of the encircled region in Fig. 3.5 (a). Fig.3.5 c shows magnified image of the region indicated by square in image 3.5(a). Fig. 3.5 (d) shows further magnified SEM image of the region indicated as rectangle in image 3.5 (c) [96].

Fig. 3.5 (a) revealed that no crater was formed within the laser treated region and surface micro-protrusions have been generated within the entire treated region. Different sections of the laser treated spot contain micro-structure of varying height and diameter. High density of surface micro-protrusions shown in Figs. 3.5 (c) and (d) refer to the regions marked by a square within the laser treated spot shown ion Figs. 3.5 (a) and 3.5 (c), respectively. Average density of micro-protrusions estimate within the rectangular region in Fig. 3.5 (c) was ~4.5×10^7 micro-protrusions/cm^2. As no crater was formed in the specimen treated at laser fluence of 0.7 J/cm^2 this micro-structured specimen was further characterized for surface roughness, change in chemical composition, crystallographic phase and field emission behavior.

Mean roughness and peak height of the generated surface micro-features in the region treated with 6000 laser pulses at laser fluence of 0.7 J/cm^2 were estimated by 3-dimensional (3D) surface profiling technique. A typical surface profile of the laser irradiated spot is shown in Fig. 3.6.

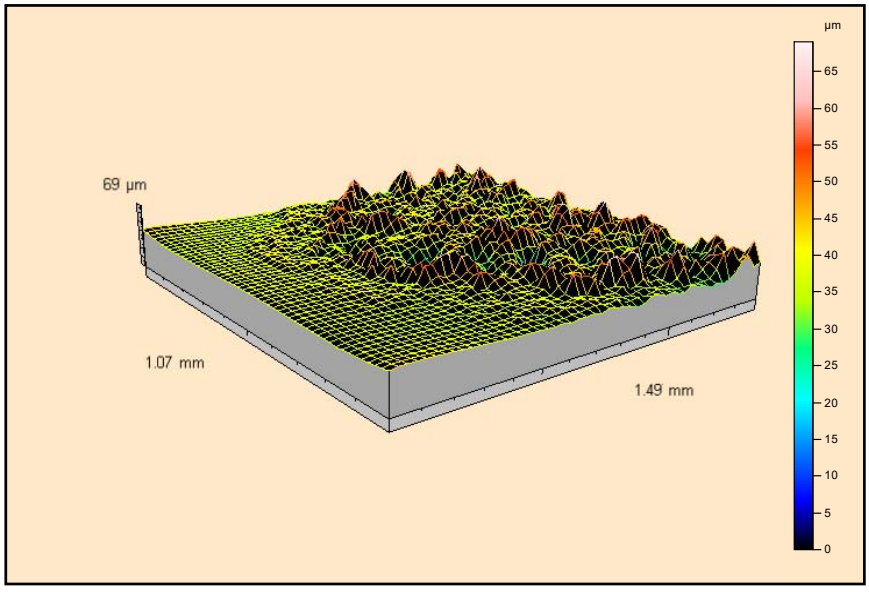

Figure 3.6 3D Surface profile of the SS sample treated with 6000 laser pulses at fluence of 0.7 J/cm^2[96].

It is evident from the Fig. 3.6 that micro-structures formed on laser treatment are projected outward with respect to the target surface. Also, surface roughness of the untreated region of the sample is negligible in comparison to laser treated surface. Estimated maximum height of the generated micro-protrusions above the mean plane of the specimen was ~30 μm.

Formation of surface μ-protrusions upon laser irradiation can be explained on the basis of laser induced melting and vaporization of surface and associated melt pool surface instability [97]. Laser irradiation of the target surface causes melting and evaporation of the target material up to certain depth. Due to rapid and localized melting of the target surface strong temperature gradients exists along lateral as well as depth directions in the melt-pool leading to flow of liquid driven by thermo-capillary forces. Thermo-capillary driven flow of liquid along with the recoil pressure exerted by evaporating atoms on melt surface causes melt surface instability resulting in formation of surface undulations. These formed surface undulations remain on the surface provided re-solidification time of the molten layer is shorter than the time required for surface to reach in equilibrium (capillary wave period). The initial surface undulation is composed of many spatial frequency components out of which a particular frequency component having highest growth rate dominates for next incoming laser pulses depending upon melt-pool geometry, laser fluence and material thermo-physical properties. Therefore, when target surface is irradiated by a large number of laser pulses surface μ-protrusions with periodicity corresponding to highest growth rate is formed on the laser irradiated surface.

3.2.2.2 Energy dispersive X-ray spectroscopy (EDS) characterization

Elemental composition of untreated sample and the sample treated with laser fluence of 0.7 J/cm^2 were characterized using EDS technique. Obtained composition for the two samples is summarized in Table 3.1.

Table 3.1 Elemental composition of untreated and laser modified SS samples obtained from EDS.

Element	Untreated steel sample	Laser treated steel sample	Change in atomic concentration upon laser treatment (at.%)
	Normalized atomic concentration (at.%)	Normalized atomic concentration (at.%)	
C	8.51	6.18	- 2.33
N	-	7.11	+7.11
O	1.65	25.92	+24.27
Al	-	0.11	+0.11
Si	0.54	0.05	-0.04
Cr	18.27	11.08	-7.19
Fe	64.16	44.24	-19.92
Ni	6.87	5.31	-1.56
Total	100	100	-

EDS results revealed that laser modification of SS 304 specimen leads to an increase in the concentration of oxygen (O) and Nitrogen (N) and reduction in the concentration of iron (Fe), chromium (Cr), nickel (Ni) and carbon (C) in the surface layer. The observed higher C concentration in untreated SS 304 sample in comparison to its typical concentration in SS 304 could be an artifact due to background count. As in the present experiments laser irradiation was carried out in atmospheric air increase in O and N concentration is expected on account of iron oxide and nitride formation due to laser induced heating of sample surface in air. Although, concentration of different elements in target presented in Table 3.1 is not truly quantitative because of limitations of EDS technique it broadly indicates trend and relative concentration of

elements upon laser treatment. These observations are also in agreement with observed trend of elemental concentration reported for laser treatment of stainless steel surface using an excimer laser in Ref. [98].

3.2.2.3 Grazing incidence X-ray diffraction (GIXRD) results

To investigate presence of phases of oxides and nitrides formed on laser treatment untreated and laser treated specimens were characterized using GI-XRD technique. GI-XRD pattern for both the samples was recorded by using 1^{o} angle of incidence for the X-Ray beam with respect to sample surface. GI-XRD patterns of untreated and laser treated samples are shown is Fig. 3.7.

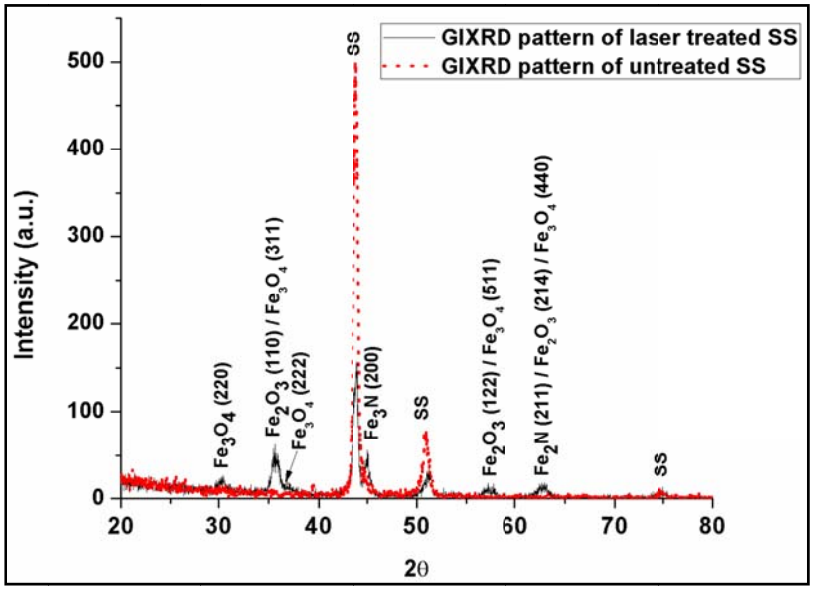

Figure 3.7 GI-XRD patterns of the untreated and the sample micro-structured with 6000 laser pulses and at laser fluence of 0.7 J/cm^2 [96].

GI-XRD results revealed the untreated surface does not contain iron oxide or nitride while laser treated surface consisted of mainly iron oxides and nitrides. Observed diffraction peaks at 2θ angles 30.4^{o}, 35.6^{o}, 37^{o} and 57.2^{o} match those due to iron oxides [Fe_2O_3 (pdf # 890599) and Fe_3O_4 (pdf # 890950)] and diffraction peak corresponding to 2θ value 45^{o}, suggests formation of

Fe_3N (pdf # 830879). Diffraction peak at 63^o could be due to iron oxide/nitride or mixture of the two (Fe_2N (pdf # 732102)). These observations indicate formation of iron oxides and nitrides in the laser treated region confirming observation obtained from the EDS technique.

3.2.2.4 Field emission characterization results

Macroscopic field emission current density (J_m) as a function of macroscopic applied field (E_m) corresponding to SS 304 specimen surface micro-structured with laser fluence of 0.7 J/cm^2 is shown in Fig. 3.8. FE characterization of untreated SS specimen showed that untreated sample delivered only few nA/cm^2 of emission current density even when E_m was increased up to 11.4 V/μm. The observed emission current density (J_m) from the untreated specimen was negligible in comparison to delivered J_m from laser modified specimen. Hence, J_m versus E_m characteristics for untreated sample has not been plotted. Here, E_m and J_m have been defined as the ratio of the applied voltage (V) to the separation between the electrodes (d) and total emission current divided by the total laser treated surface area of the sample, respectively. In estimation of J_m only surface micro-structured area has been taken in to account due to the fact that untreated SS specimen did not deliver significant emission current for the entire range of electric field used for FE characterization. Turn on field (E_{on}) which is defined as the E_m required for generating J_m equal to 10 μA/cm^2 is found to be 7.5 V/μm for laser micro-structured SS surface [96]. This magnitude of E_{on} is significantly lower than the corresponding values for untreated SS sample. Emission current density delivered by laser treated specimen in the present study is significantly higher than the emission current density reported from a SS specimen with surface roughness ~1 μm delivering J_m equal to ~0.3 μA/cm^2 at applied E_m equal to 15 V/μm [99]. Observed enhanced field emission for the laser micro-structured SS surface is due to enhancement of local electric field on the tip of generated surface. This locally enhanced electric field is sufficient to cause

emission of electrons by quantum mechanical tunneling effect. Inset of the Fig. 3.8 shows photograph of the fluorescence produced on anode surface by striking field emitted electrons.

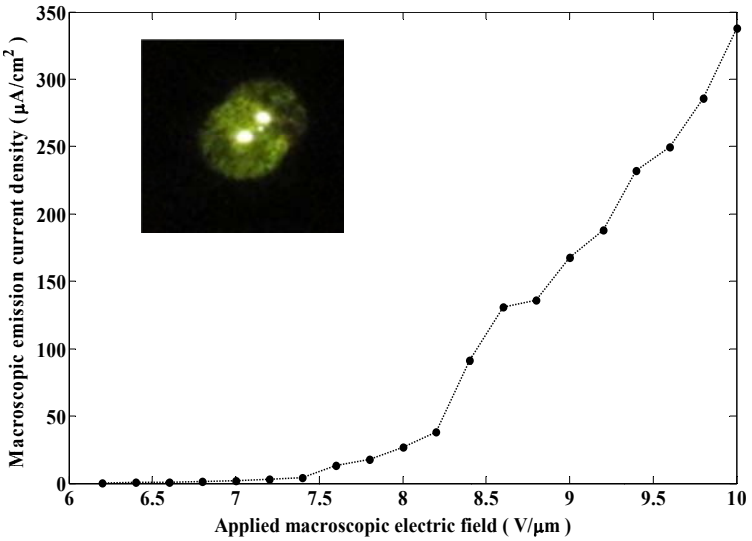

Figure 3.8 J_m versus E_m characteristics of the SS 304 sample laser micro-structured with 6000 laser pulses at laser fluence of 0.7 J/cm^2 [96].

A large area field emitter (LAFE) is characterized by many parameters, such as, turn on field (E_{on}), threshold field (E_{th}), macroscopic field enhancement factor (β_m), maximum delivered macroscopic emission current density (($J_m)_{max}$), formal area efficiency of emission (α_m) and field emission current stability. Here, field enhancement factor is defined as the ratio of the mean value of the electric field on tips of protrusions to the macroscopic applied field (E_m) and E_{th} is normally defined as the required E_m for generating J_m equal to 100 μA/cm^2. ($J_m)_{max}$ is the maximum current which a emitter delivers before start of current fluctuation because of arcing phenomenon. Area efficiency of emitter indicates how much fraction of the emitter surface is actually emitting electrons. E_{th} and ($J_m)_{max}$ for the laser modified specimen were measured to be ~8.5 V/μm and 340 μA/cm^2, respectively. Most of the aforementioned parameters can be

estimated from J_m versus E_m characteristics of the specimen using Fowler-Nordheim (F-N) theory.

According to technically complete F-N theory macroscopic field emission current density (J_m) from a LAFE surface can be expressed as [45] ─

$$J_m = \lambda_m a\varphi^{-1} (\beta_m E_m)^2 \exp(-\nu_F b\varphi^{3/2}/(\beta_m E_m)) \quad \ldots\ldots\ldots\ldots\ldots (3.1)$$

Here, λ_m, a (=1.541434 $\mu A e V V^{-2}$), b (= 6.830890 $eV^{-3/2}Vnm^{-1}$), φ and ν_F are macroscopic pre-exponential correction factor, first F-N constant, second F-N constant, work function of the emitter surface and barrier form correction factor, respectively. Here, ν_F is the correction introduced due the actual form of the potential barrier which is deviated from triangular shape.

Plot showing variation of ln (J_m/E_m^2) as a function of $1/E_m$ is known as F-N plot. Macroscopic field emission enhancement factor (β_m) on the laser treated samples can be estimated using slope of $\ln(J_m/F_m^2)$ vs $1/F_m$ type F-N plot by following equation [45]─

$$\beta_m = -\chi_m b\phi^{3/2}/S \quad \ldots\ldots\ldots\ldots (3.2)$$

Here, χ_m and S are generalized slope correction factor, and slope of the F-N plot of type $\ln(J_m/F_m^2)$ vs $1/F_m$, respectively. When emission current density is purely due to field emission process from cathode surface and no leakage current and field effects are present then χ_m is equal to Schottky-Nordheim (SN) barrier form function. F-N plot of the experimental data on J_m–E_m characteristics for laser modified sample and its linear fit are shown in Fig. 3.9.It is observed from Fig. 3.9 that F-N plot is nearly linear with some variation of data points around the straight line. Slope of the F-N plot shown in Fig 3.9 is -1.05×10^8 $Np.Vm^{-1}$.

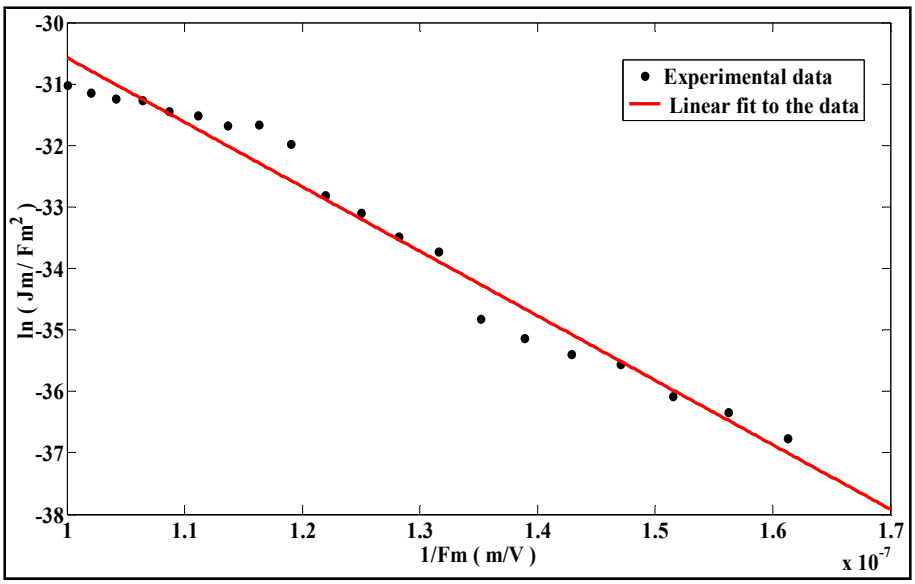

Figure 3.9 F-N plot of the experimental data on J_m vs E_m characteristics and its linear fit [96].

To estimate field enhancement factor and other parameters for the laser micro-structured stainless steel surface approach suggested in ref. [45] has been employed which is as below—

i. Experimental data on J_m–E_m was plotted as F-N plot. Slope (S) of FN plot was estimated by linearly fitting the experiment data.

ii. Generalized slope correction factor (χ_m) was estimated suing the following equation [45] –

$$\chi_m = 1/(1 + f_{Cw}^1/6) \ldots\ldots\ldots (3.3)$$

$$f_{Cw}^1 = (-9.836238)(eV/\phi)^{1/2} E_{mw}/S \quad \ldots\ldots\ldots (3.4)$$

Where, ϕ is work function, E_{mw} is known as working field and S is slope of the FN plot. E_{mw} is normally chosen as electric field value in middle of the working electric field range.

iii. Macroscopic field enhancement factor (β_m) is estimated using the equation (3.2).

iv. Macroscopic pre-exponential correction factor (λ_m) which is also a provisional estimate of the formal area efficiency of emission was estimated using the equation below –

$$\lambda_m = J_{mw}/J_c^{DD} \quad \ldots\ldots\ldots\ldots (3.5)$$

Where J_{mw} is macroscopic field emission current density corresponding to E_{mw} and J_c^{DD} is estimated using the equation [45] –

$$J_c^{DD} = \theta^{SN} f_{cw}^2 \exp\left(-\frac{\eta^{SN} v(f_{cw})}{f_{cw}}\right) \quad \ldots\ldots\ldots (3.6)$$

Here, θ^{SN}, η^{SN}, f_{cw} and $v(f_{cw})$ are estimated by following equations –

$$\theta^{SN} = (7.433980 \times 10^{11} Am^{-2})\left(\frac{\phi}{eV}\right)^3 \quad \ldots\ldots\ldots (3.7)$$

$$\eta^{SN} = 9.836238 \left(\frac{eV}{\varphi}\right)^{1/2} \quad \ldots\ldots\ldots (3.8)$$

$$f_{cw} = f_{cw}^1 / \left(1 + \frac{f_{cw}^1}{6}\right) \quad \ldots\ldots\ldots (3.9)$$

$$\left(\frac{v(f_{cw})}{f_{cw}}\right) = \frac{1}{f_{cw}} - 1 + \log(f_{cw})/6 \quad \ldots\ldots\ldots (3.10)$$

Here, for estimation of field emitter characterizing parameters work function of stainless steel (φ = 4.5 eV) has been taken in to account and the value of working field (E_{mw}) was take as 8.4 V/μm which lies nearly in the middle of the E_m range used for field emission characterization.

Estimated parameters have been summarized in Table 3.2. This table shows that macroscopic field enhancement factor (β_m) for the laser micro-structured SS surface is ~585 indicating that average value of the field on tip of the generated micro-protrusions is 585 times higher than the applied field. The macroscopic pre-exponential correction factor (λ_m) which provides provisional estimate of formal area efficiency of emission (α_m) is ~2.7 x 10^{-10} for this sample. Therefore, it implies that only a small fraction of the total sample surface is largely contributing towards field emission of electrons. High values of β_m and λ_m are envisaged for good LAFE to achieve large J_m at low applied electric field.

Stability of the field emission current from the laser modified surface has been tested over a period of 140 min at a preset current value of ~4 μA. Result of this study is shown in Fig.

3.10. Fig. 3.10 indicates that the average emission current is fairly stable over the test period. However, there are short term fluctuations in the emission current. Continuous adsorption and desorption of the gas molecules on the emitter surface and micro-explosions could be two possible reasons for the observed random fluctuations.

Table 3.2 Estimated field emitter parameters for SS 304 sample treated with 6000 pulses at laser fluence of 0.7 J/cm^2 [96].

Sr. No.	Parameter	Value
1.	Turn on electric field (E_{on})	7.5 V/μm
2.	Threshold electric field (E_{th})	8.5 V/μm
3.	Maximum delivered macroscopic current density [$(J_m)_{max}$]	340 μA/cm^2
4.	Slope of F-N plot (S)	-1.049×10^8 Np.Vm^{-1}
5.	Macroscopic field enhancement factor (β_m)	585
6.	Generalized slope correction factor (χ_m)	0.94
7.	Macroscopic pre exponential correction factor (λ_m)	2.72×10^{-10}

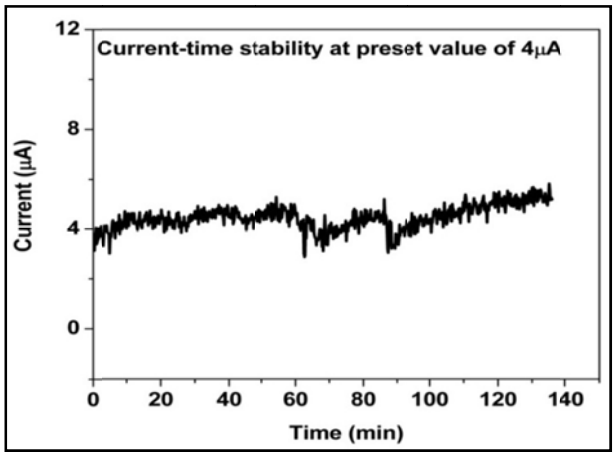

Figure 3.10 Field emission current stability of SS sample micro-structured with 6000 laser pulses/spot using laser fluence of 0.7 J/cm^2 [96].

3.3 Surface micro-structuring of Ta targets and their characterization

3.3.1 Experimental details

To carry out surface micro-structuring experiments high purity (99.99 % purity) Tantalum (Ta) foil were used as targets. Typical dimensions of the used Ta targets were - 1 cm length, 1 cm width and 100 μm thickness. These specimens were first polished using emery polishing paper of grit size 180 and then grit size 1/0. Polished Ta targets were cleaned with ethanol before using for surface micro-structuring. For laser induced surface modification these polished and cleaned targets were mounted on a computer controlled XY translational stage. Schematic of the experimental set up employed for surface modification is shown in Fig. 2.1.

Ta specimens were micro-structured by direct irradiation with focused beam of a nanosecond pulsed, frequency doubled Nd:YAG laser. Details of the nanosecond laser system used for these experiments have been presented in Section 2.1.1. Laser beam was focused using a 50 cm focal length convex lens. Target was kept at a distance of 45 cm from the focusing lens. Laser beam spot on the target surface was circular having diameter of ~1.5 mm. Laser power used for laser treatment was typically 160 mW which corresponds to an average laser fluence of 0.9 J/cm^2. During the process of laser induced surface modification the Ta target surface was kept nearly perpendicular to the incident laser beam. Target was kept stationary at one location until it received specified number of laser pulses and then it was moved by 1.5 mm along +ve X direction. Using above procedure 5 spots were made along X direction. Then target was shifted towards +ve Y direction by 1.5 mm. At this Y position of the target another 5 spots were generated by moving target along –ve X direction. Using the aforementioned procedure each Ta sample was treated at 5 x 4 spots each spot being irradiated with a specified number of laser pulses.

Surface morphology, roughness and chemical phase of the laser micro-structured specimens were characterized using SEM, surface profilometer and unpolarized micro-Raman spectroscopy. Excitation source for employed Raman spectrometer was a diode pumped solid state laser delivering average power of 100 mW at 532 nm. Excitation laser power was attenuated to 25 % using neutral density (ND) filter and 20X objective lens was used to focus laser beam on sample for Raman spectroscopic investigations. FE characterization of laser modified Ta specimens was carried out under ultra-high vacuum (~1 x 10^{-7} mbar) using the same setup used for characterization of SS 304 samples. Description of the experimental setup is provided in Section 2.2.8. Ta specimens were used as cathode, while a semitransparent anode was kept at 1 mm distance from the cathode. All other procedures for field emission characterization and data analysis were same as the procedure used for FE characterization of SS 304 samples.

3.3.2 Characterization results

3.3.2.1 Surface morphology characterization results

Figs. 3.11 (a-c) show typical SEM images of the Ta surfaces irradiated with 3000, 6000 and 9000 laser pulses, respectively. High magnification (1 kX) SEM images of surfaces treated with 3000, 6000 and 9000 laser pulses are shown in Figs 3.11 (d-f). It is clearly visible from these figures that large numbers of surface micro-protrusions are formed in the laser irradiated regions. Also, heights of undulations on target surface were found to increase with increasing number of incident pulses.

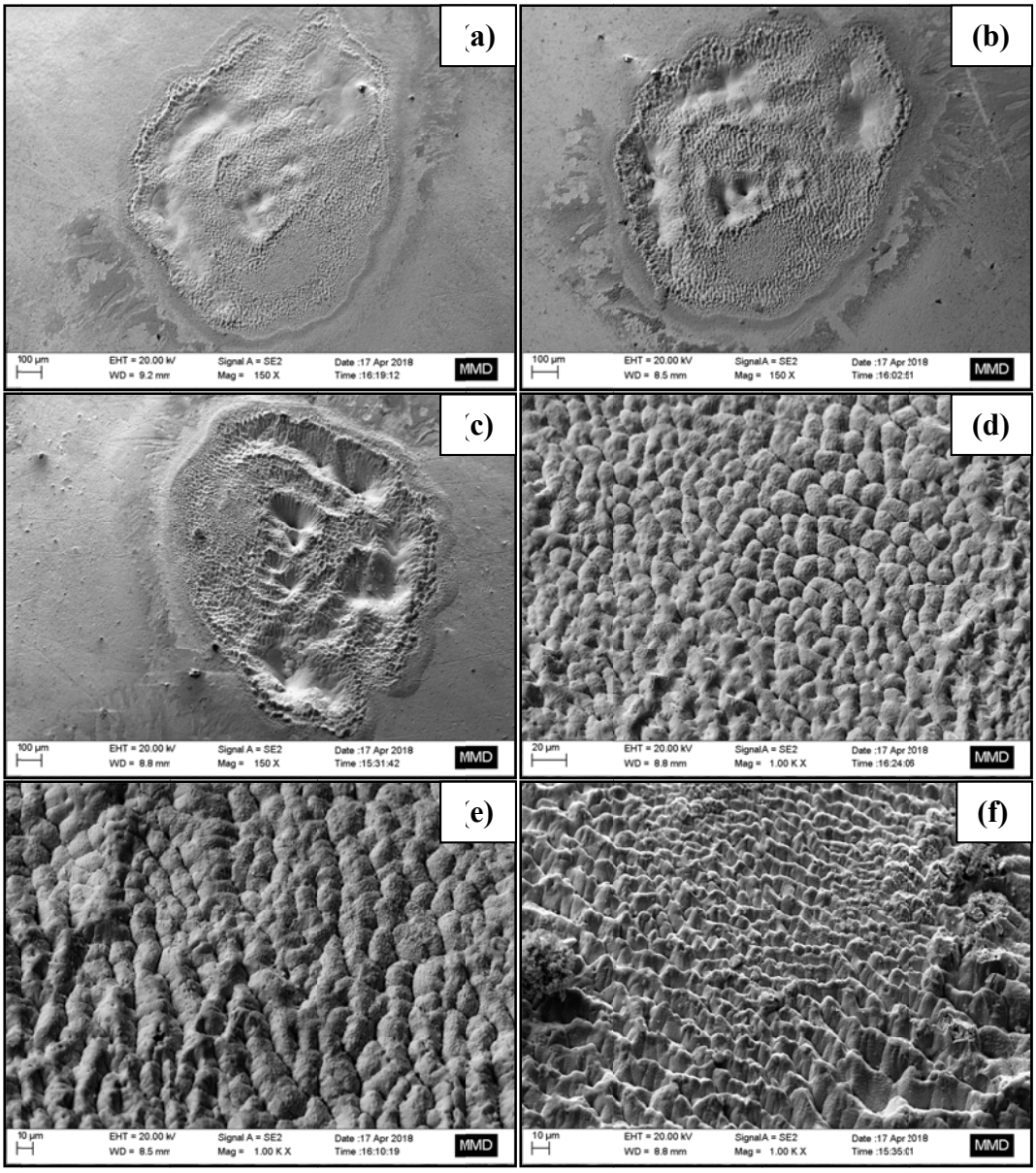

Figure 3.11 SEM images of laser treated specimens irradiated with (a) 3000 pulses (b) 6000 pulses (c) 9000 pulses (d) high magnification (1kX) image of spot irradiated with 3000 pulses (e) high magnification (1 kX) image of spot irradiated with 6000 pulses (f) high magnification (1kX) image of spot irradiated with 9000 pulses [92].

To investigate surface roughness of the laser µ-structured Ta surfaces 3D surface profiling was carried out using an optical surface profilometer. Typical 3D profiles of regions micro-structured with 3000, 6000 and 9000 laser pulses are shown in Figs 3.12 (a), (b) and (c), respectively.

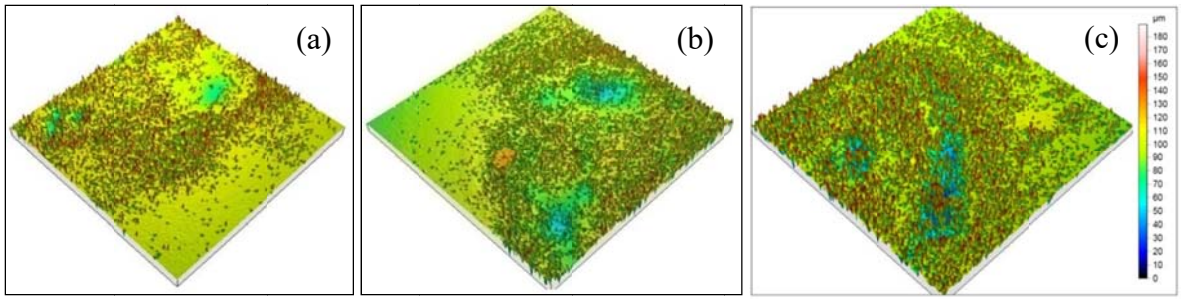

Figure 3.12 3D surface profile of the laser treated specimens irradiated with (a) 3000 laser pulses (b) 6000 laser pulses (c) 9000 laser pulses.

Average roughness (S_a) and maximum height of protrusions from base surface (S_p) estimated from figures 3 (a−c) are presented in Table 3.3. Data on surface roughness shows that S_a increased from ~7 µm to ~15 µm and S_p increased from ~50 µm to ~89 µm, as the number of incident laser pulses per spot is increased from 3000 to 9000. This observed trend of increasing S_a and S_p with increasing number of laser pulses is in agreement with the trend reported in literature. In this case of too formation and growth of these surface protrusions upon laser irradiation has been explained on the basis of hydrodynamic instability of melt surface due to strong temperature gradient in the laser irradiated region [97].

Table 3.3 Roughness parameters for Ta samples irradiated with 3000, 6000 and 9000 laser pulses.

Parameter	Sample # 1 (treated with 3000 pulses/spot)	Sample #2 (treated with 6000 pulses/spot)	Sample #3 (treated with 9000 pulses/spot)
Avg. surface roughness (S_a)	7 µm	10.2 µm	15.1 µm
Max of height of the protrusion (S_p)	50 µm	80 µm	89 µm

3.3.2.2 Raman spectroscopy results

Effect of laser treatment on the chemical phase of the target surface has been investigated using unpolarized micro-Raman spectroscopy. Raman spectra revealed that chemical phase of the laser irradiated spot varied with position within the laser irradiated spot. Raman spectra of the region near periphery of the spots irradiated with 3000 and 9000 laser pulses are shown in Figs. 3.13(a) and (b), respectively.

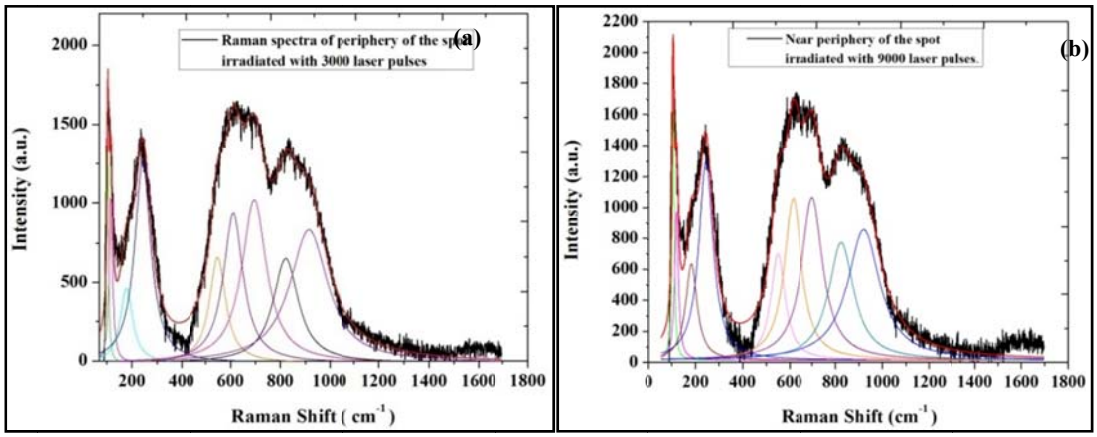

Figure 3.13 Raman spectra of the region near to periphery of the spot treated with (a) 3000 laser pulses (b) 9000 laser pulses [92].

De-convolution of the spectra 3.13 (a & b) showed Raman peaks at 105 cm^{-1}, 120 cm^{-1},183 cm^{-1}, 245 cm^{-1}, 551 cm^{-1}, 615 cm^{-1}, 700 cm^{-1}, 825 cm^{-1} and 920 cm^{-1} corresponding to Ta_2O_5 [100, 101].

On the other hand in the central region of the laser irradiated spot where large size μ-protrusions were formed none of these Raman peaks were observed indicating that this region largely remained in metallic phase [Fig. 3.14 (a & b)]. The observed metallic nature of the central region where protrusions are formed could be on account of pronounced evaporation of oxide phase, Ta_2O_5 having a lower boiling point in comparison to Ta and used laser fluence in this region being higher than the ablation threshold of both Ta and Ta_2O_5. To confirm this Ta

surface was irradiated at an average laser fluence of 0.2 J/cm^2 i.e. below ablation threshold for 1hr 15 min and investigated the surface chemical phase of the laser irradiated sample using μ-Raman spectroscopy. Raman spectra of the central and peripheral regions of spot irradiated with 0.2 J/cm^2 are shown in Figs. 3.15 (a & b), respectively. Both the figures [3.15 (a & b)] show Raman peaks corresponding to Ta_2O_5indicating formation of Ta_2O_5 in both the regions. These observations support our conjecture on absence of tantalum oxide phase in central region of the laser treated spot.

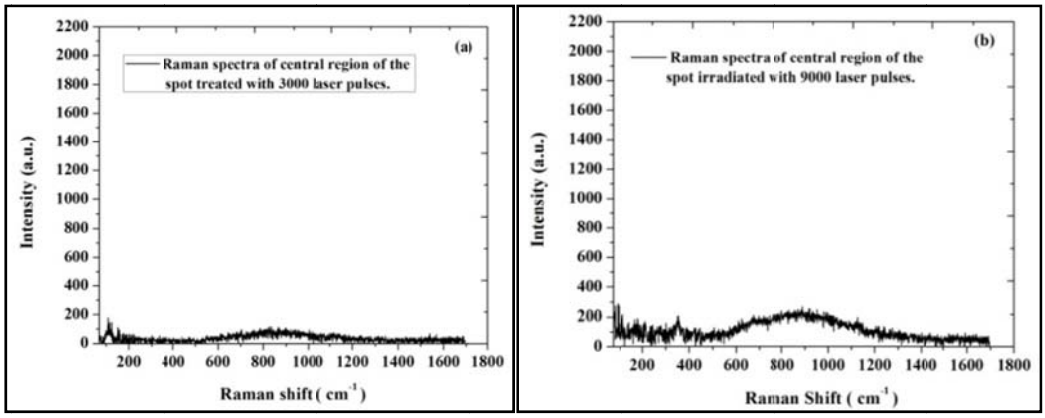

Figure 3.14 Raman spectra of central region of the spot irradiated with (a) 3000 laser pulses (5 min) (b) 9000 laser pulses (15 min) [92].

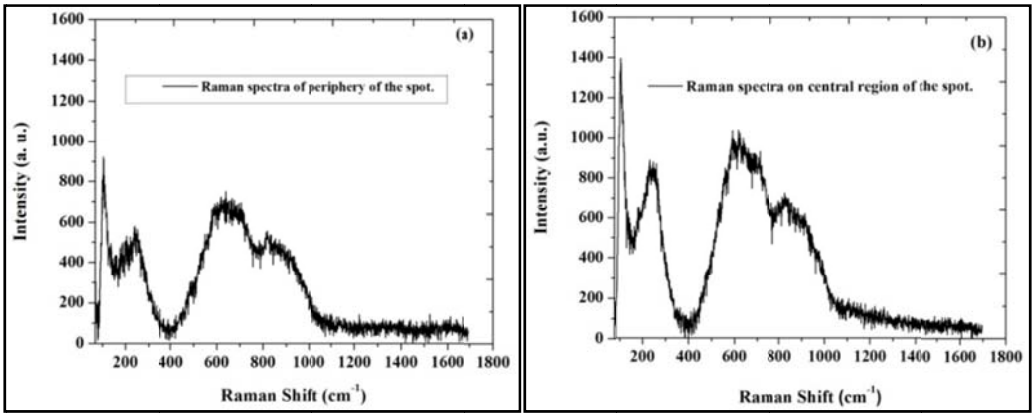

Figure 3.15 Raman spectra of different regions– (a) near periphery (b) near centre of the spot treated with laser fluence of 0.2 J/cm^2 [92].

3.3.2.3 Field emission characterization results

Fig. 3.16 shows variation of macroscopic field emission current density (J_m) versus applied macroscopic field (E_m) of the Ta specimens which were modified via irradiation using 3000, 6000 and 9000 laser pulses per spot.

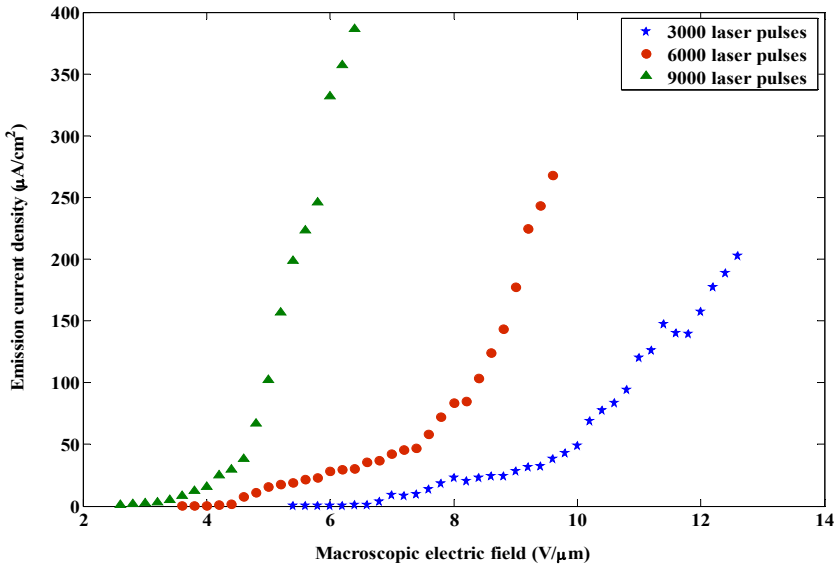

Figure 3.16 J_m vs E_m characteristics of the laser micro-structured Ta specimens [92].

Observed turn on field (E_{on}) defined as the field required to generate emission current equal to 10 μA/cm^2 for the specimens treated with 3000, 6000 and 9000 pulses per spot were measured to be ~6.6 V/μm, ~4.8 V/μm and ~3.7 V/μm, respectively. Also, achieved maximum emission current densities for these three samples were 200 μA/cm^2, 268 μA/cm^2 and 386 μA/cm^2 at macroscopic fields of 13 V/μm, 9.5 V/μm and 6 V/μm, respectively. Threshold macroscopic field (E_{th}) which is defined as the applied field required to generate J_m equal to 100 μA/cm^2 for these samples were found to be 10.9 V/μm, 8.3 V/μm and 5 V/μm, respectively. The observed decrease in turn on field with increasing number of incident laser pulses/spot could be due to an increase in aspect ratio and height of the generated micro-protrusions with increasing number of incident

laser pulses/spot. Since the region in laser treated spot where protrusions are formed has not shown signature of oxide formation work function of Ta has been used to estimate parameters characterizing these field emitters.

Fig. 3.17 shows Fowler-Nordheim (F-N) plot corresponding to FE data on $J_m$vs E_m. Estimated field enhancement factor and effective area of emission corresponding to the three samples are presented in Table 3.4.

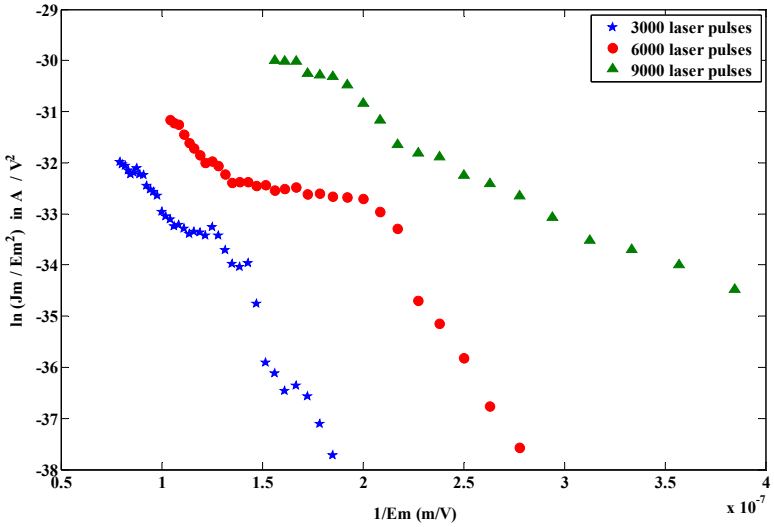

Figure 3.17 F-N plot of the FE experimental data.

Table 3.4 Estimated parameters characterizing laser micro-structured Ta samples as field emitters [92].

Sr. No.	Field emitter characterizing parameter	Sample # 1 (3000 pulses)	Sample # 2 (6000 pulses)	Sample # 3 (9000 pulses)
1.	Turn on field (E_{on}) [V/μm]	6.6	4.8	3.7
2.	Threshold field (E_{th}) [V/μm]	10.9	8.3	5
3.	Generalized slope correction factor (χ_m)	0.88	0.85	0.84
4.	Macroscopic field enhancement factor with slope correction (β_m)	978	1660	2543
5.	Macroscopic pre-exponential factor (λ_m) (formal area efficiency of emission)	3.87×10^{-14}	6.6×10^{-15}	8.5×10^{-15}

Stability of the emission current drawn from surface μ-structured specimens has also been tested here. Variation of field emission current with time corresponding to specimens treated using 3000, 6000 and 9000 laser pulses per spot are presented in Figs. 3.18 (a-c). It is observed from these tests that emission current from the specimen treated with 9000 laser pulses per spot dropped suddenly to half of its set value after 50 minutes of continuous operation and then continued to gradually decrease with time. In contrast, emission current was fairly stable for specimens treated with 3000 and 6000 laser pulses per spot [Fig. 3.18 (a & b)]. The observed sudden fall in emission current in case of sample #3 (Fig. 3.18c) could be due to damage of the protrusions which served as the predominantly electron emitting sites in this case.

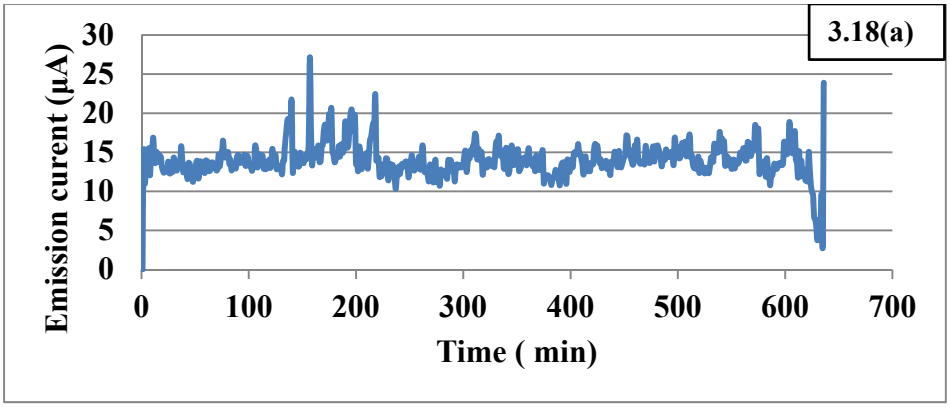

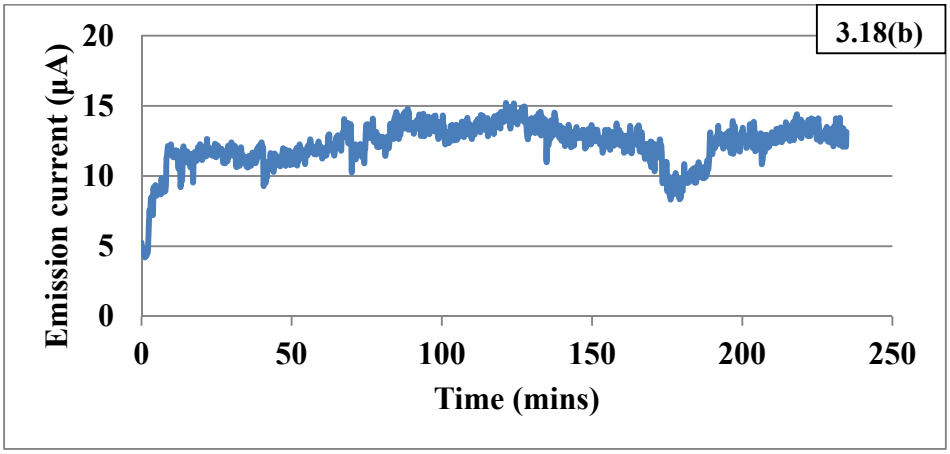

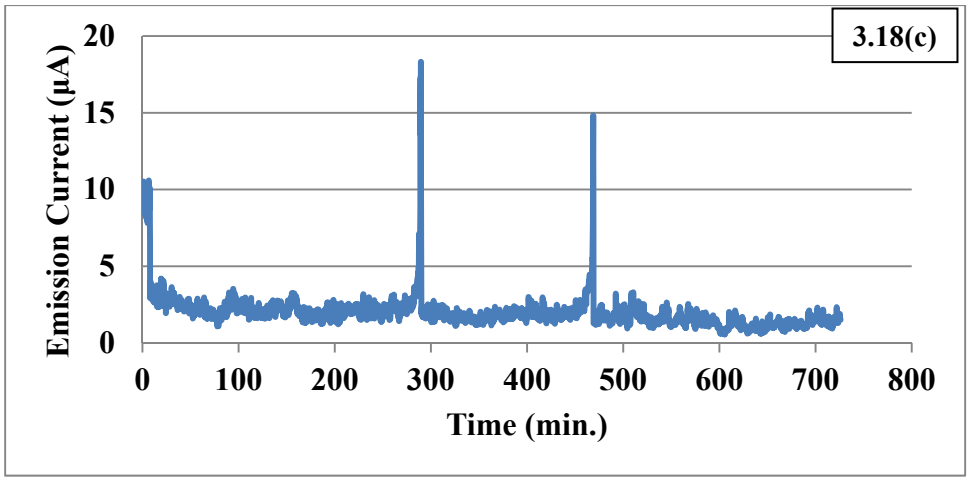

Figure 3.18 (a−c) Field emission current versus time for the Ta specimens treated with different number of laser pulses per spot (a) 3000 laser pulses (b) 6000 laser pulses (c) 9000 laser pulses [92].

3.4 Conclusion

Our results on surface micro-structuring of SS 304 targets have revealed that targets irradiated with laser fluence ≥ 4 J/cm^2 and 3000 pulses resulted in formation of deep crater within the laser irradiated spot. Micro-protrusions are formed on the laser irradiated surface when incident laser fluence is ≤ 2 J/cm^2. SS samples treated with 2 J/cm^2 and varying number of laser pulses per spot have shown increase in mean height of the grown surface micro-protrusions with increasing number of incident laser pulses. Initially growth of height of surface protrusions with incident number of pulses was rapid and it slow down after certain number of laser pulses. Target irradiated with 6000 laser pulses at laser fluence of 0.7 J/cm^{2}has shown generation of surface micro-protrusions in the entire region of the irradiated spot. Density and size of the formed surface features were varied with position within the spot. Towards periphery of the laser treated spot density of the generated surface micro-protrusions was ~4.5x10^7 protrusions/cm^2. SS surface micro-structured with 6000 pulses per spot at laser fluence 0.7 J/cm^2 has shown significant enhancement in field emission with measured E_{on} equal to ~7.5 V/µm and delivered

emission current density upto 340 μA/cm^2. Estimated macroscopic field enhancement factor (β_m) and formal for this specimen were 585 and ~2.7×10^{-10}, respectively. Field emission current from the laser micro-structured specimen was fairly stable over the test period.

Similarly, dense surface micro-protrusions were generated on Ta targets via nanosecond laser irradiation with laser fluence of 0.9 J/cm^2 and varying number of laser pulses in the range 3000 to 9000. Peak height of the generated surface micro-protrusions and mean roughness of the laser treated surface increased with increasing number of irradiating pulses. Raman spectroscopy results revealed that chemical phase of the laser treated region varied with position within the laser irradiated region. Central region of the laser irradiated spots where incident local laser fuence in high (micro-protrusions are formed) remained in metallic phase while periphery of the irradiated spot consists of Ta_2O_5. Laser treated Ta samples have shown enhanced field emission. Ta sample treated with 9000 laser pulses has shown lowest E_{on} (~3.7 V/μm) and delivered maximum emission current density (~386 μA/cm^2) among all the laser treated Ta samples. However, its field emission current stability was poor in comparison to other laser treated Ta samples.

Chapter 4

Femtosecond Laser Based Surface Micro-structuring of Stainless Steel 304 and Tantalum Targets for Field Emission Enhancement

4.1 Introduction

Femtosecond (fs) pulsed laser induced surface micro/nano structuring has been extensively employed in various applications owing to its offered advantages. Advantages of the fs lasers in material surface processing comes from two reasons, namely, high peak power and ultrashort duration of pulses [102]. Ultrashort duration of the laser pulse (< electron phonon thermalization time and heat diffusion times) causes lesser heat dissipation in bulk of the target resulting in reduced heat affected zone (HAZ). High peak power makes processing of optically transparent materials possible via multi-photon absorption. Since metals have high thermal conductivity fs lasers play a crucial role in precise surface modification of metals. Fs laser based surface micro-structuring is a highly non-equilibrium process hence formation of metastable phases on the target surfaces are possible.

There are many reports on fs laser induced generation of self-assembled micro-protrusions on the metals and semiconductors (some of them are listed in Sections 1.4 and 1.9). Only a few of them have reported field emission from fs laser micro-structured metals. In these reports laser micro-structured surfaces have shown good field emission properties.

In this chapter our results on fs laser induced surface micro-structuring of Stainless Steel 304 (SS 304) and Tantalum (Ta) surfaces and their characterization in terms of surface morphology, chemical phase and field emission behavior have been discussed.

4.2 Surface micro-structuring of SS 304 targets with laser fluence of 0.5 J/cm^2

4.2.1 Experimental details

To carry out surface micro-structuring and their characterization samples of commercially available SS 304 have been taken as targets. Typical dimensions of the used targets were– length: 1 cm, width: 1 cm and thickness: 0.05 cm. These targets were polished using emery paper of grit sizes 180 and 1/0. These polished samples were cleaned using ethanol before doing surface modification experiments. To generate self-assembled micro-protrusions on target surfaces these targets were directly irradiated by a focused beam of a femtosecond (fs) laser. Experimental setup used for surface micro-structuring has been explained in Chapter 2. Various sets of experiments for surface micro-structuring of SS 304 targets have been carried out by varying laser fluence and target scan speed in the range 0.3 J/cm^2 to 0.9 J/cm^2 and 25 μm/s to 1000 μm/s, respectively.

4.2.2 Characterization results

4.2.2.1 Surface morphology characterization results

In a first set of experiments SS 304 specimens were irradiated with varied number of laser pulses in the range 6 x 10^3 to 4.5 x 10^4corresponding to fixed laser fluence levels at 0.3J/cm^{2}and 0.5 J/cm^2 under static condition. Fig. 4.1 (a-d) shows scanning electron microscopy (SEM) images of the laser irradiated spots corresponding to laser fluence of 0.5 J/cm^2 and number of laser pulses equal to 6 x 10^3, 1.5 x 10^4, 3.0 x 10^4 and 4.5 x 10^4, respectively. From these figures it is observed that micro-granular structures are formed within the laser irradiated region with dimensions of these micro-protrusions varying from centre of the spot to the periphery. Also, size and depth of undulations on the surface increased with increasing number of incident laser pulses.

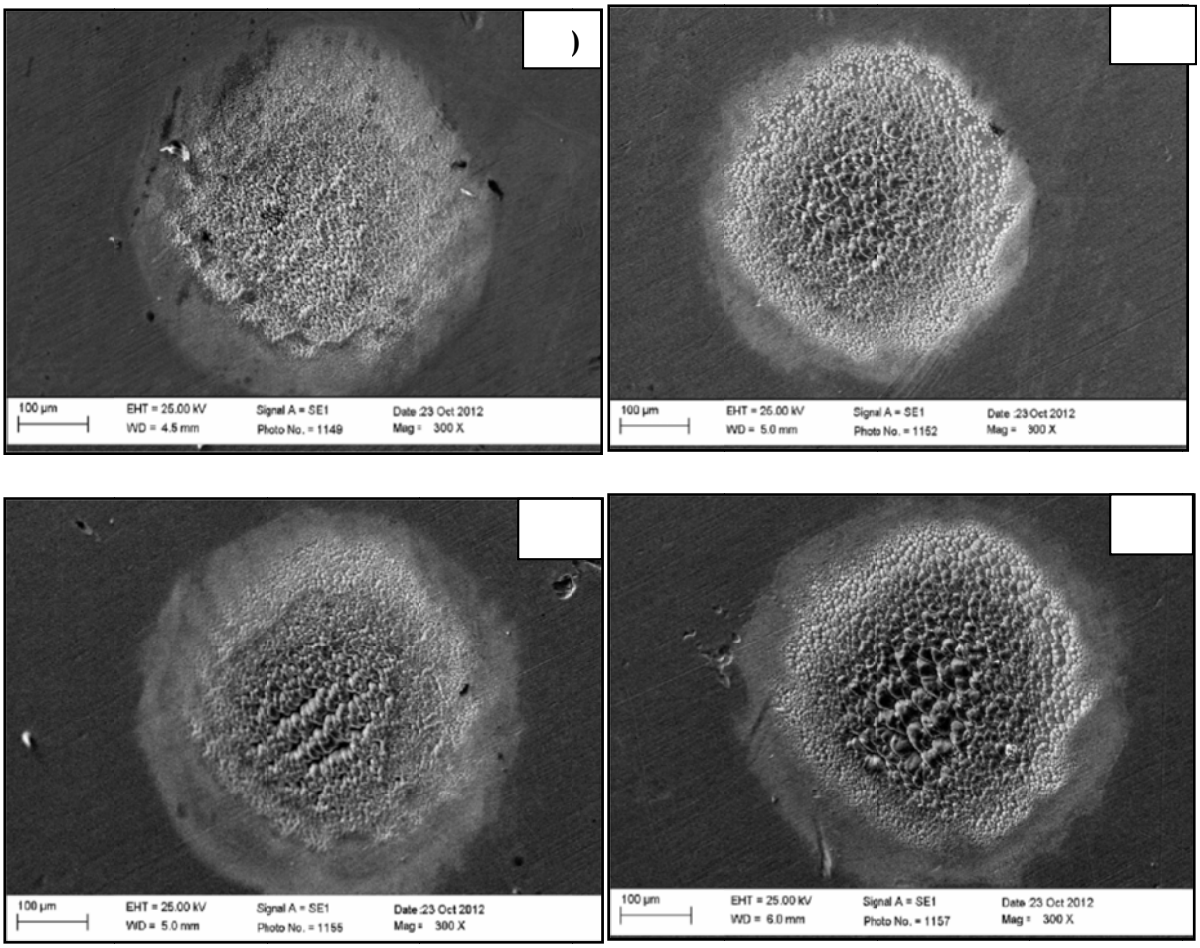

Figure 4.1 SEM images of the laser treated spots on SS samples corresponding to laser fluence of 0.5 J/cm^2 and number of incident pulses equal to (a) 6 x 10^3 (b) 1.5 x 10^4 (c) 3.0 x 10^4 and (d) 4.5 x 10^4 [12].

Formation of these micro-structures has been explained on the basis of hydrodynamic instability of the laser generated molten surface due to thermo-capillary forces [103, 104]. Mechanism for formation of surface micro-structures has been described in Chapter 3. According to the reports growth rate and period of the generated surface features increase with increasing melt pool thickness and decreasing temperature gradient. Therefore, the observed variations in the dimensions of the surface features from centre of the spot to the periphery could be due to the spatial profile of the incident laser beam. As spatial profile of the incident laser beam is Gaussian

in nature there will be a spatial variation in the energy deposited to the target. Gaussian spatial profile of the incident laser beam leads to decrease in deposited energy from centre of the spot to the periphery resulting in maximum melt depth and lowest temperature gradient at the centre of the irradiated spot. Hence, it expected to get large size micro-structures towards centre of the laser irradiated spot. Observed increase in depth of modulation of the surface with increasing number of irradiating laser pulses could be due to the cumulative effect of growth of features with each incident pulse.

To generate uniform micro-protrusions over large surface area we need to deposit uniform amount of energy over the surface. Therefore, surface micro-structuring of SS 304 targets was carried out over large area (5 mm x 2.7 mm) by scanning the target in the plane perpendicular to the incident laser beam. Fig. 4.2 (a-f) shows SEM images at different magnification of the SS target treated with laser fluence of 0.5 J/cm^2 and target scan speed of 200 μm/s. During this experiment separation between two consecutive line scans was fixed at 100 μm. Laser beam spot diameter on the target was ~450 μm. Therefore, the chosen target scanning speed and separation between two consecutive line scans corresponded to effectively ~3.1 x 10^4 laser pulses at every position in the irradiated region. It is observed from the images in Fig 4.2 (a−f) that laser irradiation along with target scanning has resulted in formation of high density micro-protrusions on the SS surface. Estimated typical tip diameter and number density of the generated micro-protrusions were in the range 2 to 5 μm and ~5.6 x 10^5 micro-protrusions/cm^2, respectively. Height of some the micro-protrusions were up to ~50 μm. High magnification images of the laser treated area [Figs 4.2(e–f)] have revealed that each of the generated micro-protrusion is covered with sub-micron size features (typical size ~ 200−300 nm) [12].

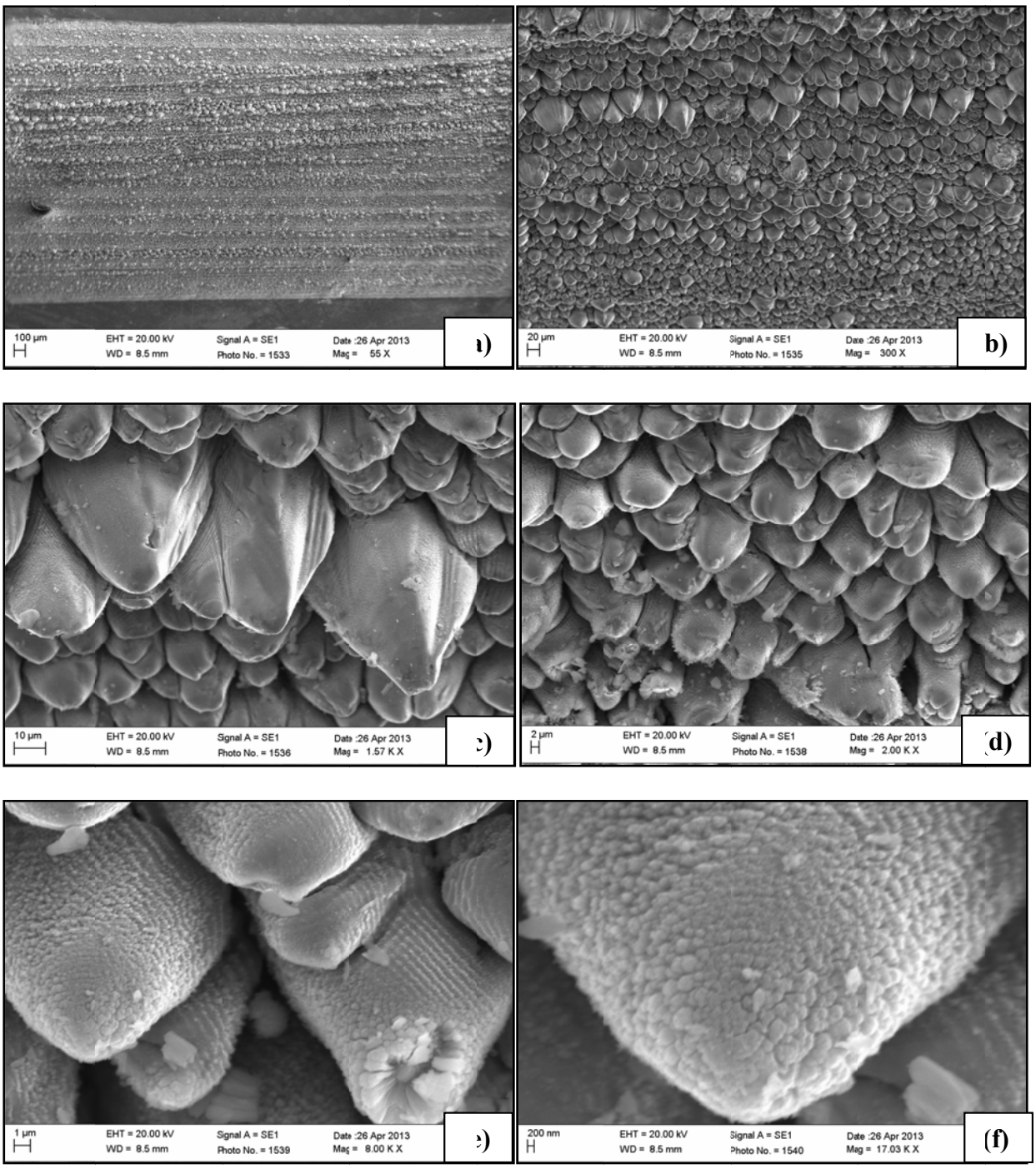

Figure 4.2 SEM images at different magnifications of the SS specimen treated at laser fluence of 0.5 J/cm^2 and target scan speed of 200 µm/s with 100 µm separation between consecutive line scans [12].

Observed high density and large size of micro-protrusions on the laser irradiated surface is expected to show local field enhancement on this surface resulting in enhanced emission current at low applied electric field. Since the SS specimen was irradiated with laser under atmospheric ambience formation of iron oxides and nitrides were expected on the laser treated region. Work function of iron oxides and nitrides are significantly different from SS work function. Therefore, before field emission characterization this sample was characterized for formed chemical and crystalline phases using GIXRD technique. Also, its work function was measured using Kelvin probe microscopy.

4.2.2.2 Grazing incidence X-ray diffraction (GI-XRD) results

GI-XRD of the samples was recorded at 5^{o} angle of incidence of the X-ray beam with respect to sample surface. GI-XRD of the untreated and laser micro-structured specimens are shown in Figs. 4.3 (a & b), respectively.

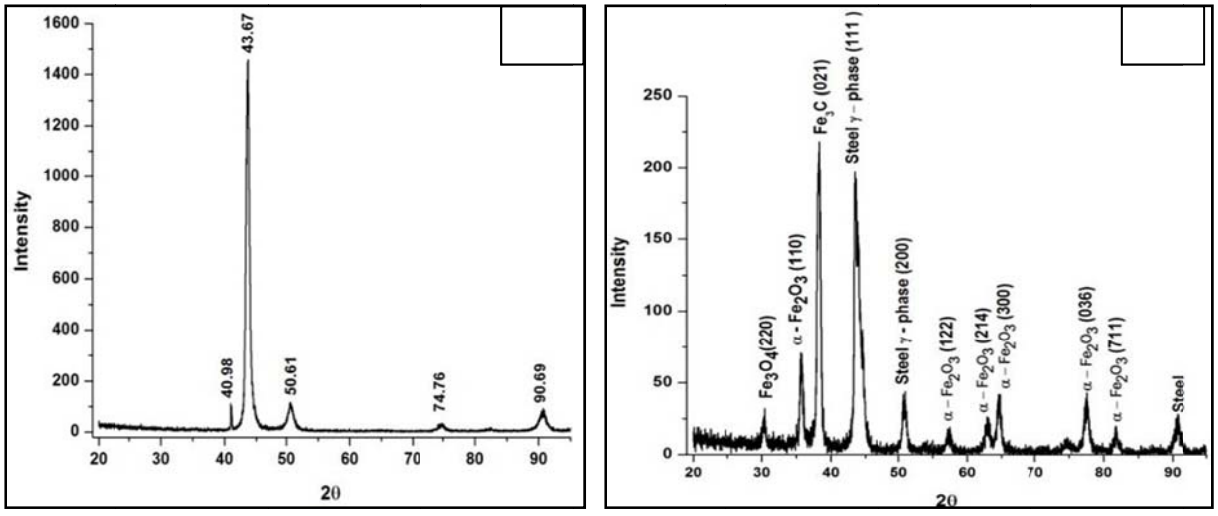

Figure 4.3 GI-XRD pattern of (a) untreated SS 304 (b) laser treated SS 304 sample [12].

GI-XRD pattern of untreated SS specimen has shown diffraction peaks corresponding only to SS 304 indicating absence of oxide or nitride on the surface. This was expected as untreated

specimen was polished with emery paper and cleaned before carrying out GI-XRD analysis. Diffraction peaks in GI-XRD pattern of the laser micro-structured surface occurs at 2θ values 30.4^{o}, 35.6^{o}, 38.3^{o}, 43.6^{o}, 44.5^{o}, 50.8^{o}, 57.2^{o}, 62.9^{o}, 64.6^{o}, 74.8^{o}, 77.4^{o}, 81.7^{o}, 90.6^{o} corresponding to Fe_3O_4 (220), α-Fe_2O_3 (110), Fe_3C (021), SS γ-phase (111), SS α-phase (111), SS γ-phase (200), α-Fe_2O_3 (122), α-Fe_2O_3 (214), α-Fe_2O_3 (300), SS γ-phase (220), α-Fe_2O_3 (036), α-Fe_2O_3 (711) and SS γ-phase (311), respectively (Fig. 4.3 (b)) [105−107]. This indicates formation of iron oxides (Fe_2O_3/Fe_3O_4) and iron cementite (Fe_3C) phase upon laser treatment. Though SS samples were irradiated with laser pulses in atmospheric air, which contains mostly nitrogen no signature of iron nitrides was found in the GI-XRD pattern of the laser modified surface. Absence of iron nitrides in the laser treated surface can be explained on basis of the fact that iron nitrides are thermodynamically unstable compared to Fe and N_2 at high temperatures. Therefore, iron nitrides decompose into Fe and N_2 at high temperature. Formed N_2 gas escapes from the surface via degassing process [108]. Ref. [108] has reported that at temperatures >973 K nitride completely disappears from the surface and iron oxides are predominantly formed on heated SS surface. During laser surface micro-structuring process surface temperature goes beyond melting point of the steel (~1450 ^{o}C). Therefore, our observation on absence of iron nitride on laser treated surface is in agreement with reported observations. Other observation is absence of chromium oxide in the laser treated region even though SS 304 contains ~18 % Cr and formation of Cr_2O_3 is thermodynamically preferred. The observed predominance of iron oxides upon laser irradiation can be explained on the basis of oxidation mechanism proposed in [106, 109]. According to the proposed mechanism first of all a thin film of Cr_2O_3 is formed on SS surface upon laser irradiation. Formed Cr_2O_3 film on the surface prevents further oxidation of Cr atoms present in the bulk due to poor mobility of Cr^{3+} ions through Cr_2O_3 film. Poor mobility

of the Cr^{3+} does not allow Cr^{3+} ions to reach on surface to react with oxygen atoms. However, Fe^{3+} ion has higher mobility in comparison to other constituents of SS 304 through grown Cr_2O_3 film. Therefore Fe^{3+} ions can easily diffuse from the bulk of the target through the Cr_2O_3 film and reach the surface. On the surface Fe^{3+} ions react with atmospheric oxygen to form iron oxides. Hence, grown oxide layer on SS surface upon laser treatment is predominantly consisting of iron oxides.

The observed cementite phase (Fe_3C) phase in the laser treated surface can be explained on the basis of incorporation of excess number of carbon (C) atoms in the melt pool during heating of the target [110]. During heating of the target when melt pool temperature is high large number of C atoms can diffuse from the bulk of the target towards the melt pool induced by irradiation with large number of laser pulses (~3.2 $x10^4$ pulses/location) due to increased solubility of C in SS at high temperature. Once the concentration of C atoms in the laser heated zone reaches beyond a certain level and solubility of C in SS reduces during the cooling process Fe_3C phase precipitates. In the laser irradiated region Fe_3C phase is formed instead of Fe and C mixture because Fe_3C is more stable than Fe and C mixture at temperature >1000 ^oC [111]. Also, amongst all iron carbide phases Fe_3C phase is the most thermodynamically stable phase. Therefore, on heating of SS with large number of laser pulses Fe_3C phase is predominantly formed.

4.2.2.3 Work function measurement

GI-XRD analysis of the laser micro-structured SS sample reveals formation of iron oxide and carbide. This indicated that work function (φ) of the laser modified surface will be higher than stainless steel (~4.5 eV) because φ of Fe_2O_3, Fe_3O_4 and Fe_3C are 5.7-5.4 eV [112], 5.2 eV [113] and 5.83 eV [114], respectively. Therefore, work function distribution over a surface area of 2

mm x 2 mm on the SS 304 specimen modified with laser fluence of 0.5 J/cm^2 and 200 µm/s sample scanning speed was measured via Kelvin probe microscopy. Result on work function distribution is shown on Fig. 4.4. Average value of φ over the measured area is found to be 5.13 eV which is lower than the work functions of the iron oxides and carbides constituting the surface. There are reports indicating that generation of surface micro/nano protrusions [115] and increase in number density of defects in target surface [116, 117] results in lowering of φ value of the material. In the present case also, surface micro/nano protrusions are generated on the surface. Also, it is expected that laser treated surface may contain large number density of defects due to rapid heating and cooling involved in the laser induced surface modification process. Hence, above mentioned processes could be some of reasons responsible for the measured lower φ value of surface in comparison to φ's of its constituent phases.

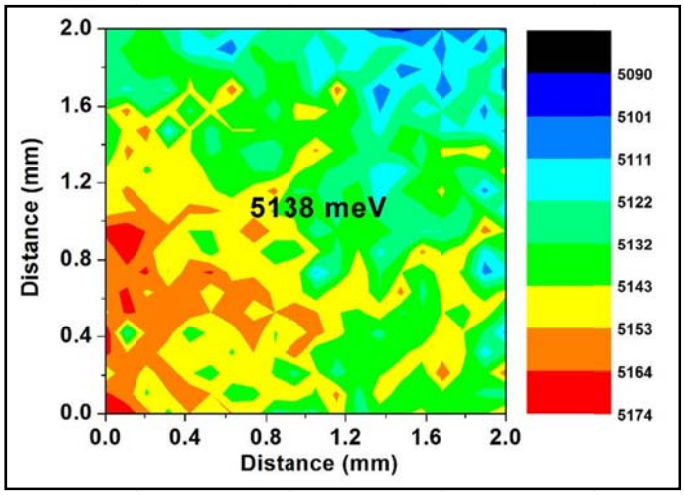

Figure 4.4 Work function distribution of the SS 304 specimen laser micro-structured with laser fluence of 0.5 J/cm^2 and target scan speed of 200 µm/s [12].

4.2.2.4 Field emission characterization results

Field emission (FE) characterization results on SS specimen the laser micro-structured with laser fluence of 0.5 J/cm^2 and target scan speed of 200 µm/s are shown in Fig. 4.5 to Fig. 4.8.

Variation of macroscopic field emission current density (J_m) with applied electric field (E_m) i.e. J_m-E_m characteristic is shown in Fig. 4.5. Here, E_m is defined as the applied voltage divided by distance between cathode and anode surfaces and J_m is defined as the emission current divided by total area of surface micro-structured region of the sample. To estimate emission current density only laser micro-structured area has been taken in to account because untreated SS sample did not deliver measurable emission current for applied electric field equal to 11.4 V/µm. J_m-E_m characteristics shows that turn on field (E_{on}) (defined as the E_m to produce J_m equal to 10 µA/cm^2) is ~4.1 V/µm. Also, this specimen delivered high J_m up to 2.5 mA/cm^{2}at E_m equal to 7.6 V/µm. Enhanced field emission of the fs laser micro-structured SS sample could be due to local field enhancement on tips of the generated micro-protrusions.

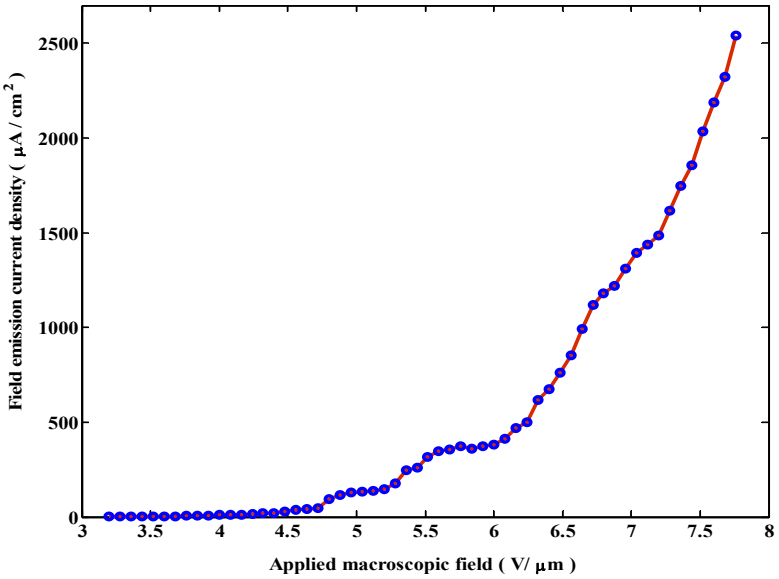

Figure 4.5 J_m vs E_m characteristics of SS specimen micro-structured with laser fluence of 0.5 J/cm^2 and target scan speed of 200µm/s [12].

The observed E_{on} for this specimen is significantly lower and maximum delivered J_m is multifold higher in comparison to the respective values for SS 304 sample treated with nanosecond laser (reported in Chapter 3). This could be due to higher number density and larger height of the

generated surface micro-protrusions on femtosecond treated SS sample in comparison to SS sample treated with nanosecond laser.

Fig. 4.6 shows typical photograph of the fluorescence produced on anode due to striking field emission electrons for a typical applied field of 6.2 V/μm.

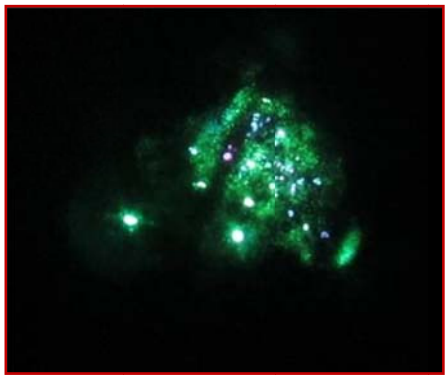

Figure 4.6 Typical photograph of fluorescent spot on anode due to striking field emission electrons corresponding to E_m= 6.2 V/μm [12].

Fig. 4.7 shows FN plot of the experimental data on J_m–E_m characteristics and its linear plot. FN plot of the experimental data on FE characterization shows broadly linear trend with some fluctuations in the measured data points.

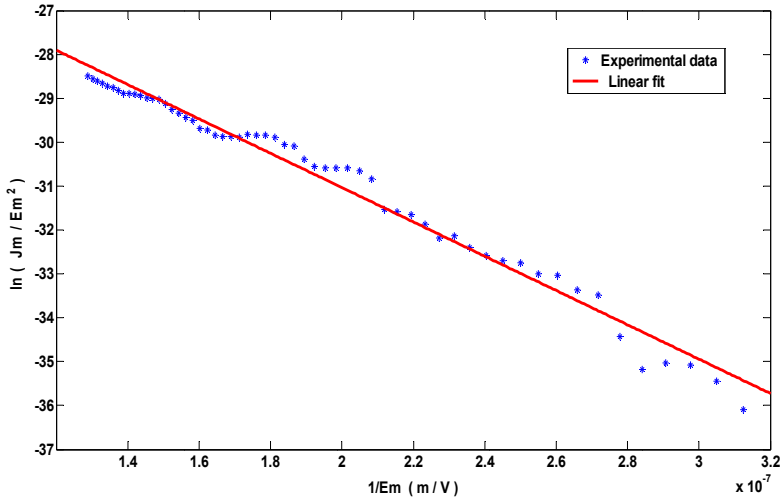

Figure 4.7 F-N plot of the experimental data of field emission characterization and its linear fit [12].

Some of the important parameters for laser modified SS sample characterizing its behavior as a large area field emitter (LAFE) have been estimated using the same methodology as used in Chapter 3. Estimated Field emitter characterizing parameters for fs laser micro-structured SS sample are summarized in Table 4.1. Estimated slope of the FN plot (S) was found to be -3.9 x 10^{-7} Np.mV^{-1}. Macroscopic field enhancement factor (β_m) modified with slope correction factor was estimated to be ~1830 with value of slope correction factor (χ_m) equal to 0.9. This value of β_m is much higher than the field enhancement factor values (~40) reported for a stainless steel surface with 0.1 μm average surface roughness [99] and β_m= 585 measured for SS sample modified with nanosecond pulsed laser reported in chapter 3 and ref. [118]. The value of pre-exponential factor (λ_m) which is also a provisional estimate for formal area efficiency of emission was estimated to be ~2.1 x 10^{-12}. This implies that very small fraction of the total surface area (~2.1 x 10^{-12}) is actually emitting electrons for this sample. Some of the reported field emission results on field emission from Fe_2O_3 with different surface morphologies are presented in Table 4.2.

Table 4.1 List of estimated parameters characterizing of laser treated SS 304 as field emitter [12].

Sr. No.	**Parameters**	**Value**
1.	Turn on field (defined for 10 μA/cm^2 current density)	4.1 V/μm
2.	Threshold field (F_{th}) (defined for 100 μA/cm^2 current density)	4.8 V/μm
3.	Slope of the F-N plot (*S*)	-3.9×10^7 Np.mV^{-1}
4.	Macroscopic field enhancement factor (β_m)	1830
5.	Generalized slope correction factor (χ_m)	0.9
6.	Macroscopic pre exponential correction factor (λ_m)	2.1×10^{-12}

Table 4.2Some of the reported values of E_{on} and β_m for different nanostructures of Fe_2O_3.

Micro/nano Structure	**Preparation Method**	**E_{on} (V/µm)**	**β_m**	**Reference**
Nanowire	Thermal oxidation	3.3-4.7	1023 - 1754	Nanoscale Res. Lett. (2008) 3:330-337 [119]
Nanoneedles	Themal oxidation	4.8	-	J. of Alloys & Compounds 478 (2009) 38-40. [120]
Nanoflakes	Thermal oxidation	7.6-5.2	-	Appl. Surf. Sci., 292 2014, 454-461. [121]
3D Urchin	Thermal oxidation	2.8	4313	ACS Appl. Mater. Interfaces, 2011, 3, 3084-3090 [122]
Quasi aligned 1 D nanoneedles	Thermal oxidation	1.7	-	J. Phys. Chem. C 2011, 115, 8816-8824. [123]
Micro-protrusions	Nanosecond pulsed laser irradiation	7.5	585	[118]
Hierarchical micro/nano protrusions	fs pulsed laser irradiation	4.1	1830	Present work

Experimentally observed turn on field and field enhancement factor in this study compares well with the turn on fields and field enhancement factors for the reported morphologies indicating that laser treated surfaces can serve as good large area field emitters.

For any technological application of the field emitter stability of the emission current is a very important parameter. Therefore, SS sample treated with 0.5 J/cm^2 laser fluence at target scan speed of 200 μm/s was characterized for field emission current stability. Emission current stability was tested via continuous operation over a period of ~ 16 hrs at a preset current value of ~4.5 μA. Variation of emission current with time is shown in Fig. 4.8. This figure shows that emission current was stable during the test period with standard deviation of emission current variations about mean value to be only ~ 0.22 μA (~ 4.9 %).

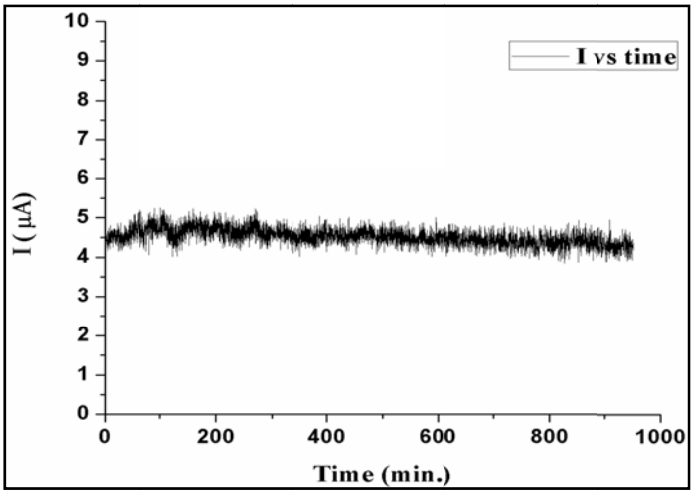

Figure 4.8 Field emission current vs time for the SS 304 sample micro-structured with laser fluence of 0.5 J/cm^2 and scan speed of 200 μm/s (separation between lines ~ 100 μm) [12].

4.3 Surface micro-structuring of SS 304 sample with laser fluence of 0.9 J/cm^2

4.3.1 Experimental details

For all practical applications surface micro-structuring has to be maximized. Therefore, in order to generate surface micro-protrusions on the SS 304 surface with lesser number of incident laser pulses another set of experiments were planned with higher incident laser fluence. In this set of

surface micro-structuring experiments laser fluence was increased to 0.9 J/cm^2 and SS 304 target was irradiated with varying scan speed in the range of 25 µm/s to 1000 µm/s.

4.3.2 Surface morphology characterization results

Fig. 4.9 shows a typical SEM image of SS surface treated with fs laser at target scan speeds in the range 25–400 µm/s. SEM imaging of the SS surfaces treated with laser fluence of 0.9 J/cm^2 revealed that deep crater was formed on the surface for target scan speed upto 100 µm/s. This occurs due to the fact that laser fluence used in this experiment is much higher than ablation threshold fluence for stainless steel (~0.13 J/cm^2) [124]. Slower target scan speed implies longer residence time for laser beam at a particular location resulting in irradiation with more number of laser pulses. Irradiation of the surface with more number of laser pulses leads to more removal of mass from the surface resulting in formation of trench like structure on the surface.

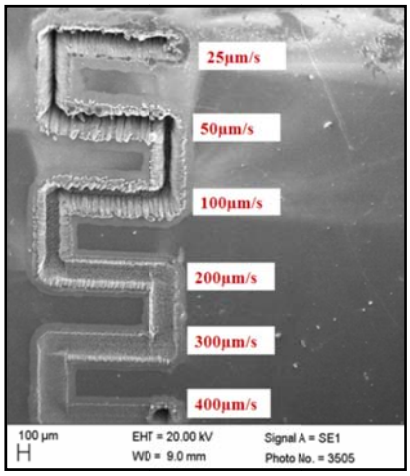

Figure 4.9 SEM image showing morphology of the target surface treated with laser fluence of 0.9 J/cm^2 at different scan speeds [125].

Magnified SEM image of the target surface irradiated at scan speeds 200 µm/s and above revealed formation of high density surface micro-protrusions. Typical SEM images corresponding to SS surfaces treated at target scan speed of 200 µm/s, 400 µm/s, 500 µm/s, 700

μm/s and 1000 μm/s are shown in Fig. 4.10 (a−e). Here again formation of surface micro-protrusions upon laser treatment can be explained on the basis of hydrodynamic instability of the laser generated melt pool as explained in the pervious chapter. Processing of the SEM image using Leica Qwin3 software revealed that number density of the generated micro-protrusions is ~10^6 micro-protusions/cm^2 in this case. Also, number density and mean height of these micro-protrusions showed an increasing and decreasing trends, respectively with increasing target scan speed.Variation of number density and mean height of the generated surface micro-protrusions with sample scan speed are shown in Fig. 4.11 and Fig. 4.12, respectively.

It is observed from SEM images in Fig. 4.10 (a−e) that in the region irradiated with fs laser pulses corresponding to target scan speed of ~400 μm/s surface grown μ-protrusions are of reasonable height and no debris is formed at the edges of the line scan. Hence, to generate uniform surface micro-protrusions over a large area for field emission study we selected a target scan speed of 400 μm/s and an area of 1 cm x 1 cm was treated at a typical laser fluence of 0.9 J/cm^2. During this experiment laser beam spot diameter on the target was ~300μm and separation between cosecutive line scans was fixed at 220 μm.

A typical SEM image of the SS sample surface micro-structured over an area of 1 cm^2 using laser fluence of 0.9 J/cm^2at target scan speed of 400 μm/s is shown in Fig. 4.13. This figure shows that high density uniform μ-protrusions are formed in the laser treated area except some lines where shallow crater has formed due to overlap of two consecutive line scans. Crater formation in the overlap region is due to irradiation of this region with more number of laser pulses (two times the number of pulses in comparison to other region) causing more removal of material resulting in crater formation. Since overlapped region is near the periphery of the laser beam where laser intensity is lower than central region fromed portion crater is shallow.

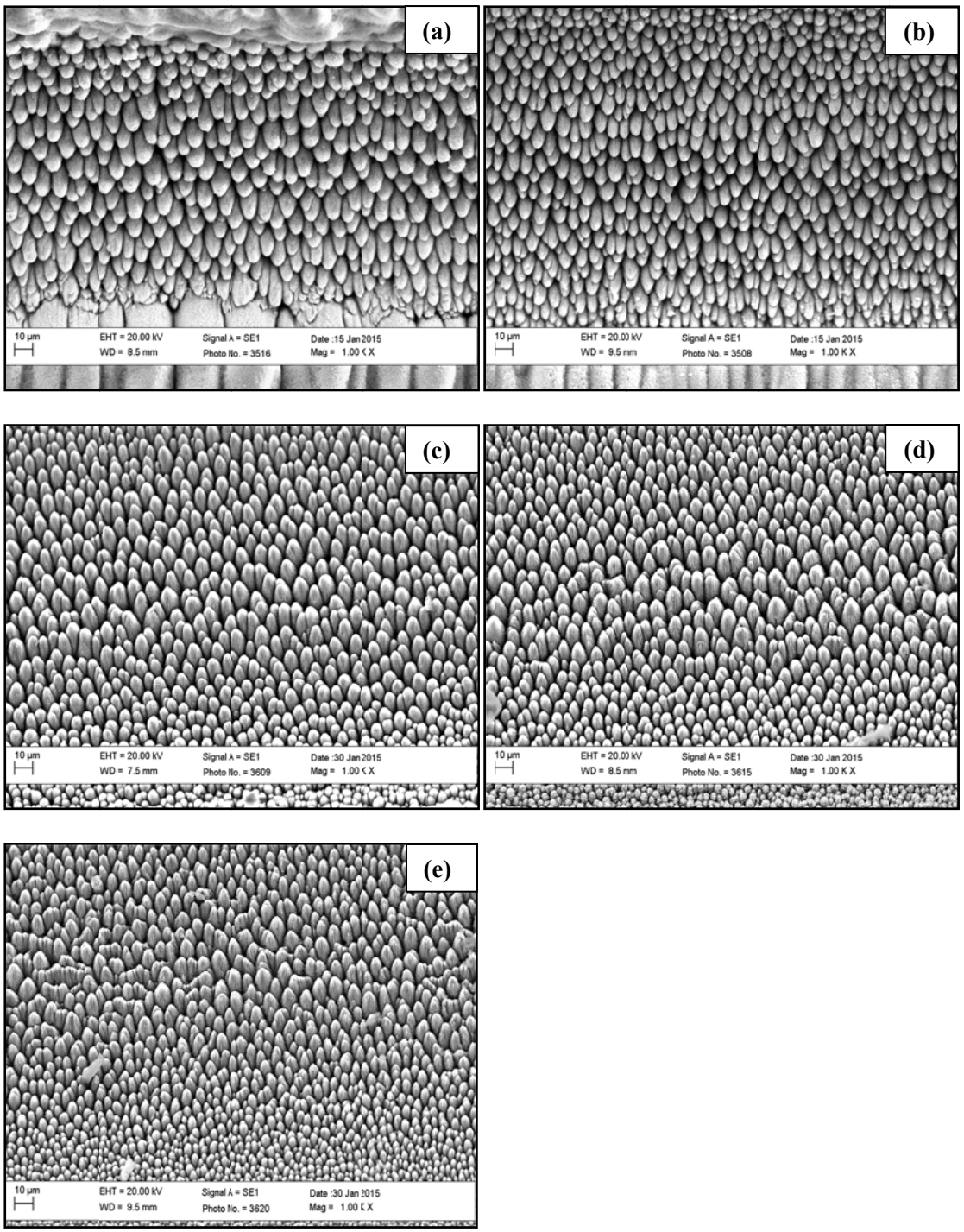

Figure 4.10 SEM images of the surfaces irradiated with laser fluence of 0.9 J/cm^2 and target scan speeds of (a) 200 µm/s (b) 400 µm/s (c) 500 µm/s (d) 700 µm/s and (e) 1000 µm/s [125].

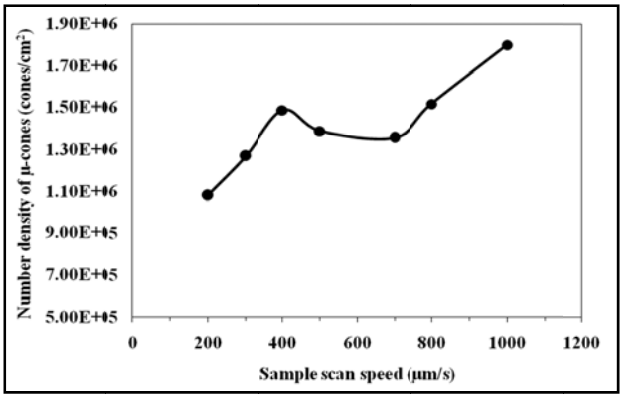

Figure 4.11 Variation of number density of generated µ-protrusions with target scan speed corresponding to incident laser fluence of 0.9 J/cm^2 [125].

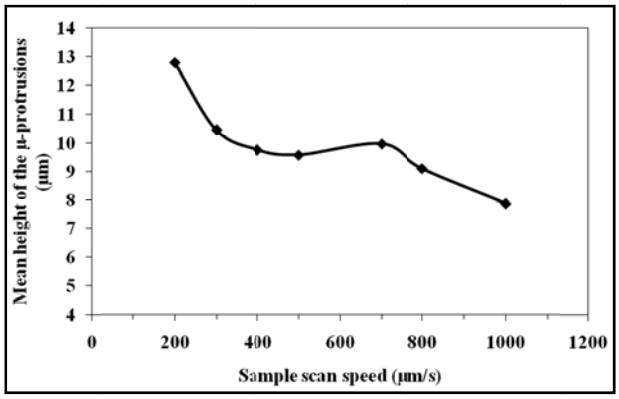

Figure 4.12 Variation of mean height of the generated surface µ-protrusions with target scan speed corresponding to incident laser fluence of 0.9 J/cm^2 [125].

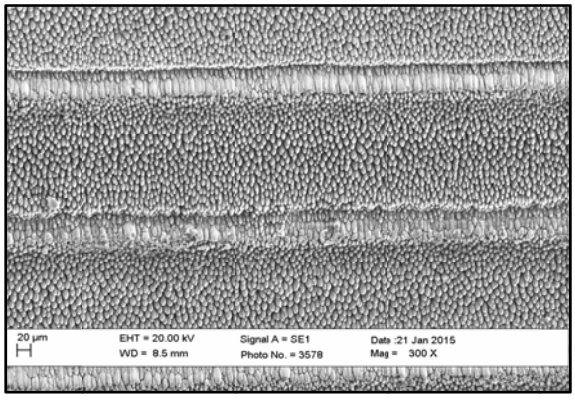

Figure 4.13 Typical SEM image of the SS 304 specimen surface treated over an area of 1 cm x 1 cm with laser fluence of 0.9 J/cm^2 and target scan speed of 400µm/s.

4.3.3 Field emission characterization results

J_m–E_m characteristics of the SS 304 surface micro-structured over an area of 1 cm^2 with laser fluence of 0.9 J/cm^2 and target scan speed of 400 µm/s is shown in Fig. 4.14. J_m–E_m characteristics of this sample shows poor field emission performance with delivering only 0.7 $\mu A/cm^2$ emission current density at applied electric field of 6.1 V/µm. The observed poor field emission current for this sample may due to field screening effect caused by high density of micro-protrusions.

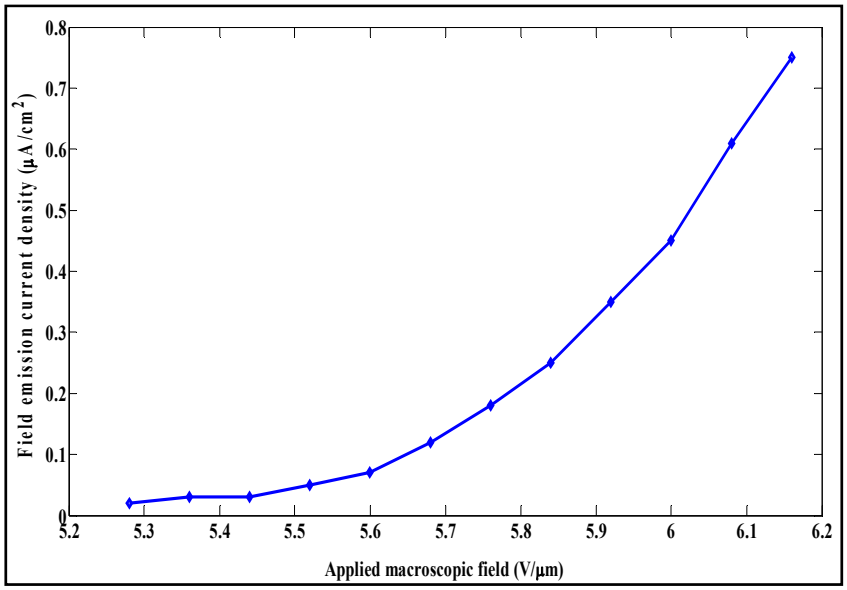

Figure 4.14 J_m-E_m characteristics of the SS sample treated with laser fluence of 0.9 J/cm^2 at target scan speed of 400 µm/s.

4.4 Surface micro-structuring of Tantalum targets

4.4.1 Experimental details

In this study targets used for surface micro-structuring were samples of commercially available high purity (99.9 %) tantalum foils (thickness ~100 µm). Typical dimensions of the targets were 8 mm x 7 mm. Each target was mechanically polished using emery papers and cleaned using

ethanol. Experimental setup used for surface modification of Ta samples was same as setup used for surface treatment of SS 304 targets. However, laser power, laser beam spot size on the target and target scanning speed were different from SS 304 surface modification experiments. In these experiments laser power incident on target surface was ~1.3 W which was focused on target using a convex lens of focal length 20 cm. During the experiments different Ta samples were micro-structured by varying space averaged laser fluence in the range 0.35 J/cm^2 to 0.55 J/cm^2. Laser fluence on the target surface was varied by changing distance between the focusing lens and the target surface using a translational stage with a linear drive. To prepare large area surface micro-structured samples for field emission characterization laser fluence was fixed at a particular value and target was irradiated and simultaneously scanned in XY plane (plane perpendicular to incident laser beam). Scanning speed during these experiments was kept constant at 25 μm/s and separation between two consecutive line scans was fixed at 75 μm. Total surface micro-structured area for each of the sample used for FE characterization was ~0.4 cm^2.

4.4.2 Characterization results

4.4.2.1 Surface morphology characterization results

Typical morphology of the Ta samples treated with laser fluence of 0.35 J/cm^2, 0.45 J/cm^2 and 0.55 J/cm^2 are shown in Figs. 4.15a, b and c, respectively. These figures show formation of high density surface micro-protrusions in the laser treated region. Further, high magnification SEM images of the samples treated with laser fluence levels 0.35 J/cm^2 and 0.45 J/cm^2 revealed that grown micro-protrusions were covered with submicron size features [Fig. 4.16 (a, b)]. Number densities of the generated micro-protrusions on different laser treated surfaces were estimated by analyzing corresponding SEM images using Leica Qwin3 software. Estimated number density of the generated micro-protrusions on Ta surfaces corresponding to irradiation with laser fluence of

0.35 J/cm^2, 0.45 J/cm^2 and 0.55 J/cm^2 are ~8.8 x 10^5, ~7.5 x 10^5 and ~3.5 x 10^5 micro-protrusions/cm^2, respectively. This observation indicates broadly a decreasing trend of number density of μ-protrusions with increasing incident laser fluence. Also, it is visible from these SEM images that generated surface micro-protrusions are tallest corresponding to Ta sample treated with laser fluence of 0.55 J/cm^2 [126].

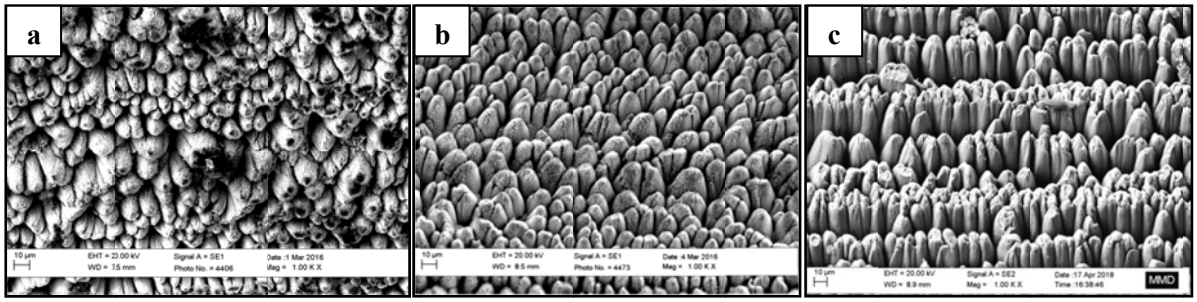

Figure 4.15 SEM images of the Ta surfaces micro-structured with laser fluence of (a) 0.35 J/cm^2 (b) 0.45 J/cm^2 (c) 0.55 J/cm^2 [126].

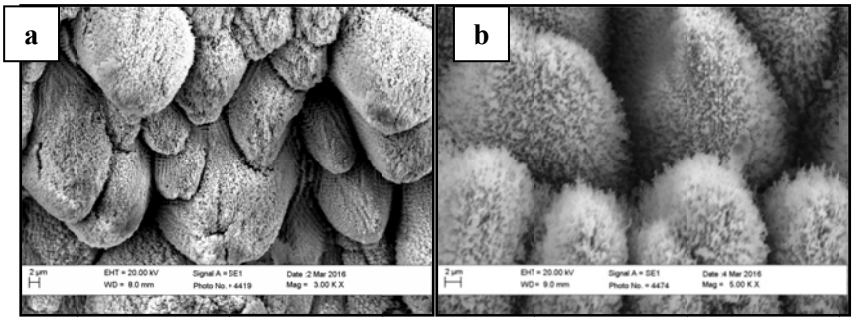

Figure 4.16 High magnification images of the Ta surfaces treated with 0.35 J/cm^2 and (b) 0.45 J/cm^2 [126].

To investigate effect of laser surface micro-structuring on field emission property of the laser modified Ta surface. Ta samples were micro-structured over an area of 0.4 cm^2 (8 mm x 5 mm) using incident laser fluence levels of 0.35 J/cm^2, 0.45 J/cm^2 and 0.55 J/cm^2, respectively. Typical SEM image of the Ta specimen treated with 0.55 J/cm^2 which has been used for field emission

characterization is shown in Fig. 4.17. This image is also showing formation of high density uniform surface micro-protrusions in the entire laser treated region.

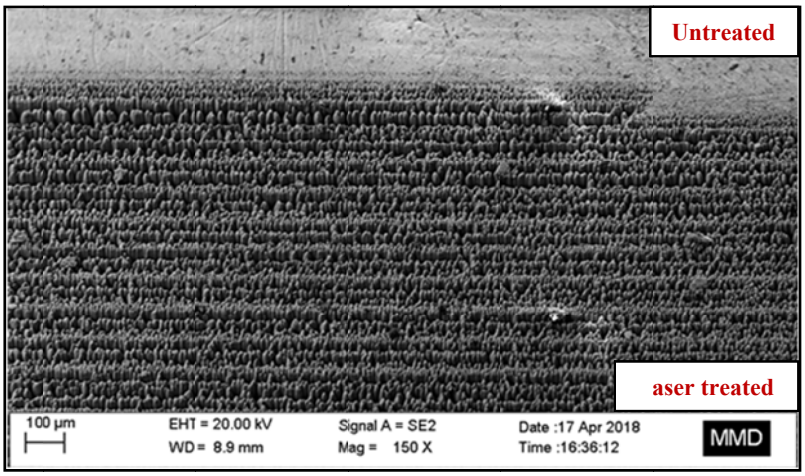

Figure 4.17 Typical SEM image of the Ta sample showing surfaces of untreated and laser treated regions [126].

4.4.2.2 GI-XRD characterization results

In order to investigate effect of laser treatment on chemical phase and crystalline phase of the surface, Ta specimen prepared for field emission and untreated Ta samples were characterized by GI-XRD and X-ray photoelectron spectroscopy (XPS) techniques.

GI-XRD pattern of the untreated and laser modified Ta specimens are shown in Fig. 4.18. Pristine Ta surface has shown X-ray diffraction peaks only at 2θ values 38.5°, 55.8°, and 69.8° corresponding to (1 1 0), (2 0 0) and (2 1 1) crystallographic planes of Ta, respectively indicating absence of Ta oxides and nitrides on the pristine surface. However, laser treated Ta surface has shown X-Ray diffraction peaks at 2θ values corresponding to Ta metal, as well as, at 2θ values equal to 22.9°, 28.4°, 36.8°, 46.9°, 50.5°, 58.7° and 64° which correspond to (0 0 1), (1 1 0), (1 1 1), (0 0 2), (0 2 0), (2 2 0) and (2 22 0) planes of Ta_2O_5 [127, 128]. Although, laser treatment has been carried out in air no X-ray diffraction peaks corresponding to tantalum nitride is observed.

Therefore, GI-XRD analysis revealed the laser treated surface mainly consists of crystalline Ta_2O_5. This has also been confirmed by XPS analysis of the laser treated sample. Crystalline phase of the Ta_2O_5 has higher electrical conductivity and mechanical strength in comparison to its amorphous counterpart. Hence, crystalline Ta_2O_5 is preferred over amorphous Ta_2O_5 for field emitter application.

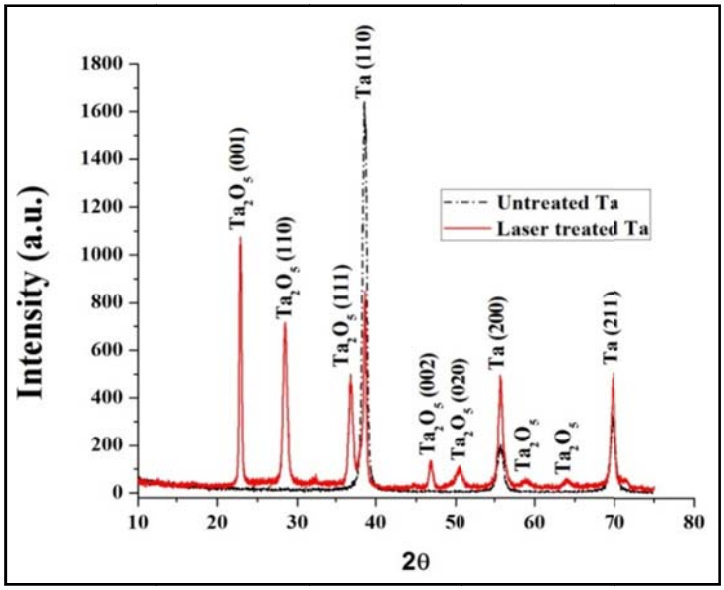

Figure 4.18 GI-XRD patterns of the untreated and laser treated Ta surfaces (Laser fluence for treatment was 0.55 J/cm^2) [126].

4.4.2.3 XPS characterization results

XPS analysis results of the fs laser treated Ta surface are shown in Figs. 4.19 (a-e). Fig. 4.19 (a) shows XPS survey spectrum of the Ta surface modified employing laser fluence of 0.55 J/cm^2. It is observed from the spectrum that only three peaks at binding energy (B.E.) 25.3 eV, 284.5 eV and 531.5eV are present which correspond to Ta (4f 5/2), C (1S) and O (1S), respectively [129].

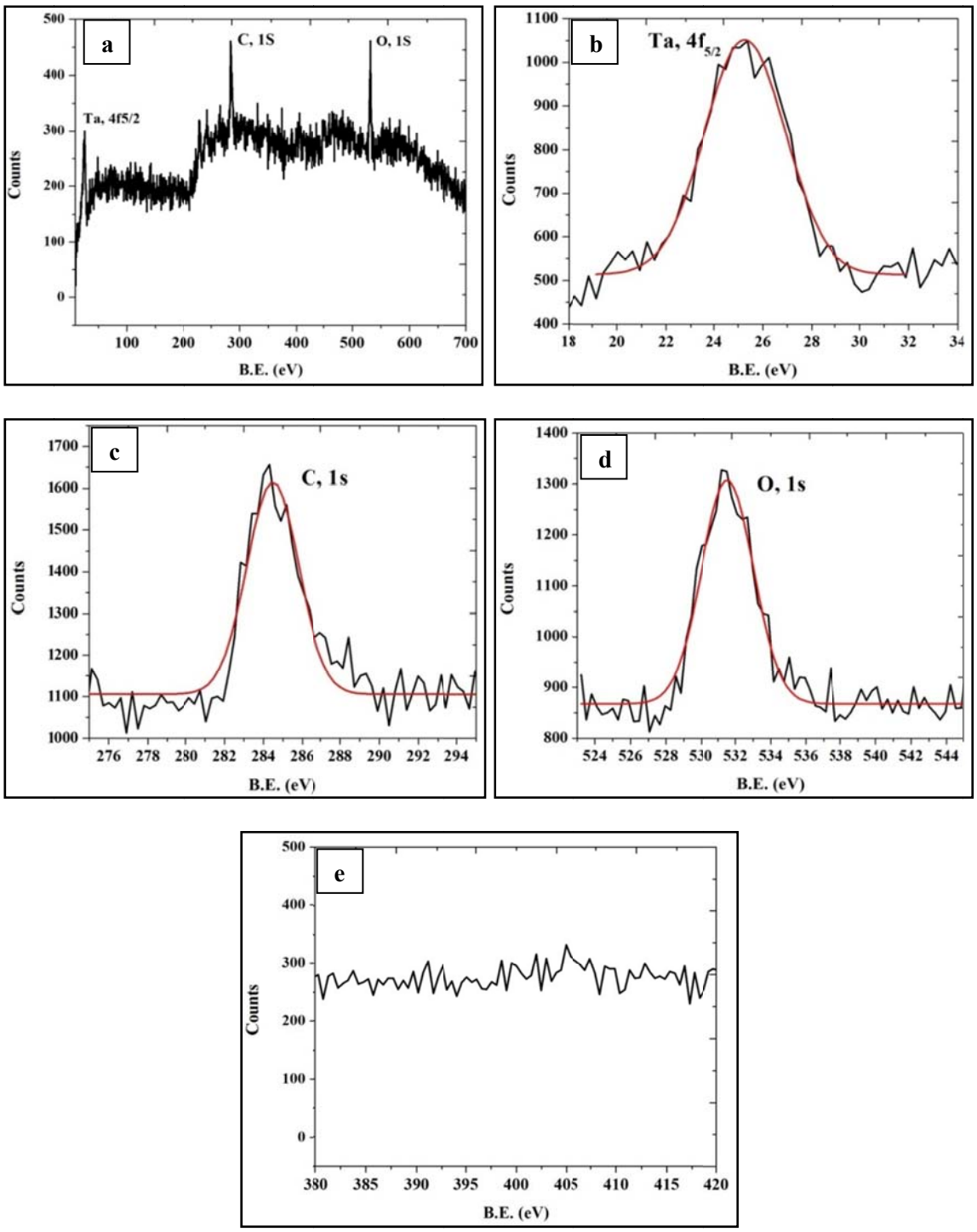

Figure 4.19 XPS analysis results of the Ta surface treated with 0.55 J/cm^2 (a) survey spectrum and expanded view of the peaks corresponding to (b) Ta, 4f$_{5/2}$ (c) C, 1S (d) O, 1S (e) region near to expected peak of N, 1S [126].

Figs. 4.19 (b−d) show expanded view of the peaks corresponding to Ta, C and O while Fig. 4.19 (e) shows expanded view of the spectrum where N (1S) is expected (~395 eV). XPS analysis has also confirmed absence of nitrogen on the surface supporting conclusion drawn by GI-XRD analysis that tantalum nitride is not formed on the laser treated surface. The observed XPS peak corresponding to C (1S) could be due to adsorption of organic compounds from the atmosphere as no peak corresponding to TaC is observed in GI-XRD pattern.

4.4.2.4 Field emission characterization results

Field emission characterizations of each of the samples treated with laser fluence of 0.35 J/cm^2 and 0.45 J/cm^2 were repeated twice while the specimen treated with 0.55 J/cm^2 was characterized thrice under same experimental conditions. Fig. 4.20 shows typical J_m vs E_m characteristics of the Ta samples treated with laser fluence of 0.35 J/cm^2 (Sample 1), 0.45 J/cm^2 (Sample 2) and 0.55 J/cm^2 (Sample 3) corresponding to one of the set of FE characterization. Here, also macroscopic field emission current density (J_m) and macroscopic applied field (E_m) have been defined same as they have been defined previously in the thesis. Turn on fields (E_{on}) of the Ta samples treated with laser fluence of 0.35 J/cm^2, 0.45 J/cm^2 and 0.55 J/cm^{2}were found to be 18.4 ± 0.3, 12.8 ± 0.8 and 4.0 ± 0.6 V/μm, respectively. FE characterization revealed that E_{on} corresponding to Ta surface micro-structured with laser fluence of 0.55 J/cm^2 is much lower than its value for samples treated with laser fluence of 0.35 J/cm^2 and 0.45 J/cm^2. The observed lower value of E_{on} corresponding to sample 3 in comparison to E_{on} values for sample 1 and sample 2could be due to larger size and lower number density of the generated micro-protrusions in sample 3 in comparison to sample 1 and sample 2. Larger size of the generated micro-protrusions leads to higher local field enhancement and lower number density leads to reduced effect of field

screening hence resulting in enhanced field emission. FN plots of the J_m vs E_m characterization data and their linear fits are shown in Fig. 4.21.

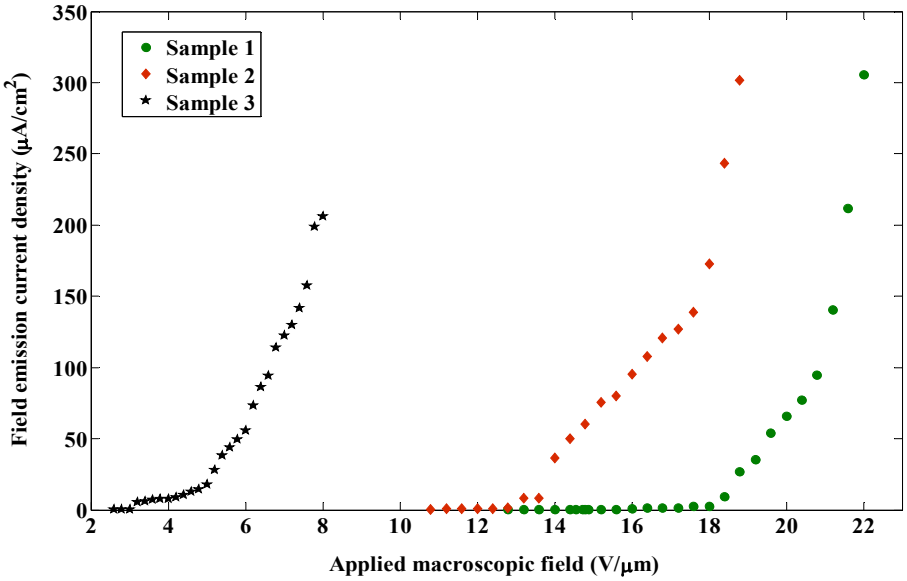

Figure 4.20 J_m vs E_m characteristics of the laser micro-structured Ta samples treated with laser fluence of 0.35 J/cm^2 (Sample #1), 0.45 J/cm^2 (Sample # 2) and 0.55 J/cm^2 (Sample # 3) [126].

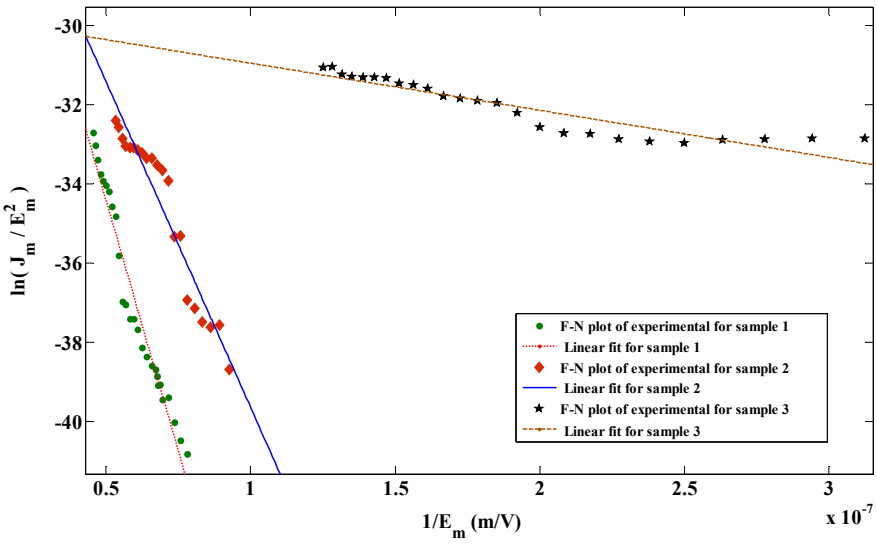

Figure 4.21 FN plots of the experimental data and their linear fit for laser micro-structured samples 1, 2 and 3 [126].

Parameters which characterize laser micro-structured surfaces as large area field emitter have been estimated using same approach which has been adopted for the case of SS 304 samples. Since our GI-XRD and XPS analysis confirmed formation of mainly Ta_2O_5 on the laser treated surfaces work function of Ta_2O_5 (φ=4.45 eV) [130] has been used instead of work function of Ta (φ = 4.1−4.3eV) [131, 132] to estimate large area field emitter parameters. Estimated field emitter parameters corresponding to experimental data shown in Fig. 4.20 have been summarized in Table 4.3. Field enhancement factors for Ta specimens surface modified with laser fluence levels of 0.35 J/cm^2, 0.45 J/cm^2 and 0.55 J/cm^2 were found to be 270 ± 30, 400 ± 80 and 4500 ± 500. Here, first number written in each case is the mean value of field enhancement factor and number written after ± sign is variation in the field enhancement factor value for different set of experiments. It is also observed from Table 4.3 that value of β_m increased and λ_m decreased on the sample as the incident laser fluence increased from 0.35 J/cm^2 to 0.55 J/cm^2 indicating that as field enhancement factor increases formal area efficiency of emission decreases. Reported data on field emission from different morphologies of Ta_2O_5 is presented in Table 4.4.

Table 4.3 Estimated field emitter parameters for fs laser micro-structured Ta (obtained from FE characterization data presented in Fig. 4.20).

Sr. No.	Field emitter characterizing parameter	Sample # 1	Sample # 2	Sample # 3
1.	Turn on field (E_{on}) [V/μm]	18.5	13.7	4.4
2.	Threshold field (E_{th}) [V/μm]	20.9	16.2	6.7
3.	Generalized slope correction factor (χ_m)	0.94	0.93	0.73
4.	Macroscopic field enhancement factor (β_m)	238	364	3947
5.	Macroscopic pre-exponential factor (λ_m)	2.6×10^{-10}	4.0×10^{-11}	6.4×10^{-16}

Table 4.4 Literature reported values of turn on field for different type of Tantalum oxide micro-structures.

Sr. No.	Surface morphology	Sample preparation method	E_{on} (V/μm)	β_m	Ref.
1.	Ta_2O_5 coated single wall carbon nano-tubes (SWCNTs) on Si substrate	HF-CVD and	12	-	[133]
2.	Ta_2O_5 aligned nanorods	Thermal deposition	8.5	764	[134]
3.	Nano-structures	He plasma treatment	9-10	300-1455	[135]
4.	Hierarchical Micro-protrusions	Fs pulsed laser irradiation	4.4-18.5	238-3947	Present study

Fig. 4.22 (a-c) show stability of the emission currents from Ta surface micro-structured with laser fluence of 0.35 J/cm^2, 0.45 J/cm^2 and 0.55 J/cm^2. It is observed from these figures that emission currents corresponding to surfaces treated with 0.35 J/cm^2 and 0.45 J/cm^2 have shown good stability. However, Ta sample micro-structured with 0.55 J/cm^2 has shown sudden drop in emission current by ~60 % after 40 minutes of continuous operation and became stable thereafter. This might be due to damage of sites/protrusions which were predominantly contributing towards field emission. Post field emission current stability test of the sample treated with 0.55 J/cm^2 this sample was again investigated for J_m vs E_m characteristics. Obtained J_m–E_m characteristics for this sample is shown in Fig. 4.23 which shows that emission current densities were significantly lower in comparison to the emission current densities in previous test i.e. prior to the field emission current stability run.

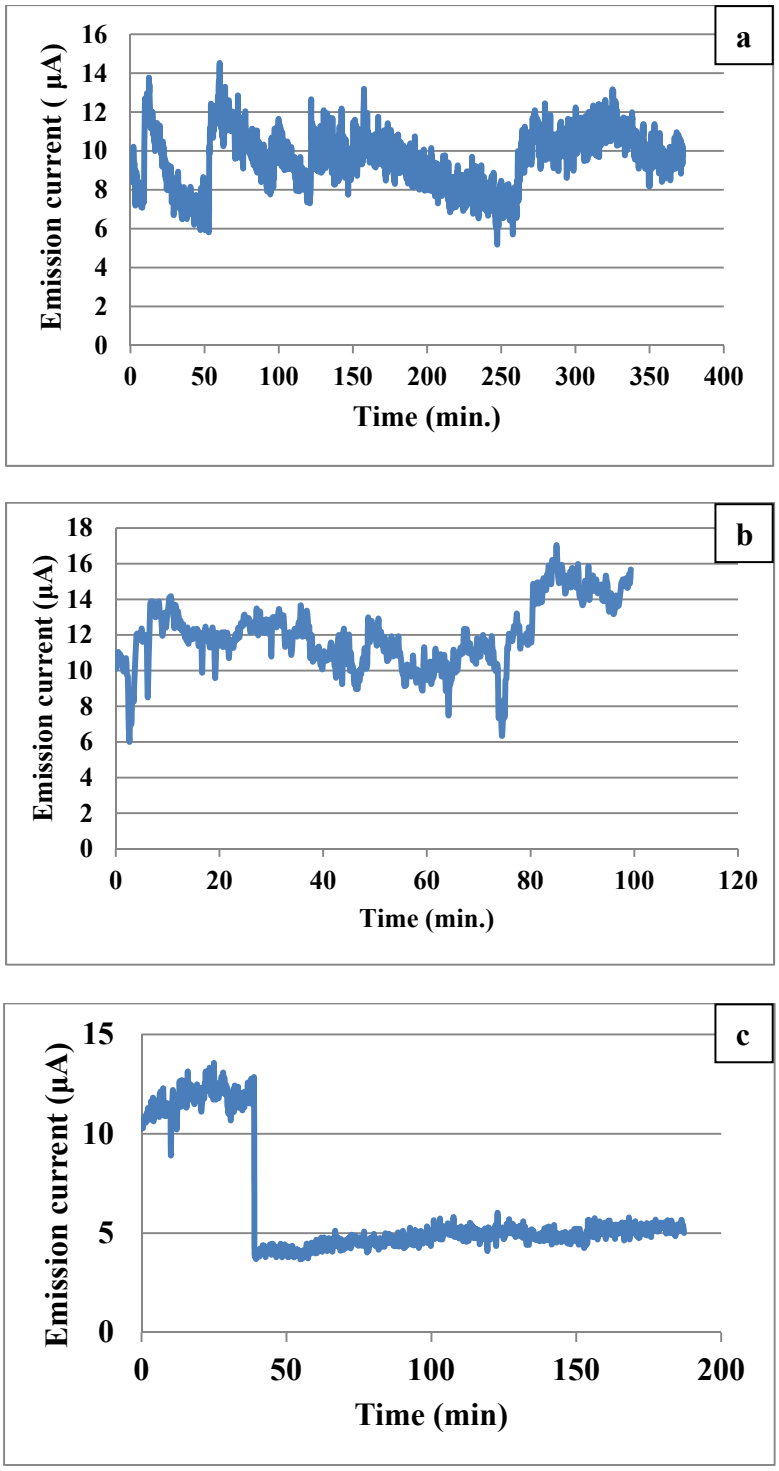

Figure 4.22 Variation of field emission current with time for Ta samples laser treated with laser fluence of (a) 0.35 J/cm^2 (b) 0.45 J/cm^2 (c) 0.55 J/cm^2 [126].

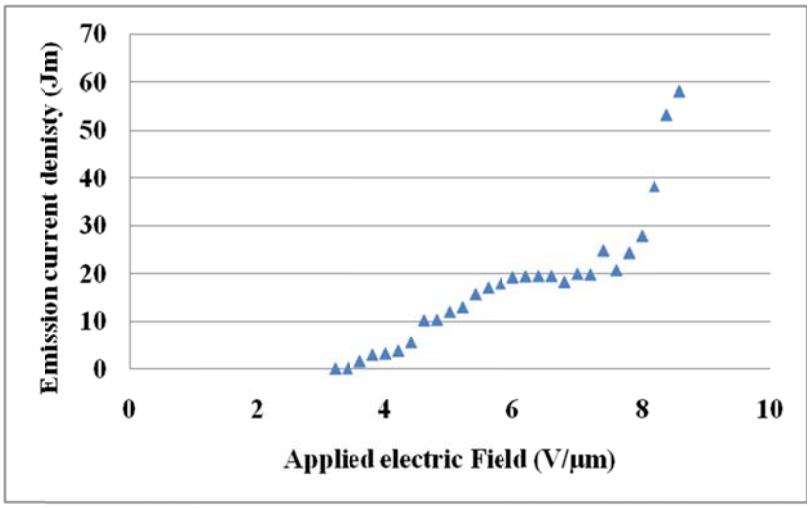

Figure 4.23 J_m—E_m characteristics of the Ta sample treated with laser fluence of 0.55 J/cm^2 (after field emission current stability test) [126].

4.5 Conclusion:

Irradiation of SS 304 and Ta targets with femtosecond pulsed laser has resulted in formation of self-assembled dense micro-protrusions on their surfaces. Generated micro-protrusions on both the surface are covered with sub-micron size features. Number density and height of the generated micro-protrusions were found to depend on laser fluence and target scan speed.

On SS 304 surface, number density of the generated micro-protrusions could be varied in the range 5.6 x10^5 − 1.8 x 10^6 μ-protrusions/cm^2 by varying laser fluence and target scanning speed. Fs laser treated SS surface was found to mainly consist of Fe_2O_3 and Fe_3C. SS surface having μ-protrusions of number density ~5.6 x 10^5 μ-protrusions/cm^2 has shown significantly higher field emission in comparison to SS sample with μ-protrusions number density of 1.5 x 10^6 μ-protrusions/cm^2. In best case fs laser treated SS 304 sample has shown low turn on field (~4.1V/μm), high macroscopic field enhancement factor (~1830) and stable field emission current.

Ta samples treated with fs laser at fluence levels 0.35 J/cm^2, 0.45 J/cm^2 and 0.55 J/cm^2 have shown generation of μ-protrusions with number densities equal to ~8.8x10^5 μ-protrusions/cm^2, ~7.5 x 10^5 μ-protrusions/cm^2 and ~3.5 x 10^5 μ-protrusions/cm^2, respectively. Fs laser modified Ta surface was found to predominantly consist of Ta_2O_5. Laser modified Ta samples have shown improvement in field emission behavior. Ta sample treated with laser fluence of 0.55 J/cm^2 has shown lowest turn on field (4.0 ± 0.6 V/μm) and highest macroscopic field enhancement factor (4400 ± 500) among all the fs laser treated Ta samples.

Chapter 5

Theoretical Simulation of Period of the Generated Micro-protrusions on SS 304 Surface upon Femtosecond Laser Irradiation

5.1 Introduction

Femtosecond (fs) laser generated self–assembled micro–protrusions on metal surfaces has shown improved performance in a variety of applications (summarized in Section 1.3 of Chapter 1). Reports indicate that number density of the generated micro-protrusions varies with incident laser fluence and target scanning speed. In our investigation too it was observed that number density/period of the grown micro-protrusions varied with incident laser fluence. Number density and height of the grown surface micro–protrusions play significant roles in field emission behavior of the laser micro-structured samples was also observed by us.

In addition to our experimental investigation theoretical model based simulation was undertaken to determine dependence of period/areal number density generated surface micro-protrusions as a function of incident laser fluence. This theoretical simulation is expected to help us in appropriately choosing the laser parameters to carry out surface micro-structuring of cathodes for field emission enhancement.

In this chapter our results on theoretical simulation to predict areal number density/period of the generated micro-protrusions on SS 304 and titanium (Ti) surfaces upon irradiation with fs laser are being presented. In this work we have theoretically simulated period of the generated surface micro-protrusions on Ti surface as a function of laser fluence and compared simulated period with the reported experimental data on micro-protrusions period [80] on Ti to validate the

theoretical model. Validated model has been then used to simulate period / number density of the surface micro-protrusions on stainless steel 304 surface.

In order to simulate period of the generated surface micro-protrusions first of all melting of the targets (Ti and SS 304) corresponding to irradiation with a single fs laser pulse has been simulated using a two temperature model (TTM) [136]. Simulated maximum melt depth (h_{max}) of the target, surface temperature and temperature gradient at surface corresponding to occurrence of maximum melt depth have been used to estimate expected number density/period of the generated surface micro-protrusions using a linear Hydrodynamic Kuramoto Sivashinsky Model (HDKS Model) [97]. A decrease in the simulated number density (increase in period) of micro-protrusions with increasing incident laser fluence was observed which is in agreement with both, reported [80] and our own experimental [Section 4.3 of Chapter 4] observations.

5.2 Theoretical model (Formulation of the problem)

Physical model used to predict the number density/period of the generated micro-protrusions for fs pulsed laser irradiation is summarized as below.

i. Generation of surface micro-protrusions on fs laser irradiated surface has been explained on the basis of hydrodynamic instability of the surface of the melt layer [97]. When a laser pulse is incident on the target surface a fraction of energy is reflected from the surface (R) and remaining energy is absorbed inside the target material. This absorbed energy causes heating of the target leading to melting and vaporization of the target material upto certain depth depending upon the incident laser fluence. If strong temperature gradient is present in the molten pool this can lead to instability of the melt layer surface. Temperature gradient induced instability leads to undulations in melt surface starting from plane surface. If re-solidification of the undulated surface occurs before it reaches an equilibrium state these

generated surface undulations on the molten layer surface results in generating an initial roughness of the surface. The created rough surface on the target causes non-uniform deposition of energy for next incident laser pulses, in the valley region energy deposited being more in comparison to inclined surface or hill region of the rough surface. Non-uniformly deposited energy density leads to a spatial temperature distribution and hence spatial variation of the surface tension. Also, due to absorption of laser beam there is attenuation of deposited energy along the depth of the target leading to a strong temperature gradient along depth direction too. Existing surface tension gradient in the melt pool causes liquid flow from low surface tension region towards high tension region. If temperature coefficient of surface tension is negative liquid flows from valley towards hills for each laser pulse incident on the target and surface undulation grows [136].

ii. To simulate period of surface micro-protrusions the linear Hydrodynamic Kuramoto–Sivashinsky (HDKS) model has been employed. According to this model hydrodynamic instability of the surface leads to formation of surface undulations of different periodicity each having different growth rate provided melt duration (t_m) is less the than time period of capillary oscillations (t_{cap}) i.e. [97] –

$$t_m < t_{cap} = \frac{2\pi}{\left(8\pi^3\gamma_s \tanh\left(\frac{2\pi h_m}{\Lambda_m}\right)/\rho\Lambda_m\right)^{1/2}} \quad \ldots\ldots\ldots (5.1)$$

Here, γ_s, ρ, h_m and Λ_m are surface tension of the melt pool at surface, density, melt depth and period of undulation, respectively. After irradiation with sufficiently large number of laser pulses surface micro-protrusions with spatial period corresponding to maximum growth rate

are formed. According to the HDKS model, period of the surface micro-protrusions (Λ_m) on the surface corresponding to maximum growth rate is given by [97] –

$$\Lambda_m = \frac{4\pi}{3} h_m \left[\frac{\gamma_s}{|\gamma_T||\partial T/\partial z|_{z=0} h_m}\right]^{1/2} \quad \ldots\ldots\ldots\ldots (5.2)$$

Here,$|\gamma_T|$ and $|\partial T/\partial z|_{z=0}$ are absolute value of temperature coefficient of surface tension and temperature gradient along depth direction at molten layer surface, respectively. In the present study z = 0 is surface of the target and z increases along depth direction in the target.

iii. Theoretical simulation has been carried out to estimated required parameters in equation (5.2) to estimate period of the generated surface micro-protrusions on target surface. When target is irradiated by a femtosecond laser pulse energy coupled to the target is first absorbed instantaneously (time scale ~ 10^{-15} s) by free electrons present in the target. The electrons which absorb energy go to excited state and again come to thermal equilibrium with other electrons via electron-electron scattering process within time scale of few tens of femtosecond. Energy from the electronic subsystem to lattice subsystem is transferred via electron–phonon scattering process. Thermalization between electronic and lattice subsystems occur at a time scale of the order of ~ ps. Hence, electronic and lattice subsystems remain at two different temperatures before the thermalization between these two subsystems occur. Therefore, simulation of the femtosecond laser pulse induced heating and melting of the target has been carried out using a two temperature model (TTM) upto the time of thermalization of electron and lattice subsystems. According to TTM heating of electrons and lattice subsystems can be written as [136] –

$$C_e(T_e)\frac{\partial T_e(z,t)}{\partial t} = \frac{\partial}{\partial z}\left[k_e(T_e, T_l)\frac{\partial T_e(z,t)}{\partial z}\right] - G(T_e)[T_e(z,t) - T_l(z,t)] + S(z,t) \quad \ldots\ldots\ldots (5.3)$$

$$C_l(T_l)\frac{\partial T_l(z,t)}{\partial t} = \frac{\partial}{\partial z}\left[k_l(T_e, T_l)\frac{\partial T_l(z,t)}{\partial z}\right] + C_l(T_l)v_a\frac{\partial T_l}{\partial z} + G(T_e)[T_e(z,t) - T_l(z,t)] \ldots\ldots (5.4)$$

Here, T_e (z, t) and T_l (z, t) are the temperatures of electrons and lattice subsystems at depth z from the surface at time equal to t, respectively. C_e and k_e are volumetric heat capacity and thermal conductivity of the electronic subsystem, respectively. C_l and k_l are volumetric heat capacity and thermal conductivity of the lattice subsystem, respectively. G is electron-lattice coupling constant, v_a is recession velocity of the surface due to ablation and S (z, t) is laser source term at depth z from the target at time t. Thermal conductivities of electrons and lattice subsystems in metals have been considered to vary as following relations [137] ─

$$k_e = k_{eq}(T_e/T_l) \quad \ldots\ldots\ldots\ldots (5.5)$$

$$k_l = 0.01k_{eq} \quad \ldots\ldots\ldots\ldots (5.6)$$

Here, k_{eq} is thermal conductivity of the target material when electron and lattice subsystems are in thermal equilibrium. Equation (5.5) is valid only for T_l, $T_e << T_c$ (thermodynamic critical temperature). Thermodynamic critical temperature (T_c) for titanium is ~1x 10^4 K [138] and T_c for main constituents of SS 304 (Fe, Cr, Ni) is also ~1x 10^4 [139]. However, due to lack of functional relation for k_e variation in Ti at T_e and T_l values in the range near to T_c and beyond we have assumed in the present case that variation of k_e follows equation (5.5) for all the values of T_e and T_l. In the case of metals contribution of lattice in thermal conductivity is normally assumed to be ~1% of the total thermal conductivity and remaining is due to free electrons present in the metal. Therefore, variation of k_l has been considered as equation (5.6) in the entire temperature range in simulation. Laser source term [S (z, t)] as a function of position and time is given by the following equation [136] ─

$$S(z,t) = \frac{F}{\sqrt{\frac{\pi}{4\ln(2)}}}\frac{1}{\tau_p}(1-R)\alpha \exp\left(-\alpha z - (4\ln(2)\left(\frac{t-\tau_p}{\tau_p}\right)^2\right) \quad \ldots\ldots\ldots (5.7)$$

Where, F, R, τ_p and α, are incident average laser fluence, surface reflectivity of the target, laser pulse duration (FWHM) and absorption coefficient of the target, respectively.

For time beyond occurrence of thermalization between electronic and lattice subsystems a single temperature (T) of the target has been defined. Evolution of target temperature (T) as function of time (t) and position (along depth direction from target surface) after reaching thermal equilibrium between electrons and lattice has been estimated using the following equation–

$$C_p \frac{\partial T(z,t)}{\partial t} = \frac{\partial}{\partial z}\left[k(z,t)\frac{\partial T}{\partial z}\right] + C_p v_a \frac{\partial T}{\partial z} \quad \ldots\ldots\ldots\ldots (5.8)$$

Here, T (z, t) and k (z, t) are temperature and thermal conductivity of the target at depth z from the surface at time equal to t, respectively. C_p is volumetric heat capacity of the target and v_a is recession velocity of the ablation front. v_a is given by the following equation–

$$v_a = 0.82\left(\frac{m}{2\pi k_b T_s}\right)^{\frac{1}{2}}\frac{P_s}{\rho} \quad \ldots\ldots\ldots\ldots (5.9)$$

Here, m is atomic mass of the target, k_b is Boltzmann constant, ρ is density of the target and P_s is saturated vapor pressure corresponding to surface temperature T_s. P_s has been calculated using the Clausius–Clapeyron equation as below–

$$P_s = P_0 \exp\left(\frac{m\Delta H_v}{k_b}\left(\frac{1}{T_b} - \frac{1}{T_s}\right)\right) \quad \ldots\ldots\ldots\ldots (5.10)$$

Where, P_0 is ambient pressure (in the present study $P_0 = 1.013 \times 10^5$ Pa). ΔH_v is latent heat of vaporization and T_b is boiling point of the target.

iv. Maximum melt depth, surface temperature and temperature gradient at the melt layer surface corresponding to maximum melt depth were estimated by solving equations (5.3), (5.4) and (5.8) for a given laser fluence level. Using surface temperature (T_s) value surface tension of the liquid at surface layer was estimated. These theoretically simulated parameters were used in equation (5.2) to estimate period of the generated surface micro-protrusions.

5.3 Numerical solution

All the heat equations have been solved using explicit finite difference method. Equations (5.3) and (5.4) have been solved for a time duration of ~3 ps (time scale of the order of electron-lattice thermalization in chosen materials) by taking into account time step (Δt) of 0.1 fs and grid size along depth direction (Δz) equal to 1 nm. Thereafter, equation (5.8) has been solved using time step (Δt) of 0.1 ps and grid size along depth (Δz) = 2 nm upto 7 ns. Time step (Δt) and grid size (Δz) have been chosen to satisfy following stability criteria−

$$r_e = \frac{k_e}{C_e}\frac{\Delta t}{\Delta z^2} < 0.5 \qquad \text{……. (5.11)}$$

$$r_l = \frac{k_l}{C_l}\frac{\Delta t}{\Delta z^2} < 0.5 \qquad \text{…… (5.12)}$$

Where, r_e and r_l are constants. In addition to satisfying the stability criteria, smaller values of Δt and Δz results in better accuracy of the numerical solution but increases demands on number of calculations. Hence, Δt and Δz are chosen judiciously get reasonable accuracy and number of calculations.

5.3.1 Solving heat equations before thermalization of electron and lattice

Evolution of T_e and T_l with time and depth from the target surface have been determined by solving equations (5.3) and (5.4). These equations have been solved together using following initial and boundary conditions –

Initial condition:

At t = 0: $T_l(z, t) = T_e(z, t) = 300$ K (Room temperature) ……. (5.13)

Boundary conditions:

At front surface (z = 0) —

$$-k_e \frac{\partial T}{\partial z} = 0 \quad \text{..…….. (5.14)}$$

$$-k_l \frac{\partial T}{\partial z} = -J_v - J_c - J_r \quad \text{…… (5.15)}$$

Where J_v, J_c and J_r are heat flux going out of target surface due to vaporization, surface conductance and radiation loss mechanisms, respectively. J_v, J_c and J_r are given by following equations–

$$J_v = \rho v_a(\Delta H_v + \Delta H_m) \quad \text{……. (5.16)}$$

$$J_c = h_t(T_s - T_{amb}) \quad \text{....……. (5.17)}$$

$$J_r = \sigma\varepsilon(T_s^4 - T_{amb}^4) \quad \text{……. (5.18)}$$

Where, ΔH_m, h_t, T_{amb}, σ and ε are latent heat of fusion, heat transfer coefficient of surface in air, ambient temperature, Stephan-Boltzman constant, total emissivity of the target, respectively.

At lower boundary (z = 200 nm) —

$T_l(z, t) = T_e(z, t) = 300$ K $= T_{amb}$…….. (5.19)

To solve equations (5.3) and (5.4) lower boundary of the problem was chosen at ~200 nm because of the fact that skin depth (depth in the target by which laser intensity reduces to 1/e times its value on the target surface) for Titanium and SS 304 are 15.9 nm and 14.2 nm, respectively. Therefore, at the depth of 200 nm laser beam intensity will reduce by ~$(1/e)^{13}$ times its value at surface i.e. laser source term at 200 nm will be negligibly small. Also, since these equations have been solved over a time scale of ~3 ps thermal heat diffusion length within this time duration will be negligible (Estimated thermal diffusion length in Ti and SS 304 within 3 ps time duration is ~0.5 nm).

Phase change of the material during heating and cooling cycles is modeled by apparent heat capacity method. In this method it is assumed that phase change of the material takes place over certain temperature range (ΔT) instead of a single temperature. Effect of latent heat during of phase change (melting and vaporization) is incorporated by increasing heat capacity of the material over range in which phase change takes place. Model used for heat capacity at the time of melting is given as below [136]-

$$C_p = \begin{cases} C_s < (T_m - \Delta T) \\ \frac{C_s + C_L}{2} + \frac{\Delta H_m \rho}{2\Delta T}(T_m - \Delta T) \le T \le (T_m + \Delta T) \\ C_L > (T_m + \Delta T) \end{cases} \quad \text{..... (5.20)}$$

Here, C_s and C_L are heat capacities of solid and liquid phase of the target and T_m is melting point of the target. In the present case we have chosen ΔT equal to 25 K for SS 304 sample because for SS 304 melting occurs in temperature range of ~50 K instead of single point. While in the case of Ti, ΔT has been chosen equal to 10 K. As $\Delta T$is reduced simulation results move towards accurate value. However, if rate of increase in temperature is high there is a chance to skip the phase transition phenomenon in the simulation. Therefore, ΔT is chosen in such a way that phase

change phenomenon is captured during the temporal evolution in simulation. Similarly, at time of liquid to vapor phase change heat capacity has been modeled as−

$$C_p = \begin{cases} C_L < (T_b - \Delta T_1) \\ C_L + \frac{\Delta H_v \rho}{2\Delta T}(T_b - \Delta T_1) \leq T \leq (T_b + \Delta T_1) \\ C_L > (T_b + \Delta T_1) \end{cases} \quad \ldots\ldots\ldots\ldots (5.21)$$

Here, ΔT_l has been chosen to be equal to 10 K for SS 304 and Ti both the samples.

5.2.2.2 Evolution of target temperature after electron lattice thermalization

In the present study thermalization temperature for Ti and SS 304 were found to be less than 3 ps hence to evolution of temperature inside target after 3 ps has been simulated by solving equation (5.8). Following initial and boundary conditions have been used to solve equation (5.8)−

Initial condition-

Initial time for solving equation (5.8) is chosen as t = 3ps and lattice temperature profile in the target obtained from solving equations (5.3) and (5.4) is used as initial temperature distribution i.e.

$T(z, t = 3\ ps) = T_l(z, t = 3\ ps)$ ……. (5.22)

Boundary conditions for solving equation (5.8):

At z = 0 (front boundary)-

$$-k\frac{\partial T}{\partial z} = -J_v - J_c - J_r \ldots\ldots\ldots\ldots (5.23)$$

Here, J_v, J_c and J_r are same as defined in equations (5.16) ─ (5.18).

At z = 900 nm (back boundary)

T = 300 K …….. (5.24)

5.4 Thermo-physical properties of the materials (Ti & SS 304) used for theoretical simulation

Thermo-physical and optical properties of titanium and stainless steel 304 which have been used for theoretical simulation study are provided in Table 5.1 and Table 5.2, respectively. Some of the properties provided in Tables 5.1 and 5.2 have been directly taken from the reported values while some of them have been derived from the reported values. For example, surface reflectivity and absorption coefficient for SS 304 and Ti has been estimated from the reported values of the real and imaginary parts of the refractive index. Surface reflectivity (R) and absorption coefficient (α) were calculated using following equations −

$$R = \frac{(n-1)^2-\kappa^2}{(n+1)^2+\kappa^2} \qquad \ldots\ldots\ldots\ldots\ldots (5.25)$$

$$\alpha = \frac{4\pi\kappa^2}{\lambda} \qquad \ldots\ldots\ldots\ldots\ldots (5.26)$$

Where, n and κ are real and imaginary parts of refractive index. λ is wavelength of the laser light. Similarly, values of electron specific heat (C_e) and electron phonon coupling factor (G) as a function of electron temperature (T_e) provided in Table 5.1 and Table 5.2 have been estimated by fitting the reported data taken from literature.

Table 5.1 Thermo-physical and optical properties of Titanium used in theoretical simulation.

Sr. No.	Property	Value	Ref.
1.	Refractive index	Real part (n) = 3.14 Imaginary part (κ) = 4.01	[140]
2.	Surface reflectivity (R)	0.62 (Estimated from n and κ values)	
3.	Absorption coefficient (α)	6.3 x 10^7 m^{-1}(Estimated from κ value)	
4.	Density (ρ)	(i) 4.5x10^3 kg m^{-3} (at 300K) & (ii) ~ 3.5x10^3 kg m^{-3} (at 3500K) Mean value: ~ 4.0x10^3 kg m^{-3}	[141] [142]
5.	Melting point (T_m)	1941 K	[143]
6.	Boiling point (T_b)	3560 K	[144]
7.	Val. Heat capacity of (C_p)	(i) C_s = ρ x (626 J kg^{-1} K^{-1}) (mean value of solid phase) (ii) C_l = ρ x (980 J kg^{-1} K^{-1}) (mean value of liquid phase)	[144]
8.	Vol. heat capacity of electrons (C_e)	$\begin{cases} 9.3196 \times 10^4 + (266.21 T_e) & Te < 0.85 \times 10^4 K \\ 2.07 \times 10^4 + (0.3578\ T_e) & \text{if } 0.85 \times 10^4 \le T_e \le 3.5 \times 10^4 K \\ -95806 + 61.25\ T_e & \text{if } T_e > 3.5\ x\ 10^4 K \end{cases}$ ($Jm^{-3}K^{-1}$)	[145]
9.	Thermal conductivity at thermal equilibrium (k_{eq})	17 W m^{-1} K^{-1} (mean value in solid phase) 28 W m^{-1} K^{-1} (mean value in liquid phase)	[143]
10.	Electron-phonon coupling factor (G)	$\begin{cases} 1.042E18 + 1.111E15\ T_e - 1.0213E11\ T_e T_e & \le 5.6E3\ K \\ 4.701E18 - 1.206E14\ T_e + 1.192E9\ T_e - 2085.76\ T_e & 5.6E3 < T_e \le 5E4\ K \\ 13.98E17 & T_e > 5E4\ K \end{cases}$ ($Wm^{-3}K^{-1}$)	[145]
11.	Latent heat of fusion (ΔH_m)	295 kJ/kg	[146]
12.	Latent heat of vaporization (ΔH_v)	8.88 x10^3 kJ/kg	[146]
13.	Surface tension (γ)	1.64 Nm^{-1}	[142]
14.	Temperature coefficient of surface tension ($\partial\gamma/\partial T$)	-2.38 x 10^{-4} $Nm^{-1}K^{-1}$	[142]
15.	Heat transfer coeff. (h_t)	5 W/m^2/K	[147]
16.	Emissivity (ε)	0.34@ temperature in the range 1640 K to 2000 K	[148]

Table 5.2 Thermo-physical and optical properties of SS 304 used in theoretical simulation.

Sr. No.	Property	Value	Ref.
1.	Refractive index	Real part of refractive index (n) = 3.5 Imaginary part of refractive index (κ) = 4.8	[149]
2.	Surface reflectivity (R)	0.67 (Estimated from n and κ values)	
3.	Absorption coefficient (α)	7.59×10^7 m^{-1} (Estimated from κ value)	
4.	Density (ρ)	7.1×10^3 $kg.m^{-3}$[Mean value of the solid and liquid phase densities]	[150]
5.	Melting point (T_m)	1723 K (Solidus temperature: 1698 K & Liquidus temperature: 1748K)	[151]
6.	Boiling point (T_b)	2910 K	[151]
7.	Vol. heat capacity of lattice (C_p)	(i) $C_s = \rho \times (600\ J\ kg^{-1}\ K^{-1})$ [Mean of solid phase] (ii) $C_L = \rho \times (800\ J\ kg^{-1}\ K^{-1})$ [Mean of liquid phase]	[150]
8.	Vol. heat capacity of electrons (C_e)	$\begin{cases} 680 \times T_e & \text{if } Te < 2.5 \times 10^3 K \\ (680 \times 2.5 \times 10^3) + 173(T_e - 2.5 \times 10^3) & \text{if } 2.5 \times 10^3 \le T_e \le 10^4 K \\ (680 \times 2.5 \times 10^3) + 173(10^4 - 2.5 \times 10^3) + 23.33(T_e - 10^4) & \text{if } T_e > 10^4 K \end{cases}$ $(Jm^{-3}K^{-1})$	[149]
9.	Thermal conductivity in equilibrium (k_{eq})	$k_{eq} = \begin{cases} 24\ W\ m^{-1}K^{-1} & \text{if } T < T_m \text{ (Mean value of solid phase)} \\ 29\ W\ m^{-1}K^{-1} & \text{if } T > T_m \text{ (Mean value of solid phase)} \end{cases}$	[152]
10.	Latent heat of fusion (ΔH_m)	300 kJ/kg	[153]
11.	Latent heat of vaporization (ΔH_v)	6.5×10^3 kJ/kg	[153]
12.	Electron-phonon coupling factor (G)	$\begin{cases} 53 \times 10^{17} & \text{if } T_e \le 7 \times 10^3 K \\ (53 \times 10^{17}) - 16.67 \times 10^{13}(T_e - 7 \times 10^3) & \text{if } 7 \times 10^3 < T_e \le 2.3 \times 10^4 K \\ 28 \times 10^{17} & \text{if } T_e > 2.3 \times 10^4 K \end{cases}$ $(Wm^{-3}K^{-1})$	[149]
13.	Surface tension (γ)	1.84 Nm^{-1} @1823K	[150]
14.	Temp. coeff. of surface tension ($\partial\gamma/\partial T$)	-0.4×10^{-3} $Nm^{-1}K^{-1}$	[150]
15.	Heat transfer coeff. (h_t)	5 $W/m^2/K$	[147]
16.	Emissivity (ε)	0.22 @ temperature of 1000 K	[154]

5.5. Simulation results on Titanium

Femtosecond (fs) laser induced melting, ablation depth, period of the generated micro-protrusions and number density of the generated surface micro-protrusions on Ti sample have been theoretically simulated for single incident laser pulse with varying laser fluence in the range 0.5 J/cm^2 to 1.1 J/cm^2.

Fig. 5.1 shows a theoretically simulated temporal evolution of temperatures of electron and lattice subsystems at titanium sample surface corresponding to irradiation with a single fs laser pulse with laser fluence of 0.7 J/cm^2. Fig. 5.1 reveals that electron temperature increases at much higher rate in comparison to the lattice temperature. The observed faster temperature change for electrons in comparison to lattice subsystem is due to lower heat capacity of electrons in comparison to the lattice. This figure also indicates that electron and lattice subsystems reach in thermal equilibrium within 3 ps and lattice temperature reaches up to ~ 1.0 x 10^4 K in 3 ps after irradiation with a fs laser pulse.

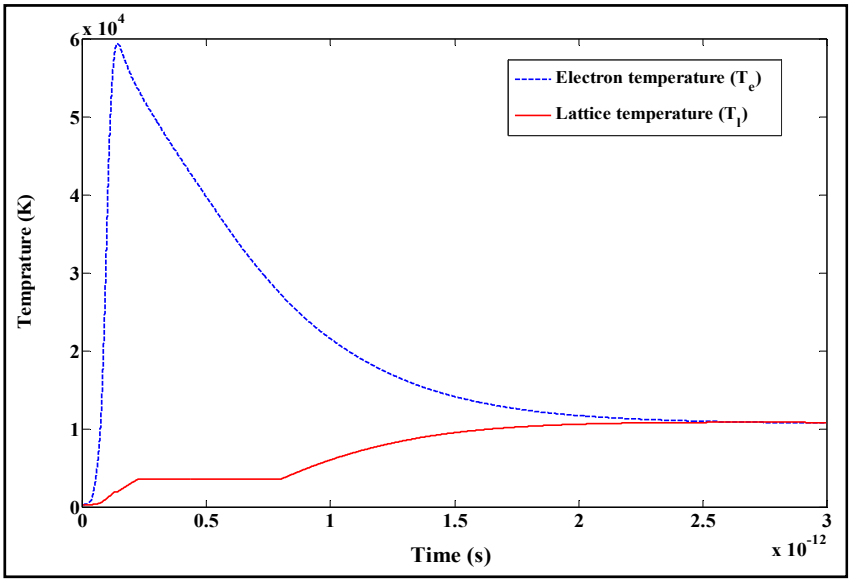

Figure 5.1 Temporal evolutions of temperatures of electron and lattice subsystems at Ti target surface corresponding to a laser fluence of 0.7 J/cm^2.

Fig. 5.2 shows a typical temporal evolution of melt depth in the Ti target corresponding to irradiation with single fs laser pulse with laser fluence of 0.7 J/cm^2. This figure clearly shows that melt depth in the target first increases up to a certain maximum value (h_m=160nm)at a particular time then after decreases.

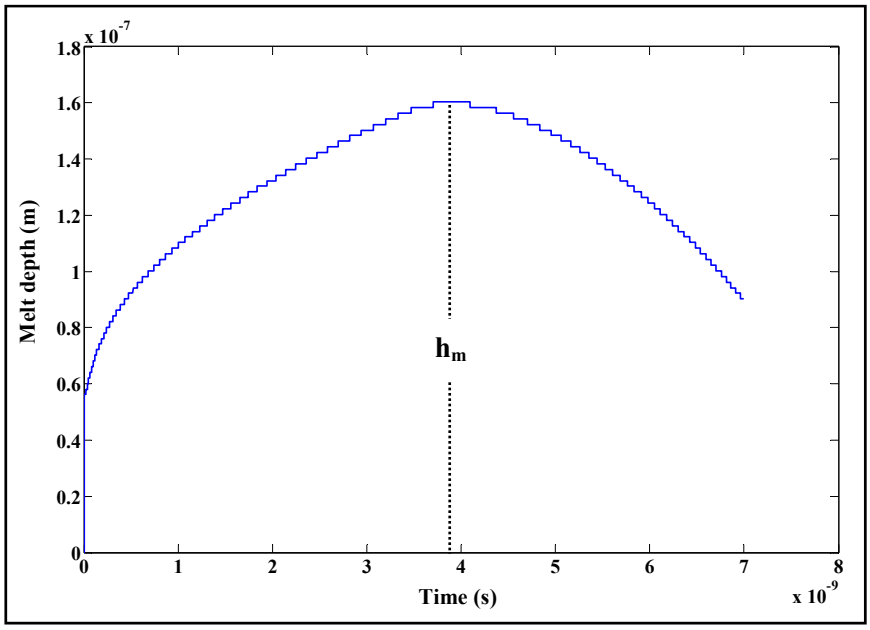

Figure 5.2 Temporal evolution of the melt depth in Ti target corresponding to irradiation with laser fluence of 0.7 J/cm^2.

Fig. 5.3 shows a typical simulated temperature distributions along depth direction in Ti sample at time t equal to 3 ps and at a time when maximum melt depth occurs in the target (t equal to ~ 4 ns) corresponding to irradiation with laser fluence of 0.7 J/cm^2. This figure clearly shows that at the time of maximum melt depth temperature distribution has become smoother in comparison to the temperature distribution at t equal to 3 ps. This would have happened due to heat diffusion process in the target because of strong temperature gradient along the depth direction.

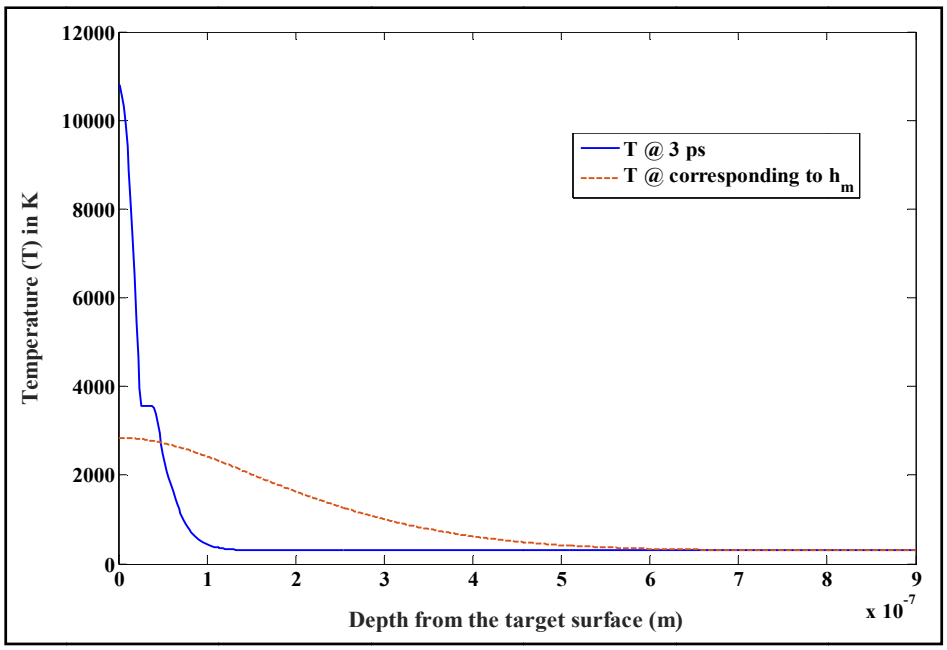

Figure 5.3 Temperature variation along depth direction in the Ti target at two different times (a) 3 ps (b) at the time of maximum melt depth (~ 4 ns) corresponding to laser fluence of 0.7 J/cm^2.

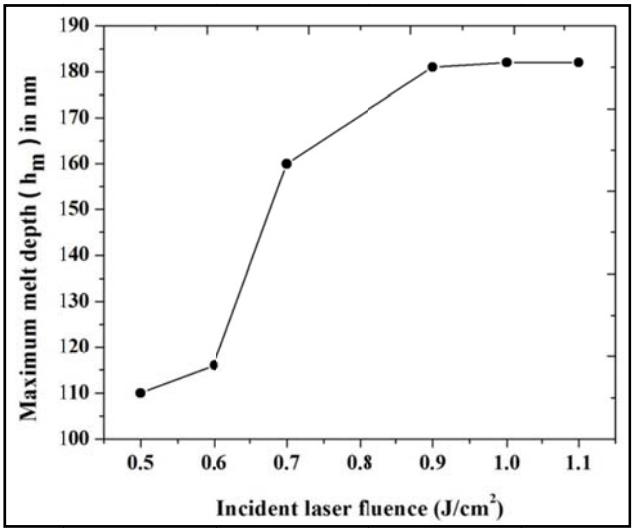

Figure 5.4 Variation of melt depth in Ti target as a function of incident laser fluence.

Fig. 5.4 shows variation of the maximum melt depth (h_m) in the Ti target as a function of incident laser fluence. It is observed from this figure that as laser fluence increased from 0.5 J/cm^2 to 0.7 J/cm^2, melt depth increased from 110 nm to 160 nm. However, rate of increase of

melt depth slows down for increase of laser fluence beyond 0.7 J/cm^2. The observed slowdown of the rate of increase of maximum melt depth as fluence beyond 0.7 J/cm^2 could be due to increase in ablation rate from the target surface.

Fig. 5.5 shows ablation depth per pulse as a function of incident laser fluence. This figure clearly shows a sharp increase in ablation depth per pulse for laser fluence >0.7 J/cm^2. This observed increase in ablation rate could be possible reason for slowdown of rate of increase in h_m with incident laser fluence beyond 0.7 J/cm^2.

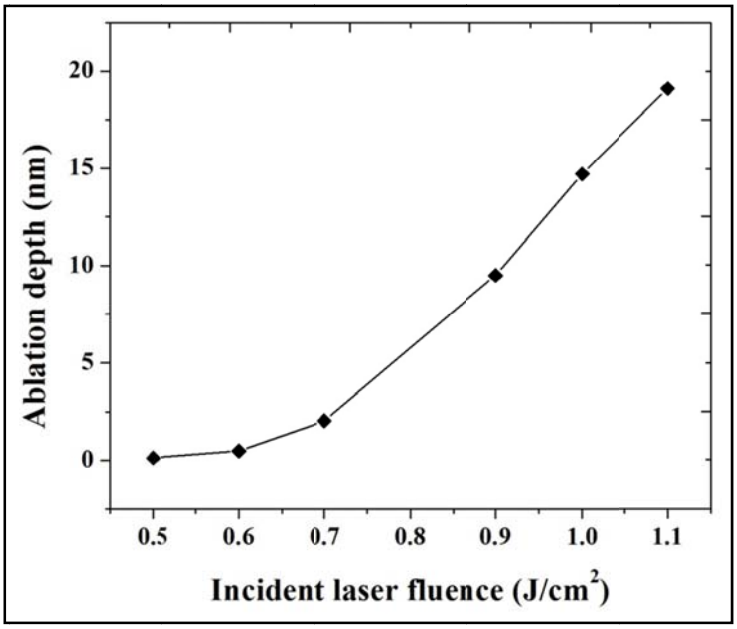

Figure 5.5 Variation of ablation depth per pulse for Ti target as a function of laser fluence.

Fig. 5.6(a) shows variation of the simulated period of the generated surface micro-protrusions as a function of incident laser fluence. Reported variation of the period of generated micro-protrusions on Ti surface corresponding to irradiation with 450 laser pulses [1] is shown in Fig. 5.6 (b). Comparison of the Figs. 5.6 (a) and 5.6 (b) revealed that the theoretically simulated trend and experimentally obtained trend by fs laser irradiation [1] on variation of the period of surface micro-protrusions are in good agreement. In addition, magnitudes of the period of these micro-

structures are also of the same order. Therefore, this theoretical model was used to predict micro-protrusions period and number density of the generated surface micro-protrusion.

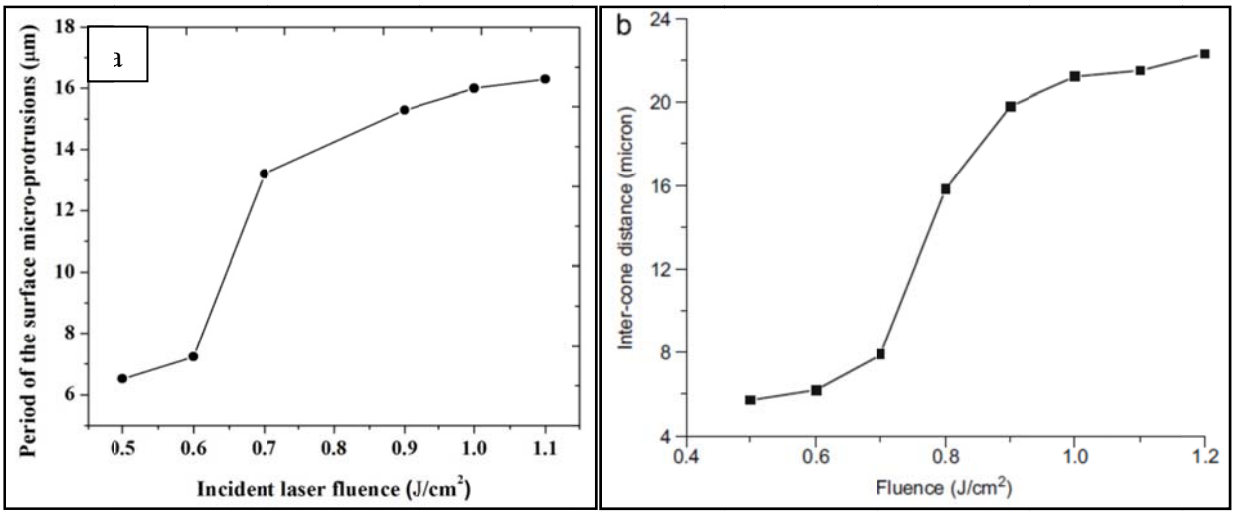

Figure 5.6 Variation of period of surface micro-protrusions as a function of incident laser fluence (a) Simulated (b) reported [1].

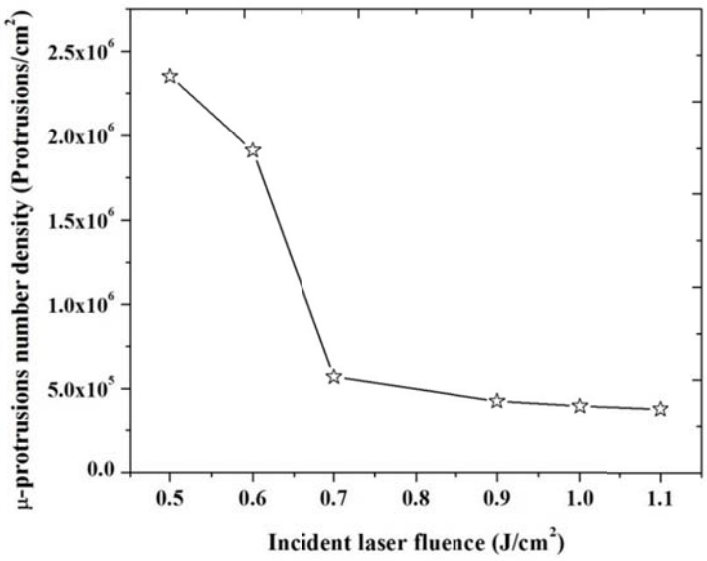

Figure 5.7 Variation of number density of the generated surface micro-protrusions as a function of incident laser fluence.

Number density of the generated micro-protrusions on Ti sample surface has been estimated from the simulated period of the surface micro-protrusions. Variation of the estimated number density of the micro-protrusions as a function of laser fluence is shown in Fig. 5.7.

Having broadly validated our simulation model against experimental observations reported for titanium we next used this model to predict period and number density of the surface micro-protrusions on stainless steel 304 by fs laser irradiation.

5.6 Simulation results on SS 304

Figure 5.8 shows theoretically estimated temporal evolution of temperature of electron and lattice subsystems at surface of the SS target corresponding to a typical laser fluence of 0.7 J/cm^2. Fig. 5.8 shows that electrons and lattice reaches a thermal equilibrium within ~3 ps of irradiation with an fs laser pulse. Also, lattice temperature reaches a temperature of ~7500 K (much beyond the boiling point of the SS 304) at ~3 ps.

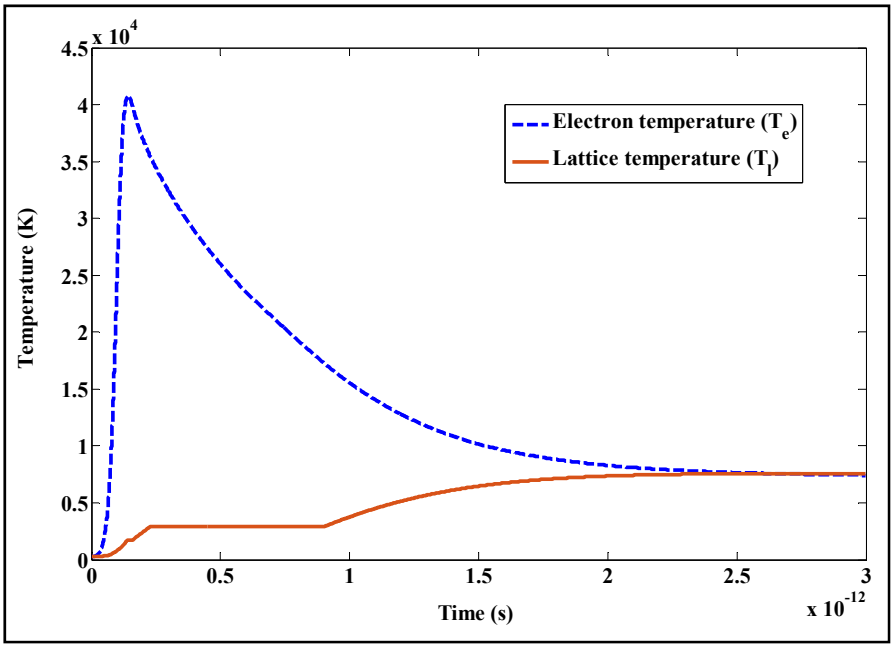

Figure 5.8 Temporal evolution of T_e and T_l at SS 304 surface corresponding to laser fluence of 0.7 J/cm^2.

Fig. 5.9 shows the theoretically estimated variation of the maximum melt depth (h_m) of SS sample as a function of incident laser fluence. This figure clearly shows that h_m in the target initially increases rapidly with increasing incident laser fluence and then slows down. Slowing down of the rate of increase in the maximum melt depth is most likely due to an increase in ablation rate of the target at higher laser fluence. Variation of the ablation depth per pulse as a function of the incident laser fluence is shown in Fig. 5.10. This figure reveals that ablation depth increases sharply when laser fluence is increased beyond 0.8 J/cm^2.

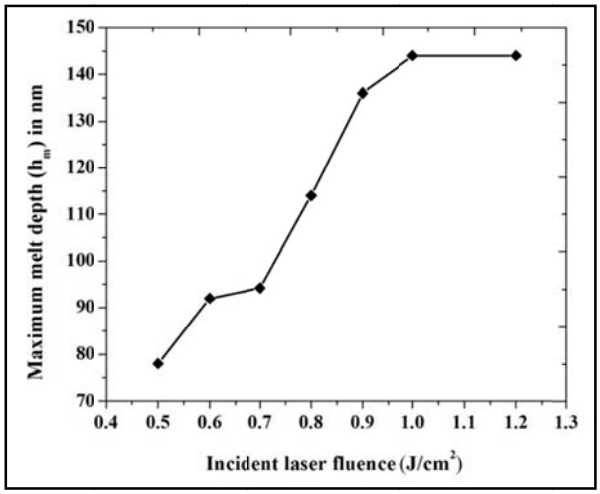

Figure 5.9 Variation of maximum melt depth (h_m) in SS 304 as a function of incident laser fluence.

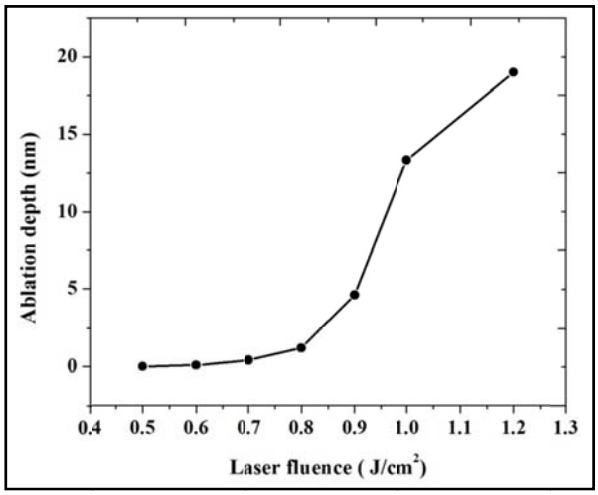

Figure 5.10 Variation of ablation depth in SS 304 sample with laser fluence.

Fig. 5.11 shows variations in the period of the laser generated surface micro-protrusions on the SS target surface. At high laser fluence (≥ 0.9J/cm^2) slower increase in the simulated period of the micro-protrusions could be due to saturation of the laser induced maximum melt depth at higher laser fluence and decrease in temperature gradient in the melt pool with increasing laser fluence. Corresponding variation of number density of the generated surface micro-protrusions as a function of incident laser fluence is shown in Fig. 5.12. Theoretically simulated number density corresponding to laser fluence of 0.9 J/cm^2 was compared with experimentally observed number density of the surface micro-protrusions on SS 304 observed by us corresponding to a laser fluence of 0.9 J/cm^2 (Reported in Section 4.3.2). Theoretically simulated number density of the generated surface micro-protrusions was ~1 x 10^6 protrusions/ cm^2 while experimentally observed number density of micro-protrusions varies in the range 1.1x 10^6 to 1.8 x 10^6 protrusions/cm^2 depending upon the target scan speed.

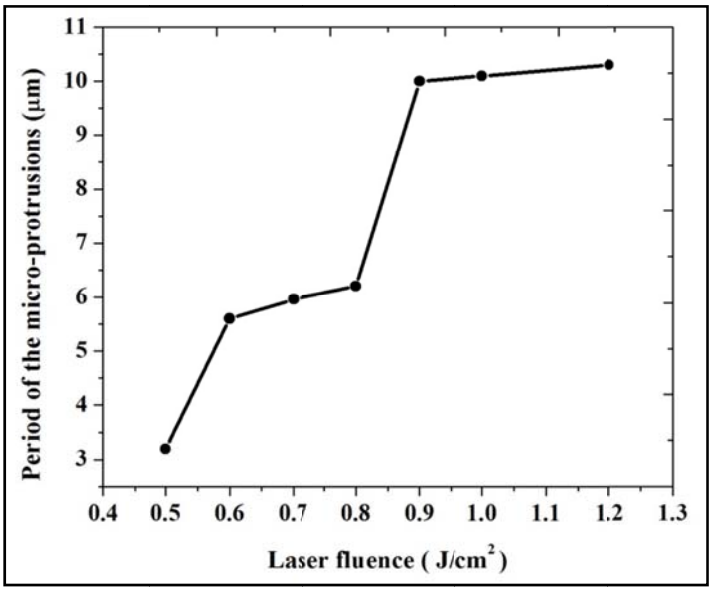

Figure 5.11 Variation of the period of surface micro-protrusions on SS sample as a function of laser fluence.

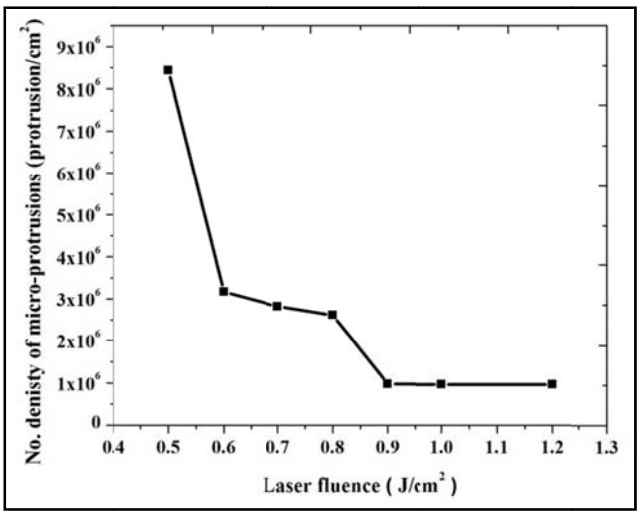

Figure 5.12 Variation of number density of micro-protrusions on SS surface as function of laser fluence.

5.7 Conclusion

Areal number density and period of the generated surface micro-protrusions on Ti and SS 304 targets have been theoretically simulated based on a single femtosecond laser pulse irradiation. Variation of the simulated period of the surface micro-protrusions with incident laser fluence corresponding to Ti surface was found to follow a similar trend as reported in literature corresponding to ~450 laser pulses. However, simulated period of the micro-protrusions at lower laser fluecne level (< 0.6 J/cm^2) were slightly higher (~20%) than the reported period and at higher laser fluence levels (in the range 0.9 to 1.1 J/cm^2) simulated period of micro-protrusions were lower (~25 %) than the reported values. This observation could be due to difference between considered material properties for simulation and actual variations in material properties as a function of temperature. Having broadly validated our theoretical model against experimental data reported for Ti period and number density of the generated micro-protrusions on SS 304 surface as a function of the incident laser fluence was also theoretically predicted. Theoretically simulated number density corresponding to laser fluence of 0.9 J/cm^2 was

compared with experimental number density of the surface micro-protrusions on SS 304 observed by us corresponding to a laser fluence of 0.9 J/cm^2 (Reported in Section 4.3.2). Theoretically simulated number density of the generated surface micro-protrusions was ~1 x 10^6 protrusions/cm^2 while experimentally observed number density of micro-protrusions varies in the range 1.1 x 10^6 to 1.8 x 10^6 protrusions/cm^2 depending upon the target scan speed.

Chapter 6

Conclusion & Future perspective

6.1 Conclusion

In the present study, we carried out surface micro-structuring of stainless steel 304 (SS 304) and tantalum (Ta) samples via irradiation with a focused beam of nanosecond (ns) or femtosecond (fs) lasers. Surface micro-structuring of sample surfaces was carried out by varying laser fluence and number of laser pulses irradiating the target at a specific location. Surface micro-structured samples were characterized in terms of surface morphology, roughness, chemical phase, crystallographic phase and field emission behavior. Irradiation of targets with optimized laser fluence and number of laser pulses resulted in generation of self-assembled micro-protrusions on the surfaces. These micro-structured surfaces have shown improved field emission behavior in comparison to the pristine samples. In addition to the experimental work theoretical simulation was carried out to predict period of the generated micro-protrusions on SS 304 surface corresponding to irradiation with fs laser pulse.

Surface micro-structuring experiments on SS 304 targets using nanosecond laser revealed that targets irradiated with laser fluence $\geq$ 4 J/cm^2 and 3000 pulses resulted in deep crater formation in the target. Self-assembled micro-protrusions were formed in the laser irradiated surface when incident laser fluence was $\leq$ 2 J/cm^2. Average height of the generated micro-protrusions on SS surface corresponding to 2 J/cm^2 increased from 17 μm to 30 μm when number of incident laser pulses increased from 3000 to 9000. While initial growth of height of surface protrusions with incident number of pulses was rapid it slowed after certain number of laser pulses. When SS sample was irradiated with 0.7 J/cm^2 and 6000 laser pulses surface micro-

protrusions were formed over the entire laser irradiated spot. SS 304 sample treated with laser fluence of 0.7 J/cm^2 was characterized for chemical phase. This sample showed that laser treated surface consists of iron oxides and iron nitrides. SS 304 sample surface micro-structured with laser fluence of 0.7 J/cm^2 demonstrated low turn on field (~7.5 V/μm), high macroscopic field enhancement factor (~585) and delivered emission current density up to 340 μA/cm^2. Formal area efficiency of emission for this specimen was estimated to be ~2.7×10^{-10} which implies that a very small fraction of the actual specimen was actually contributing towards emission of electrons. Field emission current from the laser micro-structured specimen was fairly stable over the test period.

Similarly, surface micro-protrusions were generated on Ta targets via nanosecond laser irradiation with laser fluence of 0.9 J/cm^2 and varying number of laser pulses in the range 3000 to 9000. In the case of Ta too, height of the generated surface micro-protrusions and mean roughness of the laser treated surface increased with increasing number of irradiating pulses. Raman spectroscopy results revealed that chemical phase of the laser treated region varied with position within the laser irradiated region. Central region of the laser irradiated spots where incident local laser fuence was higher remained in metallic phase while periphery of the irradiated spot consists of Ta_2O_5. Laser treated Ta samples showed enhanced field emission. Ta sample treated with 9000 laser pulses demonstrated lowest E_{on} (~3.7 V/μm) and delivered maximum emission current density (~386 μA/cm^2) among all the laser treated Ta samples. However, field emission current stability of this sample was poor in comparison to the other laser treated Ta samples.

Dense array of self-assembled micro-protrusions were generated on SS sample surfaces using optimized fs laser fluence and number of incident pulses per location. SS sample showed

generation of surface micro-protrusions with number density ~5.6 x 10^5 micro-protrusions/cm^2corresponding to irradiation with laser fluence of 0.5 J/cm^2 and number of laser pulses per location equal to ~3.1 x 10^4. When SS sample was irradiated with laser fluence of 0.9 J/cm^2 and number of laser pulses equal to ~2250 (corresponding to target scan speed of 400 μm/s) surface micro-protrusions were generated with number density ~1.5 x 10^6 micro-protrusions/cm^2. SS sample micro-structured with ~3.1 x 10^4 laser pulses per location at laser fluence of 0.5 J/cm^2 showed superior field emission behavior in comparison to SS sample surface modified with 2250 laser pulses per location at laser fluence of 0.9 J/cm^2. Measured turn on field and estimated macroscopic field enhancement factor corresponding to SS specimen treated with laser fluence of 0.5 J/cm^2 were ~4.1 V/μm and ~1830, respectively. The observed poor field emission behavior of the SS sample treated with 0.9 J/cm^2 was explained on the basis of field screening effect.

Similarly, dense array of self-assembled micro-protrusions were generated on Ta surfaces via irradiation with fs laser pulses with optimized laser fluence levels for achieving enhanced field emission. Number densities of the generated surface micro-protrusions on Ta samples treated with laser fluence levels of 0.35 J/cm^2, 0.45 J/cm^2 and 0.55 J/cm^2 were ~8.8 x 10^5, ~7.5 x 10^5 and ~3.5 x 10^5 μ-protrusions/cm^2, respectively. Fs laser modified Ta surfaces were found to predominantly consist of Ta_2O_5. The fs laser modified Ta samples demonstrated improvement in field emission behavior. Ta sample treated with laser fluence of 0.55 J/cm^2 has shown lowest turn on field (4.0 ± 0.6 V/μm) and highest macroscopic field enhancement factor (4400 ± 500) among all the fs laser treated Ta samples. However, its field emission current stability was poorer than other laser modified samples.

In addition to experimental investigations on ns and fs laser induced surface modification and their characterization we carried out a theoretical simulation study to predict period of the generated surface micro-protrusions on SS 304 and titanium surfaces by fs laser. Simulated period of the generated surface micro-protrusions on Ti surface as a function of laser fluence was compared with reported experimental data on Ti to validate our theoretical model. Simulated trend of the variation of micro-protrusions period with laser fluence broadly matched with the reported data confirming validity of the model. Thereafter, this model was used to simulate period of the generated micro-protrusions on SS 304 sample corresponding to fs laser irradiation.

6.2 Future perspective of the work

Future scope of the work described in this thesis includes both experimental and theoretical investigations. In future, other materials such as Tungsten (W), Molybdenum (Mo) and Niobium (Nb) could be surface micro-structured using both fs, as well as, ns lasers. In order to achieve high field emission current density at low applied field along with stable emission current, laser parameters would have to be optimized. Also materials having low work function, high thermal and electrical conductivity, low vapor pressure, high melting point and high hardness could be deposited on surface micro-structured surfaces to achieve enhanced field emission current density, stable emission current and long cathode life time. In future, simulation would be further improved by incorporating change in material properties as a function of temperature to predict number density and height of the cones and range of fluence over which cones are formed. Simulation would also be extended to account for multiple laser pulses instead of single pulse condition.

Details of the Ph. D. candidate

Name in English: Anil Kumar Singh

हिंदी में नाम: अनिल कुमार सिंह

Enrolment No.: PHYS01201304014

Title of the Thesis: Pulsed Laser Surface Treatment of Metals for Enhanced Field Emission Studies

CI name: Bhabha Atomic Research Centre, Mumbai

Thesis Highlight

Name of the Student: Anil Kumar Singh
Name of the CI/OCC: BARC, Mumbai **Enrolment No.:** PHYS01201304014
Thesis Title: Pulsed Laser Surface Treatment of Metals for Enhanced Field Emission Studies
Discipline: Physical Sciences **Sub-Area of Discipline:** Physics
Date of viva voce: 24/08/2020

During the last two decades pulsed laser based surface processing has emerged as technique of potential importance for a variety of applications due its offered advantages over conventional surface processing techniques. One such application is pulsed laser based surface micro-structuring/texturing of the targets for improving performances of bio-implants, solar cells, large area field emission cathodes (LAFEC) etc.

In this thesis, surface micro (μ)-structuring of metallic targets such as Stainless Steel 304 (SS 304) and Tantalum (Ta) have been carried out via direct irradiation with nanosecond (ns) and femtosecond (fs) laser pulses with the aim to generate μ-protrusions for achieving enhanced field emission effect. The surface μ-structured specimens have been investigated in terms of surface morphology, chemical phase and their field emission behavior. Target surfaces irradiated with optimum laser fluence and a number of laser pulses have shown generation of high density μ-protrusions on their surfaces resulting in enhanced field emission in comparison to the pristine surfaces. Theoretical simulation has been carried out to estimate expected areal number density/spatial period of the generated surface micro-protrusions corresponding to fs laser irradiation of SS 304. Our numerical model has been validated by comparing simulation and reported experimental results for Titanium.

Typical SEM images of the laser μ-structured SS 304 and Ta specimen are shown in Figs. 1 & 2, respectively. A typical variation of macroscopic field emission current density (J_m) versus applied macroscopic electric field (E_m) corresponding to a laser treated SS 304 specimen is shown in Fig. 3. Estimated macroscopic field enhancement factor for the laser μ-structured SS and Ta specimens was found to be in the range 585 to 1830 and 270 to 4500, respectively.

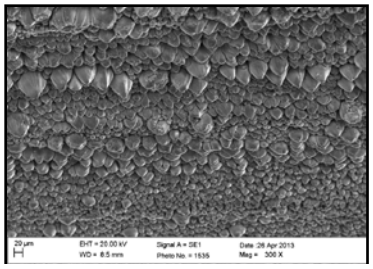

Figure 1: Typical SEM image of a SS 304 specimen μ-structured with fs laser irradiation.

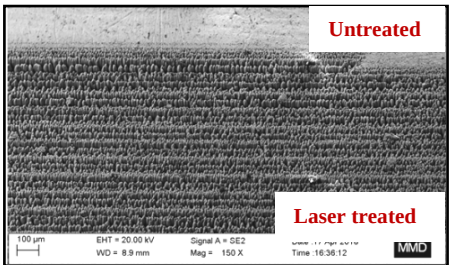

Figure 2: Typical SEM image of a Tantalum specimen showing surfaces of untreated and fs laser treated (@ laser fluence: 0.55 J/cm^2) regions.

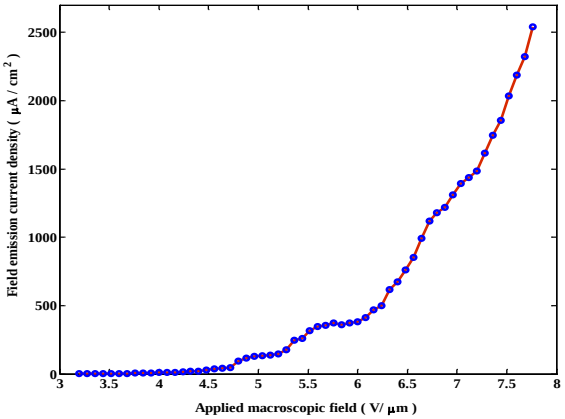

Figure 3: J_m-E_m characteristics of SS specimen micro-structured with laser fluence of 0.5 J/cm^2 and target scan speed of 200 μm/s.